



An Optical and Infrared Photometric Study of the Young Open Cluster IC 1805 in the Giant H II Region W4^{*†}

Hwankyung Sung^{1,2}, Michael S. Bessell³, Moo-Young Chun⁴, Jonghyuk Yi⁵, Y. Nazé⁶, Beomdu Lim⁴, R. Karimov⁷, G. Rauw⁶,
Byeong-Gon Park⁴, and Hyeonoh Hur⁸

¹ Department of Astronomy and Space Science, Sejong University, 209 Neungdong-ro, Kwangjin-gu, Seoul 05006, Korea; sungh@sejong.ac.kr

² Visiting Researcher, Korea Astronomy and Space Science Institute, Korea

³ Research School of Astronomy & Astrophysics, The Australian National University, Canberra, ACT 2611, Australia

⁴ Korea Astronomy and Space Science Institute, 776 Daedeokdae-ro, Yuseong-gu, Daejeon 34055, Korea

⁵ SELab, Inc., 8 Nonhyeon-ro 150-gil, Gangnam-gu, Seoul 06049, Korea

⁶ Groupe d'Astrophysique des Hautes Energies, Institut d'Astrophysique et de Géophysique, Université de Liège, Allée du 6 Août, 19c, Bât B5c, B-4000 Liège, Belgium

⁷ Ulugh Beg Astronomical Institute, Uzbek Academy of Sciences, 33 Astronomical Street, Tashkent 700052, Uzbekistan

⁸ Daegu National Science Museum, 20, Techno-daero-6-gil, Yuga-myeon, Dalseong-gun, Daegu 43023, Korea

Received 2016 October 12; revised 2017 April 11; accepted 2017 April 13; published 2017 May 9

Abstract

We present deep wide-field optical CCD photometry and mid-infrared *Spitzer*/IRAC and MIPS 24 μm data for about 100,000 stars in the young open cluster IC 1805. The members of IC 1805 were selected from their location in the various color–color and color–magnitude diagrams, and the presence of H α emission, mid-infrared excess emission, and X-ray emission. The reddening law toward IC 1805 is nearly normal ($R_V = 3.05 \pm 0.06$). However, the distance modulus of the cluster is estimated to be 11.9 ± 0.2 mag ($d = 2.4 \pm 0.2$ kpc) from the reddening-free color–magnitude diagrams, which is larger than the distance to the nearby massive star-forming region W3(OH) measured from the radio VLBA astrometry. We also determined the age of IC 1805 ($\tau_{\text{MSTO}} = 3.5$ Myr). In addition, we critically compared the age and mass scale from two pre-main-sequence evolution models. The initial mass function with a Salpeter-type slope of $\Gamma = -1.3 \pm 0.2$ was obtained and the total mass of IC 1805 was estimated to be about $2700 \pm 200 M_{\odot}$. Finally, we found our distance determination to be statistically consistent with the Tycho-*Gaia* Astrometric Solution Data Release 1, within the errors. The proper motion of the B-type stars shows an elongated distribution along the Galactic plane, which could be explained by some of the B-type stars being formed in small clouds dispersed by previous episodes of star formation or supernova explosions.

Key words: open clusters and associations: individual (IC 1805) – stars: formation – stars: pre-main sequence

Supporting material: machine-readable tables

1. Introduction

The young open cluster IC 1805 is one of the core clusters of the Cas OB6 association and is surrounded by the giant H II region W4, which is at the center of three massive H II regions W3/W4/W5 in the Perseus spiral arm of the Galaxy. The Perseus region is one of most active star-forming regions (SFRs) in the Galaxy. The physical properties of the giant H II region or the relation between W4 and the massive stars in IC 1805 are relatively well studied. The relatively small masses of the molecular clouds in the region together with the lower metallicity, higher gas temperature, and lower gas surface density are considered to be unfavorable conditions for star formation. Although there are eight known O-type stars in IC 1805, the largest number of O stars in the northern young open clusters, the stellar content, especially of low-mass stars, the

star-formation history, and the shape of the initial mass function of the whole area of IC 1805 are not well known, and therefore are all interesting issues to study.

The giant H II region W4 is also known as a Galactic chimney/superbubble first proposed and discovered from the high-resolution H I observations of the Perseus arm by Normandeau et al. (1996, 1997). The reality of a Galactic superbubble was confirmed by Dennison et al. (1997) from a wide-field H α image and analysis of the ionization balance. They also estimated the age of the superbubble to be between 6.4–9.6 Myr. Based on the estimated age of the superbubble, they argued that the massive wind and supernova explosions from an earlier generation of stars before the formation of IC 1805, was responsible for the formation of the 230 pc superbubble. Later, Reynolds et al. (2001) found a much larger H α loop extending about 1.3 kpc above the Galactic plane. They suggested that the formation of such a gigantic superbubble may take 10–20 Myr or more, which implies the existence of an even older generation of stars in the region. Guetter & Vrba (1989) also suggested the existence of such an old group of stars from the broadening of the MS band of early B-type stars. Carpenter et al. (2000) found that about 39% of the cluster population, identified in the K' images of 32 IRAS point sources distributed in the Cas OB6 association, is embedded in small clouds located as far as 100 pc from the W3/W4/W5 region, and speculated that these small clouds are

* The optical imaging data in this article were gathered with two facilities: the AZT-22 1.5 m telescope at Maidanak Astronomical Observatory in Uzbekistan and the Canada–France–Hawaii Telescope (CFHT), which is operated by the National Research Council of Canada, the Institut National des Sciences de l'Univers of the Centre National de la Recherche Scientifique of France, and the University of Hawaii.

† This work has made use of data from the European Space Agency mission *Gaia* (<http://www.cosmos.esa.int/gaia>), processed by the *Gaia* Data Processing and Analysis Consortium (DPAC, <http://www.cosmos.esa.int/web/gaia/dpac/consortium>). Funding for the DPAC has been provided by national institutions, in particular, the institutions participating in the *Gaia* Multilateral Agreement.

fragments of a cloud complex dispersed by previous episodes of massive star formation.

From the similarity in age between stars in IC 1795 and IC 1805, Oey et al. (2005) suggested that the formation of IC 1795, as well as IC 1805, was triggered by the massive stars of the earliest generation, and that IC 1805 may be located on the edge of the shell. There are eight (or nine depending on the spectral type of MWC 50 = VSA 113)⁹ known O stars in IC 1805, which are considered to be the triggering source of massive star formation in the high density layer of the eastern part of W3 (Carpenter et al. 2000; Fukuda et al. 2013). Besides the star formation of the whole W3/W4 regions, several small-scale star-formation events triggered by the hot massive stars in IC 1805 were also investigated for the bright rim clouds (BRCs) 5 and 7 (Ogura et al. 2002; Fukuda et al. 2013; Panwar et al. 2014).

The spatial distribution of the young stellar objects (YSOs) within an SFR, gives important information on the embedded physical processes that influence star formation in the region (Koenig et al. 2012). Although there are eight O-type stars in IC 1805, the surface density of stars in IC 1805 is very sparse, and therefore the region is called an aggregate (Guetter & Vrba 1989) or OB association (Oey et al. 2005), rather than an open cluster. The stellar IMF of IC 1805 is also another important issue given its many O-type stars, though situated at a large Galacto-centric distance with unfavorable conditions for star formation, such as lower surface density of molecular gas and relatively higher gas temperature due to lower metallicity. The IMF of IC 1805 was investigated by, Sung & Lee (1995), Massey et al. (1995), and Ninov et al. (1995). Sung & Lee (1995) derived a slightly shallow IMF ($\Gamma = -1.1 \pm 0.2$), while Massey et al. (1995) and Ninov et al. (1995) obtained nearly normal IMF slopes; however, their work was limited to massive stars. In addition, photometric studies with modern CCDs tend to be relatively shallow and limited to the central region only.

The multiplicity fraction of massive stars is another important research topic because the binarity or multiplicity of stars is a direct result of star-formation processes (Duchêne & Kraus 2013). The multiplicity fraction of O stars is being actively investigated by Rauw & De Becker (2004), De Becker et al. (2006), Hillwig et al. (2006), and Rauw & Nazé (2016). Currently, three O stars (HD 15558, BD+61 497, and BD+61 498) have been identified as double-lined spectroscopic binary (SB2) systems. De Becker et al. (2006) obtained a large mass ratio between the primary and the secondary of HD 15558, and suspect that HD 15558 is a massive triple system. However, the current value of the binary fraction of IC 1805 is lower than that of other young open clusters (Sana et al. 2012).

In this study, we provide deep wide-field optical CCD photometry of the young open cluster IC 1805. In addition, for a complete and homogeneous census of low-mass pre-main-sequence (PMS) stars with thick circumstellar disks, we obtained the mid-infrared (MIR) magnitudes of objects from the archival *Spitzer*/IRAC (Fazio et al. 2004) and MIPS (Rieke et al. 2004) 24 μm images. The published X-ray source lists were also used for the selection of cluster members. Based on the large volume of photometric data over the $41' \times 45'$ area of

IC 1805, we investigated the reddening law, the reddening, distance, age, and the IMF of IC 1805.

This paper is organized as follows. The optical photometry and photometry of *Spitzer*/IRAC and MIPS 24 μm images are described and compared in Section 2. Optical and MIR photometric data for about 100,000 stars are presented. The cross-match with X-ray emission objects from *Chandra* and *XMM-Newton* X-ray observations is also performed in the section. Some properties of X-ray emission objects were analyzed in the section. Membership selection is described in Section 3 including a detailed description of the selection of PMS stars with $H\alpha$ emission, the classification of YSOs in the MIR diagrams and selection of MIR excess emission stars, X-ray emission stars, and massive and intermediate-mass members. Fundamental parameters, such as reddening, the reddening law, distance, and radius of IC 1805 are obtained in Section 4. The Hertzsprung–Russell diagram (HRD) is constructed in Section 5. Also in Section 5, the IMF and age of IC 1805 are derived, the mass and age of PMS stars from two popular PMS evolution models are compared, and the total mass of IC 1805 is estimated. In Section 6, we present some discussion on the distance of the W3/W4 regions, the parallax and proper motion data from the *Gaia* astrometric mission are analyzed, and some discussion is made on the star-formation process of massive O- and B-type stars in IC 1805. The star-formation history of the IC 1805/Cas OB6 association and its relation with the high-mass X-ray binary LS I+61 303 is also discussed in the section. The summary and conclusions are given in Section 7.

2. Observations

2.1. Optical Photometry

For a study of the IMF and the star-formation history of the young open cluster IC 1805, we obtained deep wide-field *VRI* and $H\alpha$ images of IC 1805 using the CFH12K mosaic CCD camera of the CFHT on 2002 January 6 and 7. We also observed several regions in IC 1805, for a study of the reddening and massive star content, using the SITE 2000 \times 800 CCD (Maidanak 2k CCD) and standard *UBVRI* filters of the AZT-22 1.5 m telescope at the Maidanak Astronomical Observatory in Uzbekistan. Later, we obtained additional images of the central region of IC 1805 with the Fairchild 486 CCD (SNUCam - Lim et al. 2009; Im et al. 2010) and *UBVI* and $H\alpha$ filters of the AZT-22 telescope. The optical observations are summarized in Table 1.

2.1.1. CFH12K Observations

2.1.1.1. Observation and Standardization

Deep wide-field *VRI* and $H\alpha$ photometry was obtained for the young open cluster IC 1805 with the CFH12K, a 6×2 mosaic CCD camera of the 3.6 m CFHT. We obtained images of the central region (we refer to this region as “CFH12K-C”) on 2002 January 6, and observed the North (“CFH12K-N”) and South (“CFH12K-S”) regions on 2002 January 7. The observed three regions largely overlap each other and so the total surveyed area of IC 1805 is about $43' \times 45'$, as shown in Figure 1. To fill in the gaps between CCD chips, we used a three-point dithering pattern for a given pointing. The central wavelength of the $H\alpha$ filter is 6584 Å with a bandwidth of 76 Å. The *VRI* filters used at CFHT are Mould interference filters, which have a more rectangular responses than the

⁹ O9Ve by Ishida (1970), O9.5Ve by Shi & Hu (1999), Be by Massey et al. (1995), and B2 by Wolff et al. (2011).

Table 1
Observation Log

Telescope	Detector	Date of Obs.	Region	Exposure Time	Seeing ^a (")
CFHT	CFH12K	2002. 1. 6	Center	<i>I</i> : 75 s × 3, <i>R</i> : 150 s × 3, <i>V</i> : 150 s × 3, H α : 1875 s × 3	0.86 ± 0.06
		2002. 1. 7	North	<i>I</i> : 6 s, 75 s × 3, <i>R</i> : 10 s, 150 s × 3, <i>V</i> : 10 s, 150 s × 3, H α : 900 s	0.82 ± 0.07
		2002. 1. 7	South	<i>I</i> : 6 s, 75 s × 3, <i>R</i> : 10 s, 150 s × 3, <i>V</i> : 10 s, 150 s × 3, H α : 900 s × 3	0.82 ± 0.09
AZT-22	SITe 2000 × 800	2003. 8. 18	F1, F2, F3, F4	<i>U</i> : 600 s, 15 s, <i>B</i> : 300 s, 7 s, <i>V</i> : 180 s, 5 s, <i>R</i> : 90 s, 5 s, <i>I</i> : 60 s, 5 s	0.98 ± 0.02
		2004. 12. 25	F5, F6, F7, F8	<i>U</i> : 600 s, 15 s, <i>B</i> : 300 s, 7 s, <i>V</i> : 180 s, 5 s, <i>R</i> : 90 s, 5 s, <i>I</i> : 60 s, 5 s	1.21 ± 0.14
		2004. 12. 30	F9, F10, F11	<i>U</i> : 600 s, 15 s, <i>B</i> : 300 s, 7 s, <i>V</i> : 180 s, 5 s, <i>R</i> : 90 s, 5 s, <i>I</i> : 60 s, 5 s	1.18 ± 0.17
			F12, F13, F14		
AZT-22	Fairchild 486 (SNUCam)	2007. 10. 7	C1	<i>U</i> : 600 s, 15 s, <i>B</i> : 300 s, 7 s, <i>V</i> : 180 s, 5 s, <i>I</i> : 60 s, 5 s, H α : 600 s, 30 s	1.5
		2009. 1. 19	C2	<i>U</i> : 600 s, 15 s, <i>B</i> : 300 s, 7 s, <i>V</i> : 180 s, 5 s, <i>I</i> : 60 s, 5 s, H α : 600 s, 30 s	0.9

Note.

^a Average and standard deviation of the FWHM of stellar profiles in long-exposure *V* images.

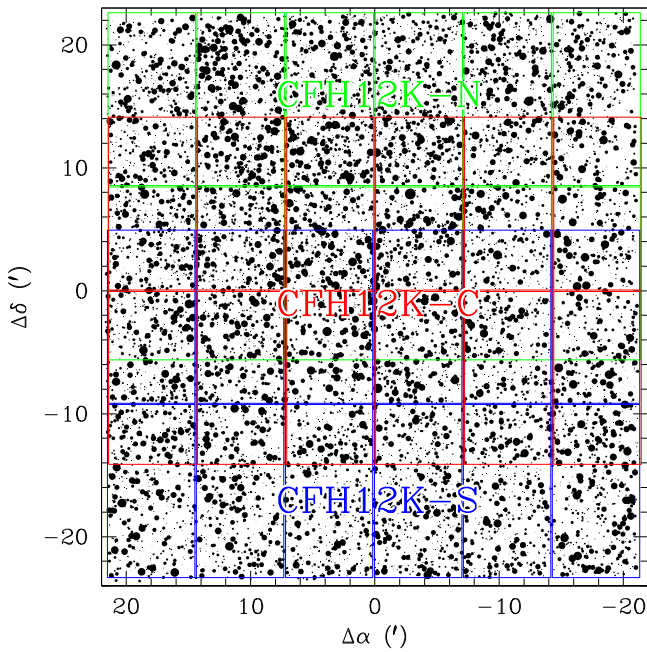


Figure 1. Finder chart of IC 1805 for the stars brighter than $I = 18$ from CFH12K observations. The size of the dots is proportional to the brightness of the star. Squares represent a schematic view of the CFH12K mosaic CCD camera, and three different pointings are drawn in different colors. The name of each pointing is given near the center of each region. The position of stars is relative to the brightest star HD 15558 [α (J2000) = $2^{\text{h}}32^{\text{m}}42^{\text{s}}.54$, δ (J2000) = $+61^{\circ}27'21''.6$].

standard colored glass filters (Bessell 1990). Transformation to the standard Johnson–Cousins *VRI* system requires a multi-linear transformation in *R*, and is well documented in Sung et al. (2008b).

The exposure times used on 2002 January 6 were 3×75 s in *I*, 3×150 s in *V* and *R*, and 3×1875 s in H α . On 2002 January 7, together with the long-exposure images, we also obtained a short-exposure image for each *VRI* filter to enable the photometry of bright stars. Unfortunately, due to the limited observing time for IC 1805 (the main target was NGC 2264—see Sung et al. 2008b), only one image for CFH12K-N and three images for CFH12K-S were obtained in H α . The exposure time used for H α on the second night was 900 s, and therefore the photometric depth in H α in the extreme north and extreme south ($|\Delta\delta| \gtrsim 14'$) is shallower than that for the central region. The mean value of the seeing was about $0''.8$ in the 150 s-exposure *V* images. The instrumental signatures were

removed using the IRAF/MSCRED package. Instrumental magnitudes were obtained using the IRAF/DAOPHOT package via point-spread function (PSF) fitting.

The instrumental magnitudes were transformed to the standard magnitudes and colors using the atmospheric extinction coefficients, transformation coefficients, and photometric zero-points summarized in Table 1 of Sung et al. (2008b). However, we did not apply the time variation of the photometric zero-points on the first half of 2002 January 6 because we found consistent magnitudes and colors between those observed on 2002 January 6 and 7 when we neglected the time variation coefficients. When we were checking the internal consistency of photometric data between CFH12K-N and CFH12K-S, the photometric data obtained from chip 08 of CFH12K-N (N08) showed a large shift in zero-points. The *V* magnitude zero-points were in relatively good agreement, but the *I* and *R* magnitudes were shifted by about 0.08 and 0.04 mag, respectively. We therefore corrected for the photometric zero-points for N08 by these amounts. The consistency of the photometric data from the three CFH12K pointings after this correction are shown in Figure 2 and summarized in Table 3. The difference between the data sets was calculated for relatively bright stars with $V \leq 21$ for ΔV and $\Delta(V - I)$, $I \leq 19.5$ for ΔI and $\Delta(R - I)$, respectively. The statistics were obtained from a successive exclusion scheme—the successive exclusion of data with a large difference ($> 2.5\sigma$) from the mean. The number in parenthesis indicates the number of stars excluded from the statistics. The three independent data sets agreed very well with each other.

2.1.1.2. Astrometry and 2MASS Counterparts

CCD coordinates were transformed to the equatorial coordinate system using the Two Micron All Sky Survey (2MASS) point-source catalog (Skrutskie et al. 2006), and all data finally merged into a catalog (called CFH12K) using the weighted averaging scheme described in Sung & Lee (1995). The number of stars in the catalog CFH12K (Table 2) is 91139. We included in the table, duplicity from PSF photometry and membership information, YSO class, 2MASS ID, *Spitzer* ID in Table 8, VSA ID (Vasilevskis et al. 1965), and spectral types from various sources. Ten stars in Table 2 may be listed twice due to a large difference in brightness ($\Delta I > 1$ mag) among three sets of data (e.g., C11519 and C11524, C51759 and C51760) or due to the problems in PSF deconvolution of a very close ($d \lesssim 0''.15$) double (e.g., C03096 and C03097, C17752 and C17755, C19384 and C19387, C20486 and

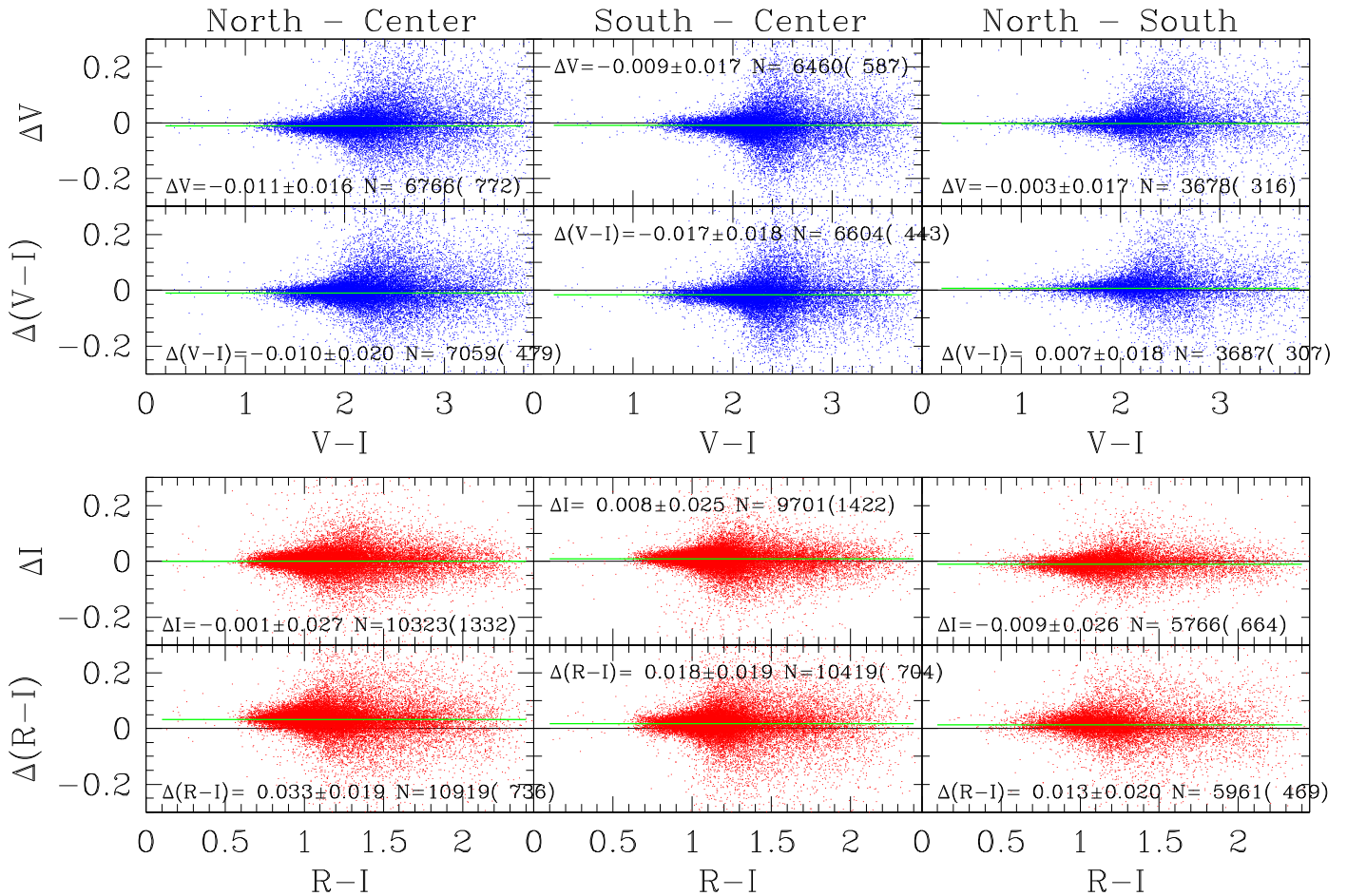


Figure 2. Internal consistency of CFH12K data. The meaning of Δ is shown above the first panel of each column. The statistics were obtained for the stars brighter than $V \leq 21$ mag for ΔV and $\Delta(V-I)$, and $I \leq 19.5$ mag for ΔI and $\Delta(R-I)$ from a successive exclusion of data with a large deviation ($>2.5\sigma$) from the mean. The number in parenthesis represents the number of stars excluded from the statistics.

C20491, C22238 and C22240, C23895 and C23897, C39867 and C39874, C53870 and C53877). Owing to the superior sky conditions of the CFHT observations, there are many cases of two or more stars being simultaneously identified as the optical counterpart of a 2MASS source within a matching radius of $1''.0$. If the difference in the I magnitude of two or three stars being matched with a 2MASS source was greater than 5 mag, we assigned the brightest star as the optical counterpart of the 2MASS source. If the difference in I was greater between 1 and 5 mag, we assigned the brighter (brightest) star as the optical counterpart of the 2MASS source and added “b” after 2MASS ID for the fainter star(s). If the difference in I was less than 1 mag, we added “A” and “B” for the brighter star and the fainter star, respectively. The same rule was applied for the *Spitzer* ID.

2.1.2. Maidanak AZT-22 1.5 m Observations

2.1.2.1. SITe 2000 × 800 CCD (Maidanak 2k) Observations

For a comprehensive study of IC 1805, the photometry of the bright blue stars was very important and therefore we decided to observe several regions in IC 1805 with the AZT-22 1.5 m telescope at the Maidanak Astronomical Observatory in Uzbekistan.

UBVRI CCD observations of IC 1805 were performed on 2003 August 18 (Region: F1–F4), 2004 December 24 (F5–F8), and 2004 December 30 (F9–F14) at the Maidanak

Astronomical Observatory with the AZT-22 1.5 m telescope and a thinned SITe 2000 × 800 CCD ($15 \mu\text{m}$ pixels; pixel scale = $0''.265/\text{pixel}$). The observed regions are shown in Figure 3. Two sets of exposure times were used in the observations—long: 60 s in I , 90 s in R , 180 s in V , 300 s in B , 600 s in U , and short: 3 s in I , R and V , 5 s in B , 15 s in U . The seeing was relatively good ($1''.0$ – $1''.2$). Because we did not observe many standard stars at various air masses, we used as secondary standard stars those stars common with the SNUCam FOV in the determination of atmospheric extinction coefficients and photometric zero-points. These coefficients are listed in Table 4. The transformation to the SAAO standard system was performed using the coefficients described in Lim et al. (2009). As can be seen in Table 3, the photometric zero-points of the CFH12K and SNUCam data differ by about 3% in V and I . The photometric zero-points for V and I were adjusted to those of CFH12K, but those for $(B-V)$ and $(U-B)$ were adjusted to those of the SNUCam data.

A total of 5319 stars were measured and listed in Table 5 (we refer to this data set as “Maidanak2k”). Among them, 5121 stars were matched with a single object in Table 2, 145 stars were matched with two objects, and two stars were matched with three stars within a matching radius of $0''.7$, and 51 objects had no counterpart in the CFH12K catalog. Forty nine objects were bright stars ($I < 15$ mag). The star M2k3582 is located

Table 2
Photometric Data from CFHT Observations^a

ID	α_{J2000}	δ_{J2000}	V	I	$R-I$	$V-I$	$R-H\alpha$	ϵ_V	ϵ_I	ϵ_{R-I}	ϵ_{V-I}	$\epsilon_{R-H\alpha}$	N_{obs}				D^b	M^c	Class ^d	2MASS ID ^e	<i>Spitzer</i> ID ^f	VSA ^g	Sp. Type	
C79360	2:34:56.37	61:17:17.1	...	21.325	1.281	0.010	0.022	0	6	6	0	0	F	...	S084685
C79361	2:34:56.38	61:21:12.1	22.014	19.651	1.143	2.359	-3.179	0.007	0.013	0.003	0.018	0.013	6	7	7	6	5	S084690
C79362	2:34:56.39	61:44:44.0	22.420	20.191	1.065	2.226	-2.855	0.031	0.013	0.016	0.033	0.049	3	4	3	3	1
C79363	2:34:56.39	61:15:43.5	17.723	16.180	0.719	1.535	-2.987	0.011	0.014	0.008	0.028	0.002	7	7	7	7	6	02345637+6115433	S084683
C79364	2:34:56.39	61:44:01.2	18.650	17.064	0.779	1.585	-3.014	0.001	0.004	0.004	0.004	0.004	4	4	4	4	1	02345637+6144011	S084695
C79365	2:34:56.39	61:29:05.4	...	20.878	1.415	0.007	0.030	0	11	9	0	0	S084696
C79366	2:34:56.39	61:38:09.3	21.250	19.261	1.004	2.004	-2.987	0.005	0.009	0.007	0.003	0.005	6	7	7	6	4	S084688
C79367	2:34:56.39	61:33:22.0	17.357	15.585	0.830	1.779	-3.005	0.007	0.001	0.008	0.003	0.009	7	7	7	7	4	4	02345640+6133220	S084692
C79368	2:34:56.39	61:40:19.7	23.418	21.333	1.111	2.109	...	0.091	0.039	0.051	0.107	...	1	6	6	1	0
C79369	2:34:56.40	61:27:28.6	...	21.577	1.794	0.004	0.061	0	9	2	0	0
C79370	2:34:56.40	61:23:57.4	21.478	18.252	1.589	3.212	-2.123	0.069	0.015	0.027	0.081	0.029	10	11	11	10	7	...	H	3	02345637+6123576A	S084691A
C79371	2:34:56.41	61:30:55.7	14.296	13.575	0.373	0.734	...	0.016	0.022	0.024	0.000	...	2	2	2	2	0	4	02345640+6130556	S084694	281	B5
C79372	2:34:56.41	61:32:37.4	22.635	20.505	1.047	2.099	-3.020	0.028	0.006	0.034	0.027	0.044	6	7	6	6	4
C79373	2:34:56.41	61:32:30.3	20.568	18.828	0.855	1.737	-3.001	0.011	0.006	0.034	0.005	0.011	7	7	7	7	4	S084697
C79374	2:34:56.42	61:19:51.5	23.375	20.943	1.201	2.408	...	0.000	0.012	0.012	0.017	...	5	7	6	5	0
C79375	2:34:56.44	61:35:45.5	23.138	21.043	1.074	2.096	-2.829	0.013	0.005	0.012	0.017	0.070	6	7	6	6	3
C79376	2:34:56.44	61:44:21.2	22.188	20.096	1.034	2.092	-2.954	0.018	0.013	0.015	0.022	0.035	3	4	3	3	1
C79377	2:34:56.44	61:38:26.0	...	21.410	1.642	0.012	0.014	0	6	5	0	0
C79378	2:34:56.45	61:19:20.5	...	21.756	1.340	0.002	0.104	0	6	3	0	0
C79379	2:34:56.46	61:06:25.6	...	21.181	1.372	0.016	0.022	0	3	3	0	0	S084713
C79380	2:34:56.46	61:28:52.7	...	22.194	0.075	0	3	0	0	0

Notes.

^a Units of right ascension are hours, minutes, and seconds of time, and units of declination are degrees, arcminutes, and arcseconds.

^b Duplicity—D: stars for which the PSF shows a double, but measures as a single star, G: galaxy.

^c Membership—X: X-ray emission star, x: X-ray emission candidate, H: H α emission star, h: H α emission candidate, “+” = X + H, “-” = X + h.

^d YSO class—1: Class I, F: flat spectrum, 2: Class II, 3: Class III, 4: Class IV, t: star with pre-transition disks, T: star with transition disks, P: stars with PAH emission, g: photometric galaxy candidates, ?: two or more stars are identified as the optical counter parts of a *Spitzer* source.

^e A, B, or b are added at the end of 2MASS ID if two or more stars are matched with a 2MASS source within a matching radius of 1". A or B: the bright or faint component of a 2MASS source whose I magnitude difference is less than 1 mag. b: the faint component of a 2MASS source whose I magnitude difference is greater than 1 mag.

^f A, B, or C are added at the end of *Spitzer* ID if two or more stars are matched with a *Spitzer* source within a matching radius of 1".

^g ID from Vasilevskis et al. (1965).

(This table is available in its entirety in machine-readable form.)

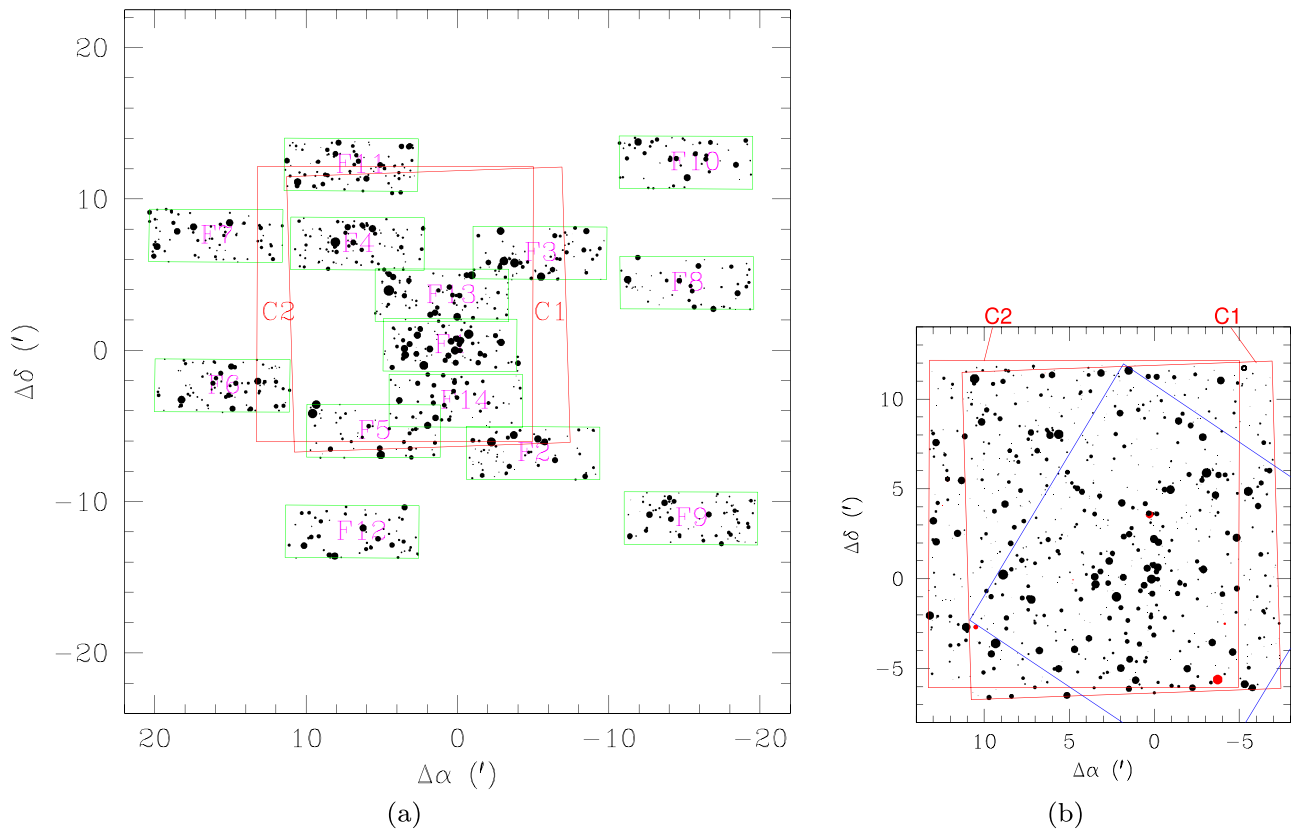


Figure 3. Finder chart for the stars brighter than $I = 16$ mag (or $V = 17.8$ mag) from (a) Maidanak 2k observations and (b) SNUCam observations. The size of the dot is proportional to the brightness of the star. Red dots in (b) represent $H\alpha$ emission stars. Fourteen green rectangles represent the fields of view (FOVs) of 14 regions observed with the Maidanak 2k CCD, while two red squares denote the FOVs of two regions observed with the SNUCam CCD. The blue diamond in (b) represents the FOV of the *Chandra* X-ray observation. The origin ($\Delta\alpha = 0.0$, $\Delta\delta = 0.0$) is the position of the brightest star in IC 1805 HD 15558.

just south of M2k3581 (= VSA 199, G7Ib), and was on the saturated portion of the CFH12K images. The other object M2k4020 is an extended source, and was classified as a galaxy candidate “G” in the Maidanak2k data. This source was rejected in the CFH12K images probably because of its higher χ or sharpness value. The difference in photometry between the SNUCam and Maidanak2k data is shown in Figure 4 (left and middle panels) and Table 3. The difference in V and I was -0.033 and -0.024 mag, respectively. This means that the SNUCam data were about 3% brighter than the CFH12K data as the Maidanak2k data were adjusted to the CFH12K data. On the other hand, the $(V-I)$ and $(B-V)$ colors for $V \leq 17$ mag were consistent with each other. However, $\Delta(U-B)$ for $V \leq 16$ mag showed abnormal behavior. Although the mean value of the difference was very close to 0.0, there was a systematic difference, which was related to the Balmer jump of A–F stars. Because the SITe 2000×800 CCD and U filter combination do not require a nonlinear correction (Lim et al. 2009), the nonlinear difference in $\Delta(U-B)$ is caused solely by the nonlinear correction term in the U transformation of the Fairchild 486 CCD and U filter combination (see Lim et al. 2009, 2015a). More discussion on this issue will be dealt with in the following section.

2.1.2.2. Fairchild 486 CCD (SNUCam) Observations

$UBVI$ and $H\alpha$ CCD photometry for the central region of IC 1805 was obtained on 2007 October 7 (C1 region) and 2009 January 19 (C2 region) at the Maidanak Astronomical Observatory with the AZT-22 (1.5 m) telescope ($f/7.74$) and

a thinned Fairchild 486 CCD ($15 \mu\text{m}$ pixels) as a part of the Sejong Open-cluster Survey (Sung et al. 2013a). The observed regions are shown in Figure 3. The filters and exposure times used in the observations were the same as those used for the observations of IC 1848 (Lim et al. 2014a). The seeing was good on 2009 January 19 (about $0''.9$ in $V180$ s image), and moderate on 2007 October 7 ($1''.5$).

All the preprocessing needed to remove the instrumental signature was done using the IRAF/CCDRED package. Instrumental magnitudes were obtained using IRAF/DAOPHOT via PSF fitting for the target images and via simple aperture photometry for standard stars. All the instrumental magnitudes were transformed to the standard $UBVI$ system using SAAO photometry of equatorial standard stars (Menzies et al. 1991) and blue and red standard stars in Kilkenny et al. (1998). Details of the transformations to the standard system can be found in Lim et al. (2009). Individual data were compared with the CFH12K data, and showed that the brightness of stars at $r > 5'$ from the center of the FOV were fainter, especially in I , probably because of a large variation in the PSF at the edge of the CCD chip (Lim et al. 2008). CCD coordinates were transformed to the equatorial coordinate system by identifying the optical counterpart of 2MASS point sources (Skrutskie et al. 2006). Two sets of SNUCam data were merged into a photometric catalog (SNUCam data).

We also identified the stars in Table 6 with those in Table 2 using a matching radius of $0''.7$. Among 7011 stars in the SNUCam data, 6804 stars had one counterpart in the CFH12K catalog. Due to the superior sky condition at Mauna Kea, 162

Table 3
Internal Consistency of Optical Photometric Data^a

Reference	Target	ΔV	$n(n_{\text{ex}})^b$	$\Delta(V - I)$	$n(n_{\text{ex}})^b$	V range	ΔI	$n(n_{\text{ex}})^b$	$\Delta(R - I)$	$n(n_{\text{ex}})^b$	I range
CFH12K-C	CFH12K-N	-0.011 ± 0.016	6766 (772)	-0.010 ± 0.020	7059 (479)	≤ 21	-0.001 ± 0.027	10323 (1332)	$+0.033 \pm 0.019$	10919 (736)	≤ 19.5
CFH12K-C	CFH12K-S	-0.009 ± 0.017	6460 (587)	-0.017 ± 0.018	6604 (443)	≤ 21	$+0.008 \pm 0.025$	9701 (1422)	$+0.018 \pm 0.019$	10419 (704)	≤ 19.5
CFH12K-S	CFH12K-N	-0.003 ± 0.017	3678 (316)	$+0.007 \pm 0.018$	3687 (307)	≤ 21	-0.009 ± 0.026	5766 (664)	$+0.013 \pm 0.020$	5961 (469)	≤ 19.5
CFH12K	Maidanak 2k	$+0.000 \pm 0.017$	427 (37)	$+0.000 \pm 0.022$	430 (34)	≤ 17	$+0.007 \pm 0.022$	991 (81)	-0.005 ± 0.036	1032 (27)	≤ 16.5
CFH12K	SNUCam	$+0.036 \pm 0.020$	388 (45)	$+0.015 \pm 0.026$	416 (15)	≤ 17	$+0.031 \pm 0.020$	868 (128)	≤ 16.5
SNUCam	Maidanak2k	-0.033 ± 0.020	260 (24)	-0.012 ± 0.021	268 (16)	≤ 17	-0.024 ± 0.024	516 (60)	≤ 16.5
		$\Delta(B - V)$	$n(n_{\text{ex}})^b$	$\Delta(U - B)$	$n(n_{\text{ex}})^b$	V range	$\Delta(U - B)$	$n(n_{\text{ex}})^b$	range		
SNUCam	Maidanak2k	$+0.005 \pm 0.022$	165 (119)	-0.016 ± 0.053	165 (6)	... ^c	$+0.013 \pm 0.033$	54 (2)	$V \leq 17$ & $(U - B) \leq 0.0$		

Notes.

^a Δ denotes the difference—reference minus target.

^b The number of stars excluded in the comparison is shown in parenthesis.

^c $V \leq 17$ for $(B - V)$ and $V \leq 16$ for $(U - B)$.

objects in the SNUCam data had two counterparts in the CFH12K catalog, and 2 objects had three counterparts. However, 43 stars had no counterpart in the CFH12K catalog. Among them, 37 stars were bright ($I < 15$ mag) and not measured because of saturation. Three objects were matched with two objects in the CFH12K catalog just outside the matching radius, one object had a counterpart just outside the matching radius, and the other two objects were missed because of their closeness to bright saturated stars (M4k0305 on the spike of BD +60 497 and M4k2398 near HD 15570).

We calculated the difference in photometry between the SNUCam data and CFH12K data or Maidanak2k data for the stars within a $5'$ radius from the center of the SNUCam FOV, and presented them in Table 3 and Figure 4 (right panel). SNUCam data were systematically brighter by about 3% in V and I than CFH12K data. Such a small, but systematic difference in zero-points may be related to the standard stars used in the standard transformation (the Stetson version of the Landolt standard system for CFH12K and the SAAO standard system for SNUCam data). A similar difference was found in Sung et al. (2008b). The difference in $(B - V)$ between the Maidanak 2k and SNUCam data was very small as the photometric zero-points of the Maidanak 2k data were adjusted to those of the SNUCam data. On the other hand, as mentioned in Section 2.2.1 the difference in $(U - B)$ was slightly curved, caused by the nonlinear correction term in the U transformation of the SNUCam data. The size of the nonlinear correction depends both on the size of the Balmer jump and the steep variation of the quantum efficiency of the CCD chip between $\lambda\lambda 3000\text{--}4000 \text{ \AA}$, and so is strongly affected by the amount of reddening. For early-type stars it is very easy to calculate the amount of reddening, but is not as easy for intermediate- or late-type field stars because their colors are affected both by metallicity and gravity. Because we have no information on the reddening of field stars, we had to apply the mean reddening for these stars, which could cause an over- or under-correction of the reddening effect.

2.1.3. Comparison of Optical Photometry

Three sets of photometric data were compared with existing photoelectric photometry and modern CCD photometry. The results are summarized in Table 7 and a few of them are shown in Figure 5. For the data comparison, we used a successive exclusion scheme for data that deviated from the mean by more

than 2.0σ for the photoelectric photometry and 2.5σ for the CCD photometry. The reason for using a different threshold is that photoelectric photometry is more vulnerable to a sudden change in the sky conditions. Photoelectric photometric data were mostly brighter than CFH12K data or Maidanak 2k data by 0.04–0.08, and than SNUCam data by about 0.01–0.05 mag in V with a scatter of about 0.02–0.05 mag. Although only three stars were in common with Johnson and/or Hiltner (Johnson & Morgan 1955; Hiltner 1956; Hiltner & Johnson 1956; Johnson & Hiltner 1956), they were consistent with SNUCam data. On the other hand, the photoelectric data of Joshi & Sagar (1983) were well consistent with the SNUCam data photometric zero-points, but many data were excluded in the statistics because of large deviations.

Figures 5(b)–(d) show the differences between the SNUCam data and CCD photometry by various authors. As Sung & Lee (1995) transformed their CCD data to the standard system using photoelectric photometric data from Hoag et al. (1961) for UBV and Guetter & Vrba (1989) for $(V - I)$, the differences are very similar to those of the photoelectric photometry. The SNUCam data are consistent with the CCD data of Massey et al. (1995). However, the large scatter in the comparison is related to the brightness range used in the comparison, and is probably caused by the relatively short-exposure time used by Massey et al. (1995).¹⁰ On the other hand, the comparison between the SNUCam data and those of Ninov et al. (1995) shows a very strange pattern. Although the difference in V is very close to zero for bright stars, it is systematically fainter for faint stars ($V \geq 15$ mag). In addition, the I magnitude shows an offset by about 0.25 mag for bright stars ($I \leq 14$ mag), but the difference increases for fainter stars. Such an offset is related to the difference between the Cousins and Johnson I magnitude systems because they transformed the $(V - I)$ of Guetter & Vrba (1989) to Johnson's $(V - I)$ using the relation given by Bessell (1979). The curved feature in Figure 5(d) may be related either to the nonlinear response of the CCD chip they used (Kodak KAF-4200) at the faint regime or to improper sky subtraction.

¹⁰ Although they did not mention the exposure time explicitly, the scatter increases rapidly for $V \geq 14$ mag in the comparison with our CFH12K data or SNUCam data.

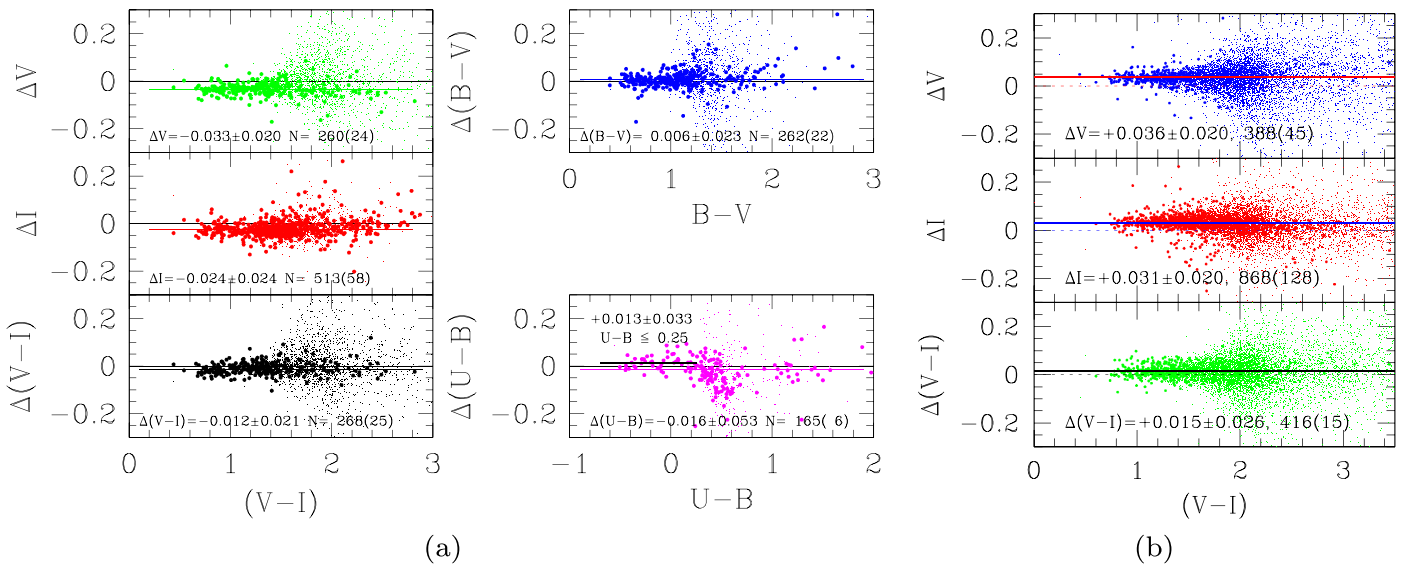


Figure 4. Comparison of Photometry. Δ means (a) SNUCam data minus Maidanak2k data (left and middle panels) and (b) CFH12K data minus SNUCam data (right panel). Large dots represent data for relatively bright stars [$V \leq 17$ for V and $(B - V)$, $V \leq 16$ for $(U - B)$, and $I \leq 16.5$ for I and $(V - I)$].

2.2. Spitzer MIR Observations and Data Reduction

2.2.1. Spitzer Observations of IC 1805

Deep optical photometry of IC 1805 reveals that $H\alpha$ emission stars are distributed across the whole FOV of the CFH12K observations (see Figure 14). To confirm whether the distribution of PMS stars with $H\alpha$ emission is real or not, we decided to reduce the *Spitzer* MIR images. The *Spitzer* mapping observations were performed under program ID 20052 (PI: S. Wolff) in 9×9 mosaics. Each pointing was imaged in the high dynamic range mode (exposure time: 0.4 s and 10.4 s). The mapping of IC 1805 was performed on 2006 September 20. We refer to the region as “SST/CM.” The Astronomical Observation Request (AOR) utilized for this map was number 13846016. For complete photometry of stars in the CFH12K FOV in 3.6 and 4.5 μm , we also downloaded and reduced the GLIMPSE360 data (AOR: 38753280, 38763264, 38769408, 38799104, 38798592, 38784512, PI: B. A. Whitney).

MIPS scans of IC 1805 were obtained on 2005 August 31 and 2005 September 2 (PID 3234, PI: J. S. Greeves) at the fast scan rate (exposure time: 2.62 s). Twenty-five scans of 1.00 length, with 300 offsets, were used. The observed area is much larger than the FOV of CFH12K. The AORs utilized for the MIPS mapping were numbers 10498304 and 10498048. Three MIPS Phot images (AOR: 13846272, 13846528, 13846784, PI: S. Wolff) were also used. The post-BCD (basic calibrated and mosaicked) images were downloaded from the *Spitzer* heritage archive.¹¹ The pixel size of the IRAC post-BCD data is $0''.6 \times 0''.6$, while that of the MIPS 24 μm data is $2''.45 \times 2''.45$. The data utilized pipeline processing software version S18.7.0 for the IRAC (cool mission) images, S19.1.0 for GLIMPSE360 images, and S18.12.0 for the MIPS 24 μm image.

2.2.2. Photometry

We used the IRAF version of DAOPHOT to derive PSF-fitting photometry for the stars in the field of IC 1805. Because

Spitzer IRAC images are undersampled, PSF fitting yields photometry with relatively poor signal-to-noise. For uncrowded fields with little nebulosity, aperture photometry would provide photometry with lower noise than PSF-fitting photometry for IRAC data. However, portions of the IC 1805 field are crowded, or have highly variable and strong nebulosity, or both. We believe that PSF-fitting photometry provides more uniform and reliable photometry than aperture photometry, admittedly at the expense of having more noise for stars where the backgrounds are benign and crowding is not an issue. For most stars in the cluster, because we have four independent sets of data, the PSF-fitting photometric accuracy is improved by averaging the results from the separate AORs. Details for the data reduction can be found in Sung et al. (2009). We found that IRAS 02260+6118 (=S022094, YSO class: F) is a point source in 3.6 and 4.5 μm images, but an extended source in 5.8 and 8.0 μm images.

The FOVs of the *Spitzer*/IRAC and MIPS, CFH12K optical, *Chandra*, and *XMM-Newton* X-ray observations are shown in Figure 6. The FOV covered by the stars measured is the combination of the FOVs of AOR 13846016 (cool mission), a full strip of the GLIMPSE360 survey—AORs 38753280, 38763264, 38769408, 38799104, and a small portion of AORs 38798592, 38784512 as shown in Figure 6. The weighted mean values and weighted errors of the magnitudes from multiple observations were calculated as in Sung & Lee (1995; weight = $1/\epsilon^2$). We present the photometric data for four IRAC bands and the MIPS 24 μm band for 101,746 objects in Table 8. The distribution of photometric errors is shown in Figure 7. As the *Spitzer*/IRAC images are undersampled data, the photometric errors are no better than 0.1 mag, even for bright stars (e.g., $[3.6] < 10$ mag). However, as several epochs of data with two exposure times per epoch are available, the resulting final error is small if the magnitudes from all images are consistent (e.g., stars with $\epsilon \approx 0.0$ at $[3.6] > 14$ mag). If not, the resulting error will be larger (e.g., stars with $\epsilon > 0.1$ at $[3.6] \approx 13.7$ mag). The abrupt increase in photometric errors at $[3.6] \approx 14$, $[4.5] \approx 13$, and $[5.8] \approx [8.0] \approx 12$ is due partly to a large intrinsic error from short-exposure images and partly to a large difference in photometry from short and long exposed

¹¹ <http://sha.ipac.caltech.edu/applications/Spitzer/SHA/>

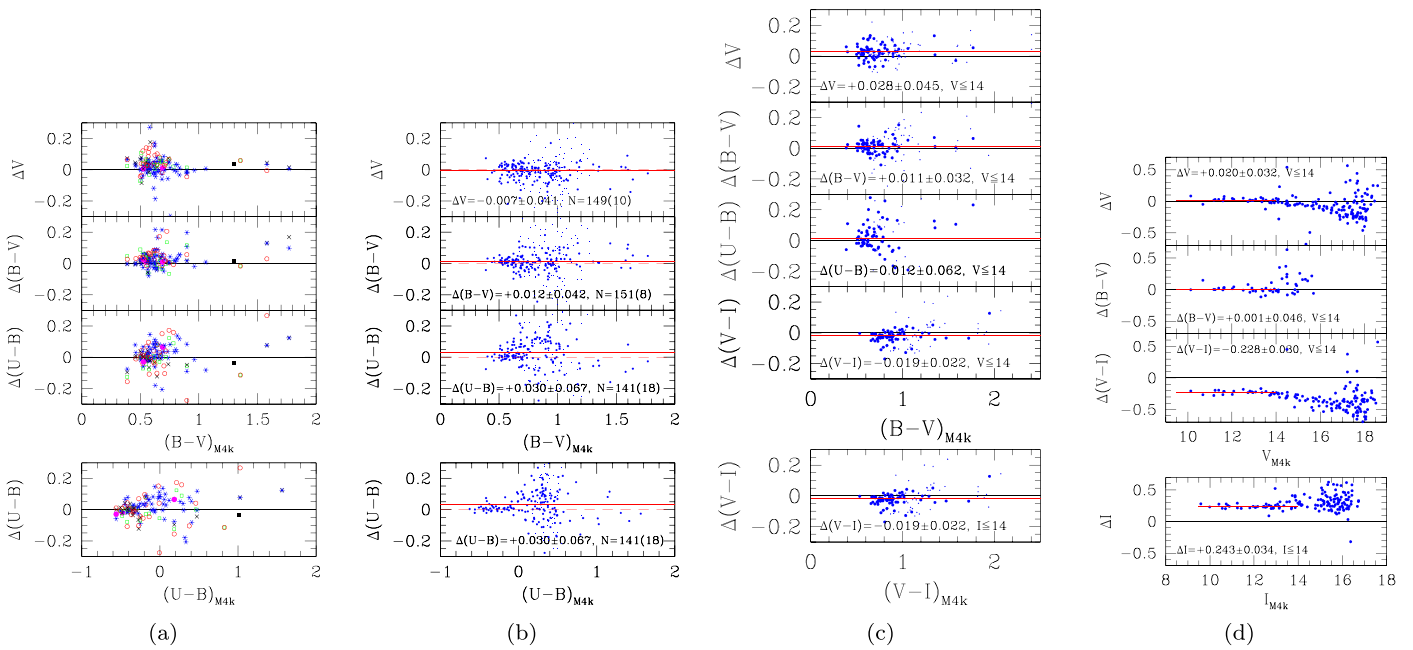


Figure 5. Comparison of photometry. Δ denotes SNUCam data minus others. (a) Photoelectric photometry—magenta dots: Johnson & Morgan (1955), Johnson & Hiltner (1956), Hiltner & Johnson (1956), Hiltner (1956), black square: Guetter & Vrba (1989), black cross: Ishida (1969), blue asterisk: Joshi & Sagar (1983), green open square: Hoag et al. (1961), red circle: Kwon & Lee (1983), (b) CCD photometry by Massey et al. (1995), (c) CCD photometry by Sung & Lee (1995), and (d) CCD photometry by Ninov et al. (1995). Large and small dots in (b), (c), and (d) represent bright stars used in statistics and fainter stars, respectively.

images. Such a trend can be seen in Figure 7. We label the objects in Table 8 as “S” + the identification number in the first column. The total number and faint limit of objects detected from the photometry are 100082 stars and 18.3 mag for [3.6], 100989 stars and 18.0 mag for [4.5], 11092 stars and 16.0 mag for [5.8], 5433 stars and 15.0 mag for [8.0], and 523 stars and 9.8 mag for [24], respectively. We included in the table, the YSO class (see Section 3.2), membership information ($H\alpha$ or/and X-ray emission—see Section 3), duplicity from the PSF fitting process, 2MASS identification, and any optical counterpart.

We compared our data with Wolff et al. (2011) who published *Spitzer*/IRAC and MIPS data for 974 objects. Among them, 14 objects were listed twice. We also found no counterpart in our data for 110 of their objects. Most of them (83 objects) were outside our FOV shown in Figure 6. Twenty-five objects that had no counterpart in our catalog also had no counterparts in 2MASS, and were mostly faint ($[3.6] > 14$ mag). They may therefore be spurious detections, such as cosmic-ray events. Two objects not in our catalog are the bright K2III star BD+60 519 and its neighbor, due to severe saturation of BD+60 519. For objects in common with Wolff et al. (2011), the differences relative to our photometry are $+0.011 \pm 0.030$ mag ($N = 571$, 78 excluded), $+0.000 \pm 0.028$ mag ($N = 574$, 98 excluded), -0.006 ± 0.051 mag ($N = 549$, 104 excluded), $+0.022 \pm 0.099$ mag ($N = 552$, 119 excluded), and -0.093 ± 0.225 mag ($N = 34$, 5 excluded) in [3.6], [4.5], [5.8], [8.0], and [24], respectively. The consistency of the photometric zero-points between the two data sets is good, but the scatter increases for fainter stars.

2.3. X-Ray Observations

2.3.1. Chandra X-Ray Observatory Observations

The *Chandra* X-ray Observatory Observations of IC 1805 (ObsID: 7033, PI: L. Townley) were made on 2006 November 25. The total exposure time was about 79ks. The properties of

647 X-ray sources were published in Townsley et al. (2014), which is part of “the Massive Young Star-forming Complex Study in Infrared and X-Ray (MYStIX) Project” (Feigelson et al. 2013). We searched for the optical and MIR counterparts of these X-ray sources with a matching radius of up to $1''.5$. If the candidate was the closest object within a matching radius of $1''.0$, we considered the object to be the optical (MIR) counterpart of the X-ray source and assigned the membership “X.” The second closest object, or the closest object within $1''.5$ from the X-ray source, was considered to be a candidate X-ray emission object, and assigned the membership “x.” The membership information is included in Tables 2–8. Among 647 X-ray sources, 194 objects had no counterpart in our optical source catalogs and MIR source list within a matching radius of $1''.5$ (232 objects within $1''.0$). Twenty-six X-ray sources had only *Spitzer* MIR counterparts.

Townsley et al. (2014) also released the median X-ray energy of the X-ray sources. The median energy distribution of the 194 X-ray sources with no optical and MIR counterpart showed two peaks with a more than 10% fraction in a 0.5 keV bin (see the left panel of Figure 8). The median value of the median energy was 2.8 (± 1.5) keV with the stronger one at 1.0–2.0 keV, and the second one at 2.5–4.0 keV. On the other hand, the 26 X-ray sources detected only in the MIR *Spitzer* observations showed a different distribution with a single peak near 3.0 (± 0.8) keV, which corresponds to the second peak of the X-ray sources without a counterpart in this study. The median value of the median X-ray energy of stars with X-ray emission only (i.e., no emission in $H\alpha$), was 1.5 (± 0.6) keV. However, that of stars with emission in both $H\alpha$ and X-ray was slightly harder (1.7 ± 0.5 keV), that may be related to the relatively larger column density of the surrounding circumstellar materials. A similar pattern of X-ray energy distribution can be found from the median values among different YSO classes (see Section 3.2 for YSO classification). The YSO classes I, F, II, t, T, and g, which are definite members of IC 1805, had slightly higher

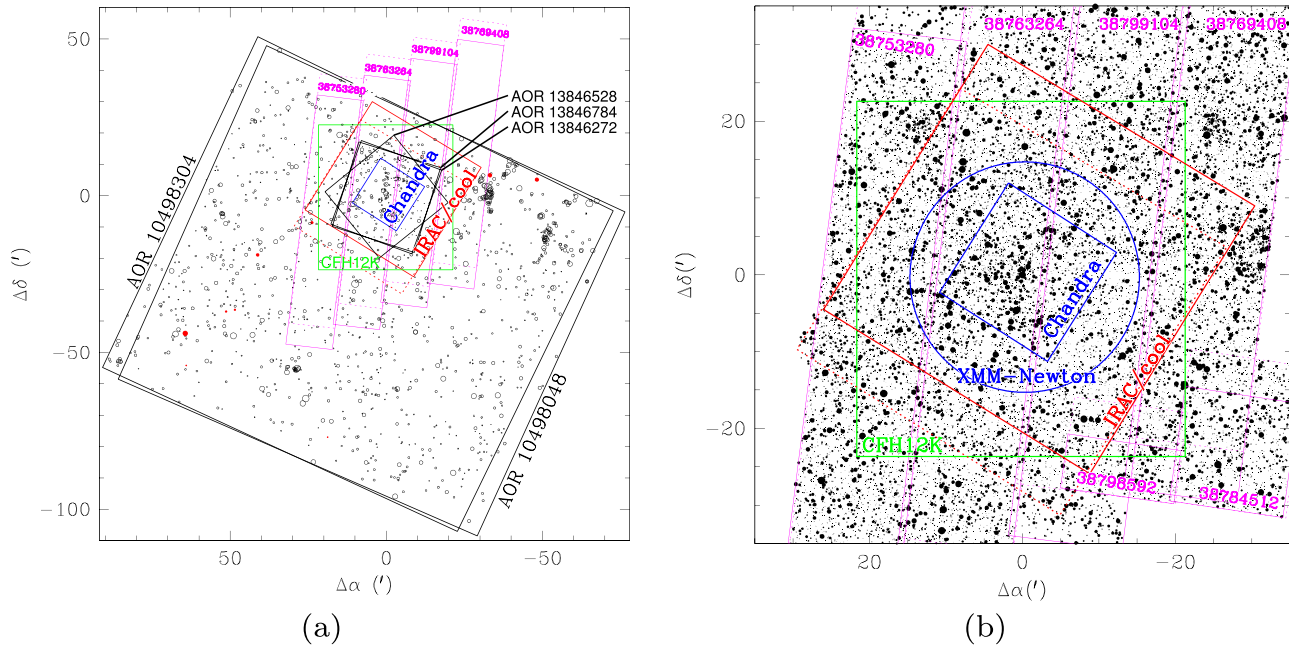


Figure 6. Fields of view of the *Spitzer* MIR, *Chandra* and *XMM-Newton*, and CFH12K optical observations. (a) Black, red, magenta, green, and blue squares indicate the FOVs of *Spitzer*/MIPS 24 μm observations, *Spitzer*/IRAC cool mission observations, *Spitzer*/IRAC GLIMPSE360 survey, CFH12K, and *Chandra* X-ray observations, respectively. The solid and dotted lines for the *Spitzer*/IRAC FOVs denotes the FOVs of IRAC 3.6 μm (and 5.8 μm) and 4.5 μm (and 8.0 μm), respectively. The size of the circles is proportional to the 24 μm brightness. Red dots represent extended sources from PSF fitting. (b) Central portion of (a). A blue circle denotes the FOV of the *XMM-Newton* observations. The size of dots is proportional to the brightness in 3.6 μm or 4.5 μm . The number in each strip is the AOR of the GLIMPSE360 images.

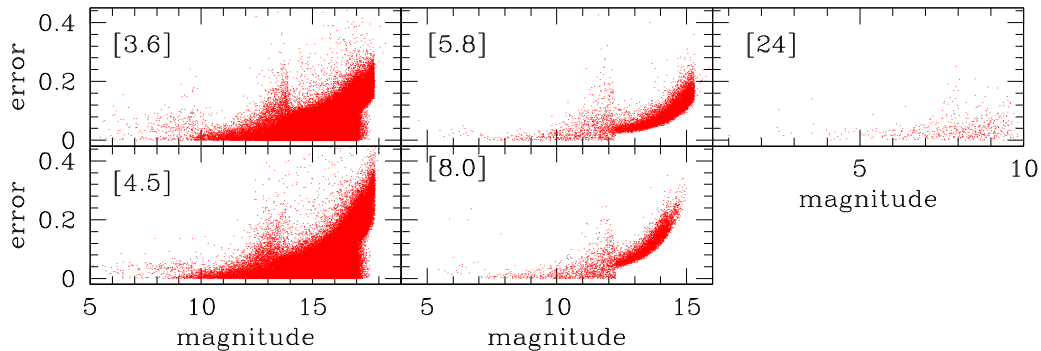


Figure 7. Distribution of photometric errors as a function of magnitude.

X-ray temperatures ($\langle E \rangle_{\text{med}} = 1.7 \pm 0.7$ keV, $N = 48$) (red crosses in the right panel of Figure 8). While the median values of Class III and Class IV objects (green plus and blue solid line, respectively, in Figure 8) were $1.5 (\pm 0.5)$ keV ($N = 43$) and $1.5 (\pm 0.4)$ keV ($N = 231$), respectively.

2.3.2. *XMM-Newton* Observations

XMM-Newton observations of IC 1805 were conducted in 2014 August for a single snapshot of 48ks duration (ObsID: 0740020101, PI: G. Rauw). The data were reduced using SAS v14 (see Rauw & Nazé (2016) for more detail). Source detection was performed using the task EDETECT_CHAIN on both soft (0.4–2.0 keV) and hard (2.0–10.0 keV) band images and for all three EPIC cameras. This task first searched for sources using sliding boxes, then applied a PSF fitting to yield the best positions and equivalent on-axis count rates. It was run for a likelihood detection of 10, both with and without considering the possibility of extended sources, and simultaneously fitting up to five neighboring sources, but the results

were similar in both cases. A total of 191 sources were found, 9 of them appearing potentially problematic (e.g., due to their position in a CCD gap, or in the PSF wings of a brighter source). A more detailed study of the X-ray properties of these sources was dealt with in Rauw & Nazé (2016).

We searched for the optical, *Spitzer* MIR, and *Chandra* X-ray source counterparts for the *XMM-Newton* X-ray sources with a matching radius of up to 6'' (mostly less than 4''). Among 191 *XMM-Newton* sources, 174 optical sources (stars or galaxies) were identified as optical counterparts for 167 *XMM-Newton* X-ray sources, 182 *Spitzer* MIR sources were identified as MIR counterparts of 175 *XMM-Newton* sources. Among 143 *XMM-Newton* sources within the FOV of *Chandra* X-ray observation, 130 sources were matched with one or two *Chandra* X-ray sources (141 X-ray sources in MYStIX catalog). Thirteen *XMM-Newton* sources had no counterpart in the MYStIX catalog, and therefore may be spurious detections or X-ray sources with strong variability. Four *XMM-Newton* sources had no counterpart in the optical, near-infrared (NIR) 2MASS, and MIR catalogs.

Table 4
Extinction Coefficients, Time-variation Coefficients, and Photometric Zero-Points at the Maidanak Astronomical Observatory

Date of Obs. CCD	Standard Stars or regions	Filter	$k_{1\lambda}$	$k_{2\lambda}$	$\alpha_{t,\lambda}$	ζ_λ
2003. 8. 18 SITe 2000 × 800	SA 111, SA 112 SA 113, SA 114 BD-11 162 (PG1633+099)	<i>I</i>	0.081 ± 0.020	...	0.0000	22.717 ± 0.011
		<i>R</i>	0.180 ± 0.034	23.095 ± 0.018
		<i>V</i>	0.250 ± 0.020	...	-0.0060	23.167 ± 0.009
		<i>B</i>	0.303 ± 0.022	0.026	0.0000	22.969 ± 0.012
		<i>U</i>	0.552 ± 0.018	0.023	0.0030	21.320 ± 0.005
2004. 12. 24 SITe 2000 × 800	SA 113, SA 114	<i>I</i>	0.114 ± 0.011	23.202 ± 0.006
		<i>R</i>	0.154 ± 0.012	23.373 ± 0.007
		<i>V</i>	0.235 ± 0.018	23.606 ± 0.011
		<i>B</i>	0.359 ± 0.025	0.026	...	23.538 ± 0.014
		<i>U</i>	0.609 ± 0.036	0.023	...	21.914 ± 0.023
2004. 12. 30 SITe 2000 × 800	SA 92, SA 97 SA 98, SA 114	<i>I</i>	0.110 ± 0.020	...	0.0063 ± 0.0018	23.198 ± 0.012
		<i>R</i>	0.174 ± 0.069	...	0.0140	23.436 ± 0.019
		<i>V</i>	0.229 ± 0.016	...	0.0018 ± 0.0015	23.586 ± 0.010
		<i>B</i>	0.369 ± 0.016	0.026	...	23.525 ± 0.008
		<i>U</i>	0.688 ± 0.043	0.026	...	21.997 ± 0.023
2007. 10. 7 Fairchild 486	SA 92, SA 95 SA 96, SA 98 SA 110, SA 113 SA 114, BD-11 162	<i>I</i>	0.024 ± 0.011	...	0.0038 ± 0.0010	22.678 ± 0.014
		<i>V</i>	0.131 ± 0.006	...	0.0023 ± 0.0007	23.192 ± 0.008
		<i>B</i>	0.246 ± 0.009	0.035 ± 0.005	0.0039 ± 0.0011	23.021 ± 0.013
		<i>U</i>	0.405 ± 0.012	0.011 ± 0.007	0.0070 ± 0.0014	21.154 ± 0.016
		H α	0.043 ± 0.004	19.403 ± 0.036
2009. 1. 19 Fairchild 486	SA 93, SA 96 SA 97, SA 98 × 3 SA 99, SA 101 SA 102, SA 104	<i>I</i>	0.042 ± 0.013	23.619 ± 0.011
		<i>V</i>	0.139 ± 0.005	...	0.0017 ± 0.0005	24.124 ± 0.009
		<i>B</i>	0.249 ± 0.007	0.017 ± 0.004	0.0019 ± 0.0005	24.054 ± 0.007
		<i>U</i>	0.444 ± 0.015	0.027 ± 0.005	...	22.388 ± 0.013
		H α	0.081 ± 0.005	20.412 ± 0.042

3. Membership Selection

Membership selection in the study of open clusters is a critical factor in deriving reliable physical properties of the clusters because, as most open clusters are in the Galactic plane, we can expect there to be many field interlopers in the foreground as well as in the background. We present the color-magnitude diagrams (CMDs) of IC 1805 from CFH12K observations in Figure 9. However, only a weak enhancement of stars between the two dashed lines can be seen in the upper panels of Figure 9. The locus of PMS stars in the CMDs of young open clusters gives several important parameters, such as age, mass distribution, star-formation history, etc. Therefore, low-mass membership selection is the important first step to precisely determine the locus of PMS stars in Figure 9. The locus of PMS members is modified and updated based on the new membership selection criteria described below. The color-excess ratio in *R* and *I* is somewhat uncertain. The parameterization representation of the interstellar reddening law (Cardelli et al. 1989) predicts $E(R - I) = 0.833E(B - V)$ and $E(V - I) = 1.592E(B - V)$ for the R_V obtained in Section 4.2, which is not a good fit to the MS band in Figure 9. In addition, the value of 1.592 is very different from the canonical value 1.25 obtained by Dean et al. (1978). Alternatively, we determined these values from Figure 22, which give the best fit to the blue MS stars in IC 1805 - $E(R - I)/E(B - V) = 0.66$ and $E(V - I)/E(B - V) = 1.26$.

The membership selection of low-mass members at the PMS stage is very difficult because most of them are brighter than normal MS stars. Because classical photometric colors cannot give a reliable membership selection criterion for low-mass PMS stars in young open clusters, various useful membership selection criteria have been introduced during the last 20 years,

such as H α photometry (Sung et al. 1997), X-ray emission (Flaccomio et al. 1999; Sung et al. 2004), and MIR excess emission (Gutermuth et al. 2008; Koenig et al. 2008; Sung et al. 2009). These membership selection criteria have their own limitations. For a thorough selection of members, several criteria should be used in conjunction. In this section, we describe several membership selection criteria, their merits, and their limitations. The selection criteria for H α emission stars is described in Section 3.1, MIR excess emission stars in Section 3.2, and X-ray emission members in Section 3.3.

3.1. H α Emission Stars

3.1.1. H α Emission Stars from CFH12K Observation

Sung et al. (1997) used the H α emission measure index, ($R - H\alpha$), as a membership criterion for low-mass PMS stars in NGC 2264. We present diagrams of ($R - H\alpha$) versus ($V - I$) or ($R - H\alpha$) versus ($R - I$) in Figure 10. The left panels of Figure 10 show the distribution of all stars detected in H α . The division of cluster stars and field stars is not as evident as that in the field of NGC 2264 (see Figure 5 of Sung et al. 2008b). This is due to the fact that the less reddened foreground stars are relatively rare and most field stars (or member stars without any appreciable H α emission) detected are those in the Perseus spiral arm, whose reddening is very similar to that of the cluster stars. There is a vertical scatter at ($V - I$) \approx 2.4 and ($R - I$) \approx 1.2. These objects with large photometric errors are either faint late-type stars in the Perseus arm, halo stars in the FOV, or faint external galaxies. The solid line represents the mean line of stars with no appreciable H α

Table 5
Photometric Data from the Maidanak AZT-22 1.5 m Telescope and SITe 2000×800 CCD^a

ID	α_{J2000}	δ_{J2000}	V	I	$R - I$	$V - I$	$B - V$	$U - B$	ϵ_V	ϵ_I	ϵ_{R-I}	ϵ_{V-I}	ϵ_{B-V}	ϵ_{U-B}	N_{obs}	D^b	M^c	Class ^d	2MASS ID ^e	CFHT ID	VSA ^f	Sp. Type
----	------------------	------------------	-----	-----	---------	---------	---------	---------	--------------	--------------	------------------	------------------	------------------	------------------	------------------	-------	-------	--------------------	-----------------------	---------	------------------	----------

Note.

^a Units of right ascension are hours, minutes, and seconds of time, and units of declination are degrees, arcminutes, and arcseconds.

(This table is available in its entirety in machine-readable form.)

Table 6
Photometric Data from the Maidanak AZT-22 1.5 m Telescope and Fairchild 486 CCD (SNUCam)^a

ID	α_{J2000}	δ_{J2000}	V	I	$V - I$	$B - V$	$U - B$	H α	ϵ_V	ϵ_I	ϵ_{V-I}	ϵ_{B-V}	ϵ_{U-B}	$\epsilon_{H\alpha}$	N_{obs}	D ^b	M ^c	Class ^d	2MASS ID ^e	CFHT ID	VSA ^f	Sp. Type
----	------------------	------------------	-----	-----	---------	---------	---------	------------	--------------	--------------	------------------	------------------	------------------	----------------------	------------------	----------------	----------------	--------------------	-----------------------	---------	------------------	----------

Note.

^a Units of right ascension are hours, minutes, and seconds of time, and units of declination are degrees, arcminutes, and arcseconds.

(This table is available in its entirety in machine-readable form.)

Table 7
Comparison with Photoelectric and CCD Photometry

Catalog	Author	ΔV	$n(n_{\text{ex}})^{\text{a}}$	$\Delta(V - I)$	$n(n_{\text{ex}})^{\text{a}}$	$\Delta(B - V)$	$n(n_{\text{ex}})^{\text{a}}$	$\Delta(U - B)$	$n(n_{\text{ex}})^{\text{a}}$	Range
CFH12K	Hoag et al. (1961)	$+0.082 \pm 0.011$	8 (1)	$V \leq 14$
	Ishida (1969)	$+0.054 \pm 0.034$	9 (1)	$V < 14$
	Kwon & Lee (1983)	$+0.086 \pm 0.042$	17 (5)	$V \leq 14$
	Joshi & Sagar (1983)	$+0.044 \pm 0.027$	63 (20)	$V \leq 14$
	Massey et al. (1995)	$+0.016 \pm 0.058$	429 (35)	$V \leq 15.5$
	Sung & Lee (1995)	$+0.068 \pm 0.052$	50 (2)	$+0.014 \pm 0.051$	32 (1)	$V \leq 14$
	Ninov et al. (1995)	$+0.057 \pm 0.038$	14 (1)	-0.195 ± 0.053	8 (0)	$V \leq 14$
Maidanak 2k	Hoag et al. (1961)	$+0.079 \pm 0.035$	19 (1)	$+0.010 \pm 0.048$	20 (0)	-0.018 ± 0.031	16 (3)	$V < 14$
	Ishida (1969)	$+0.066 \pm 0.028$	24 (5)	$+0.021 \pm 0.019$	21 (8)	$+0.002 \pm 0.049$	23 (5)	$V < 14$
	Kwon & Lee (1983)	$+0.090 \pm 0.049$	33 (4)	$+0.031 \pm 0.034$	32 (5)	$+0.002 \pm 0.056$	32 (5)	$V < 14$
	Joshi & Sagar (1983)	$+0.056 \pm 0.032$	57 (9)	$+0.013 \pm 0.028$	52 (14)	$+0.016 \pm 0.033$	53 (11)	$V < 14$
	Guetter & Vrba (1989)	$+0.053 \pm 0.033$	4 (0)	-0.013 ± 0.014	14 (0)	$+0.031 \pm 0.039$	4 (0)	-0.015 ± 0.009	4 (0)	$V < 12$
	Sung & Lee (1995)	$+0.066 \pm 0.037$	62 (3)	-0.002 ± 0.022	57 (5)	$+0.008 \pm 0.027$	61 (3)	-0.020 ± 0.041	54 (10)	$V \leq 14$
	Massey et al. (1995)	$+0.032 \pm 0.045$	176 (16)	$+0.006 \pm 0.047$	177 (16)	$+0.027 \pm 0.080$	162 (31)	$V \leq 15.5$
SNUCam	Ninov et al. (1995)	$+0.067 \pm 0.033$	25 (1)	-0.205 ± 0.030	24 (0)	$+0.019 \pm 0.048$	25 (1)	$V \leq 14$
	Johnson & Hiltner ^b	$+0.014 \pm 0.009$	3 (0)	$+0.015 \pm 0.009$	3 (0)	$+0.005 \pm 0.052$	3 (0)	$V < 14$
	Hoag et al. (1961)	$+0.043 \pm 0.022$	19 (3)	$+0.014 \pm 0.042$	21 (1)	-0.018 ± 0.055	19 (1)	$V < 14$
	Ishida (1969)	$+0.034 \pm 0.030$	19 (2)	$+0.017 \pm 0.015$	16 (5)	-0.010 ± 0.029	17 (4)	$V < 14$
	Kwon & Lee (1983)	$+0.049 \pm 0.049$	30 (3)	$+0.033 \pm 0.029$	32 (1)	-0.005 ± 0.056	27 (6)	$V < 14$
	Joshi & Sagar (1983)	$+0.014 \pm 0.031$	52 (8)	$+0.015 \pm 0.026$	49 (11)	$+0.032 \pm 0.036$	47 (12)	$V < 14$
	Guetter & Vrba (1989)	$+0.040 \pm 0.032$	3 (0)	-0.027 ± 0.011	13 (2)	$+0.007 \pm 0.008$	3 (0)	-0.022 ± 0.081	3 (0)	$V < 14$
Sung & Lee (1995)	$+0.029 \pm 0.045$	79 (0)	-0.019 ± 0.022	59 (13)	$+0.011 \pm 0.032$	76 (3)	$+0.013 \pm 0.062$	66 (11)	$V < 14$	
Massey et al. (1995)	-0.006 ± 0.046	184 (17)	$+0.014 \pm 0.051$	183 (18)	$+0.031 \pm 0.090$	177 (24)	$V < 15.5$	
Ninov et al. (1995)	$+0.020 \pm 0.032$	25 (1)	-0.228 ± 0.030	24 (0)	$+0.002 \pm 0.023$	21 (5)	$V < 14$	

Notes.

^a The number of stars excluded in the comparison is indicated in parenthesis.

^b Photoelectric data from Johnson & Morgan (1955), Johnson & Hiltner (1956), Hiltner & Johnson (1956), Hiltner (1956).

emission, such as foreground MS stars or weak-line cluster T Tauri stars.

We used the same selection criteria for $H\alpha$ emission stars as in Sung et al. (2008b), i.e., $\Delta(R - H\alpha) > 0.2$ as $H\alpha$ emission stars (membership class: H) and $\Delta(R - H\alpha) > 0.1$ as $H\alpha$ emission candidates (membership class: h) if their combined photometric error in $(R - H\alpha)$ was less than 0.07 mag. Because the depth of the $H\alpha$ images for the North and South regions was not the same as that for the Center, we used different faint limits for selecting $H\alpha$ emission stars— $H\alpha = 24$ mag for the Center ($\Delta\delta = -14'.5 - +13'.5$), 22 mag for the North ($\Delta\delta \geq +13.5$), and 23.2 mag for the South ($\Delta\delta \leq -14.5$). In addition, a more stringent criterion was applied for the faint stars ($R > 20.75$) to avoid many spurious detections due to their large intrinsic errors.

3.1.2. $H\alpha$ Emission Stars from SNUCam Observation

Because the depth of the $H\alpha$ images at the Maidanak Astronomical Observatory was much shallower than those obtained with the CFH12K and the seeing was also relatively poor, the $H\alpha$ emission star selection from the M4k data was limited to the relatively bright stars ($I + H\alpha \leq 18$ mag) to

reduce the number of spurious detections due to large photometric errors in $H\alpha$. The selection criterion of $H\alpha$ emission stars is the same as that in Lim et al. (2014a, 2014b) as shown in Figure 11.

A total of 45 $H\alpha$ emission stars and 16 $H\alpha$ candidates were selected from the SNUCam data. The $H\alpha$ emission indices $\Delta(R - H\alpha)$ and $\Delta H\alpha$ are compared in Figure 11(b). Overall consistency between the two indices was good, but some stars showed a large difference that may be related to the variability of the star. In addition, some stars showed weak emission in one index, but not in the other. Because the time difference between the CFHT observation and the SNUCam observations was 5.5 or 7 years, the level of stellar activity of some stars could have changed.

As most T Tau-type PMS stars show strong variability, especially in $H\alpha$, the $(R - H\alpha)$ index of some stars also showed variability even over a 1 day timescale, therefore the $H\alpha$ membership criteria from one data set was not always the same as that from another data set. In addition, stars with strong variability may have a large combined photometric error. Because we had five sets of independent photometry in $H\alpha$ (three sets from the CFH12K observations and two sets from

Table 8
Catalog of *Spitzer Space Telescope* IRAC and MIPS 24 μm Sources^a

<i>Spitzer</i> ID	α_{J2000}	δ_{J2000}	[3.6]	[4.5]	[5.8]	[8.0]	[24]	$\epsilon_{[3.6]}$	$\epsilon_{[4.5]}$	$\epsilon_{[5.8]}$	$\epsilon_{[8.0]}$	$\epsilon_{[24]}$	N_{obs}	D ^b	Class ^c	M ^b	2MASS ID ^d	Optical Counterpart
-------------------	------------------	------------------	-------	-------	-------	-------	------	--------------------	--------------------	--------------------	--------------------	-------------------	------------------	----------------	--------------------	----------------	-----------------------	---------------------

Note.

^a Units of right ascension are hours, minutes, and seconds of time, and units of declination are degrees, arcminutes, and arcseconds.

(This table is available in its entirety in machine-readable form.)

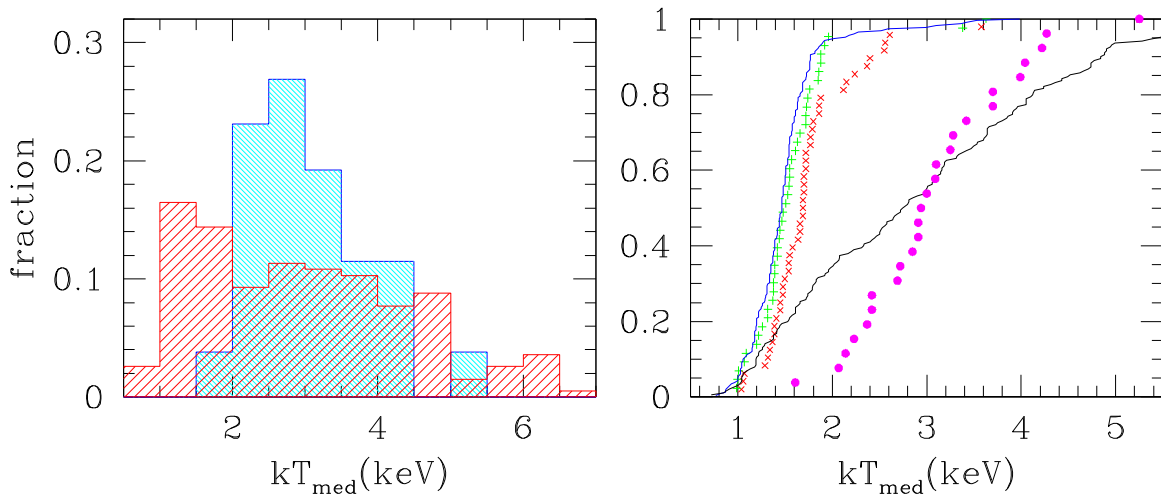


Figure 8. Median X-ray energy distribution of MYStIX sources. (Left) Histogram of no optical counterpart (cyan) and that of no counterpart in optical as well as MIR (red). (Right) Cumulative distribution of disk-bearing YSOs (red cross), Class III (green plus), Class IV (blue solid line), no optical counterpart (magenta dot), and no counterpart in optical and MIR (black solid line).

the SNUCam data), we applied an additional selection criterion to recover the membership of such stars, regardless of their combined photometric error in $(R-H\alpha)$. If a star was classified as an $H\alpha$ emission star (either H or h) more than twice from their $(R-H\alpha)$ index or $H\alpha$ index used in the SNUCam data, we classified the star as an $H\alpha$ emission star. From this procedure, we selected 26 stars as $H\alpha$ emission stars (membership class: H). Among the newly selected “H” stars, 20 stars were originally classified as “h” from the first classification scheme. Similarly, we selected 94 $H\alpha$ emission candidates (membership class: h), where $H\alpha$ emission was detected only once from several $H\alpha$ observations.

From these selection procedures, a total of 182 $H\alpha$ emission stars and 199 $H\alpha$ emission candidates were selected. Among them, SNUCam data contributed wholly for three $H\alpha$ emission stars (VSA 113 = MWC 50 = M4k0795, C41178 = M4k1785, and C66601 = M4k6084) and 21 $H\alpha$ emission candidates, and partly contributed (i.e., detected once) to the selection of 10 $H\alpha$ emission stars. The $H\alpha$ emission stars in Ogura et al. (2002) were cross-matched with our $H\alpha$ emission stars, and we found that four stars in Ogura et al. (2002; BRC 7-4, -7, -8, and -9) were also classified as $H\alpha$ emission stars from our classification scheme, and two (BRC 7-1 and -7) were Class II objects from our MIR data. BRC 7-6 was not classified as an $H\alpha$ emission star nor a Class II object, but is in the PMS locus. The other three stars (BRC 7-2, -3, and -5) are not classified as $H\alpha$ emission stars as well as not being in the PMS locus.

We can find $H\alpha$ emission stars over the whole FOV, and the degree of concentration is rather low. The distribution of $H\alpha$ emission stars is shown in the left panel of Figure 14. The highest density region of $H\alpha$ emission stars coincides with the brightest part of the nebula near HD 15629 (O4.5V—Sota et al. 2011). As mentioned in Section 3.4, the distribution is very similar to that of the intermediate-mass stars of IC 1805.

3.2. MIR Excess Emission Stars

Classification of YSOs is a basic step toward the study of the properties and evolutionary status of YSOs. The same classification scheme described in Sung et al. (2009) was employed, i.e., both the use of two-color diagrams (TCDs) and the slope of the spectral energy distribution (SED;

$\alpha \equiv d \log(\lambda F_\lambda) / d \log \lambda$) with a proper weighting scheme. In addition, for the classification of stars outside the *SST/CM* FOV, we have to use a simple classification criterion, i.e., a star’s location in the $([3.6], [3.6]-[4.5])$ CMD (see Figure 12). In actual application of the above classification criterion, the photometric errors in $[3.6]$ and $[4.5]$ were also taken into account. A total of 11910 objects with reasonable photometric errors were classified. The number of class I ($\alpha \geq +0.3$), Flat ($+0.3 > \alpha \geq -0.3$), class II ($-0.3 > \alpha \geq -1.8$), class III ($-1.8 > \alpha \geq -2.55$), and class IV ($\alpha < -2.55$ —stellar photosphere) objects were 76, 85, 542, 1433, and 9681, respectively. Sung et al. (2009) also introduced α_{IRAC} (SED slope from four IRAC bands) and α_{LW} (SED slope between 8.0 and 24 μm) to classify stars with (pre-)transition disks. If $\alpha_{\text{IRAC}} = -0.3$ – -1.8 and $\alpha_{\text{LW}} > +0.3$, we classified the object as a YSO with a pre-transition disk (“t”), and if $\alpha_{\text{IRAC}} < -1.8$ and $\alpha_{\text{LW}} > +0.3$, then a YSO with a transition disk (“T”). In addition, if the 8.0 μm flux of an object was more than 0.3 dex larger than the flux estimated from the 5.8 μm flux and 24 μm flux, we assigned the object as “P” (an object with polycyclic aromatic hydrocarbon emission). Furthermore, if $[5.8]-[8.0] > 1.5$, we classified the object as “g” (an object with MIR colors similar to those of starburst galaxy). The number of objects with classes P, t, T, and g is 6, 11, 37, and 35, respectively. The distribution of these objects in the TCDs is shown in Figure 13. Although we used the MIR CMDs for the classification of YSOs outside the *SST/CM* FOV, because YSO classification is largely dependent on the SED slope, YSO classification outside the *SST/CM* FOV may be incomplete.

The nature of the spectral classes of objects (classes P and g) is also of interest. There are six objects with a class P. Two objects are stars—S57629 (=C43353) is a normal A-type star, the other (S50327 = C34233) is an $H\alpha$ emission object below the PMS locus. Two objects (S48812 = C32227; S91183) are faint extended sources.¹² Both may be galaxies. Finally, the last two sources are S60140 and S97616. The former is the counterpart of two optical sources C46494 (a star in the PMS locus) and C46539 (a faint extended object below the PMS

¹² S91183 is not measured from the CFH12K images and so is not listed in Table 2, but a faint elongated object can be seen on the CFH12K images. C32227 (=S48812) is a faint object below the PMS locus.

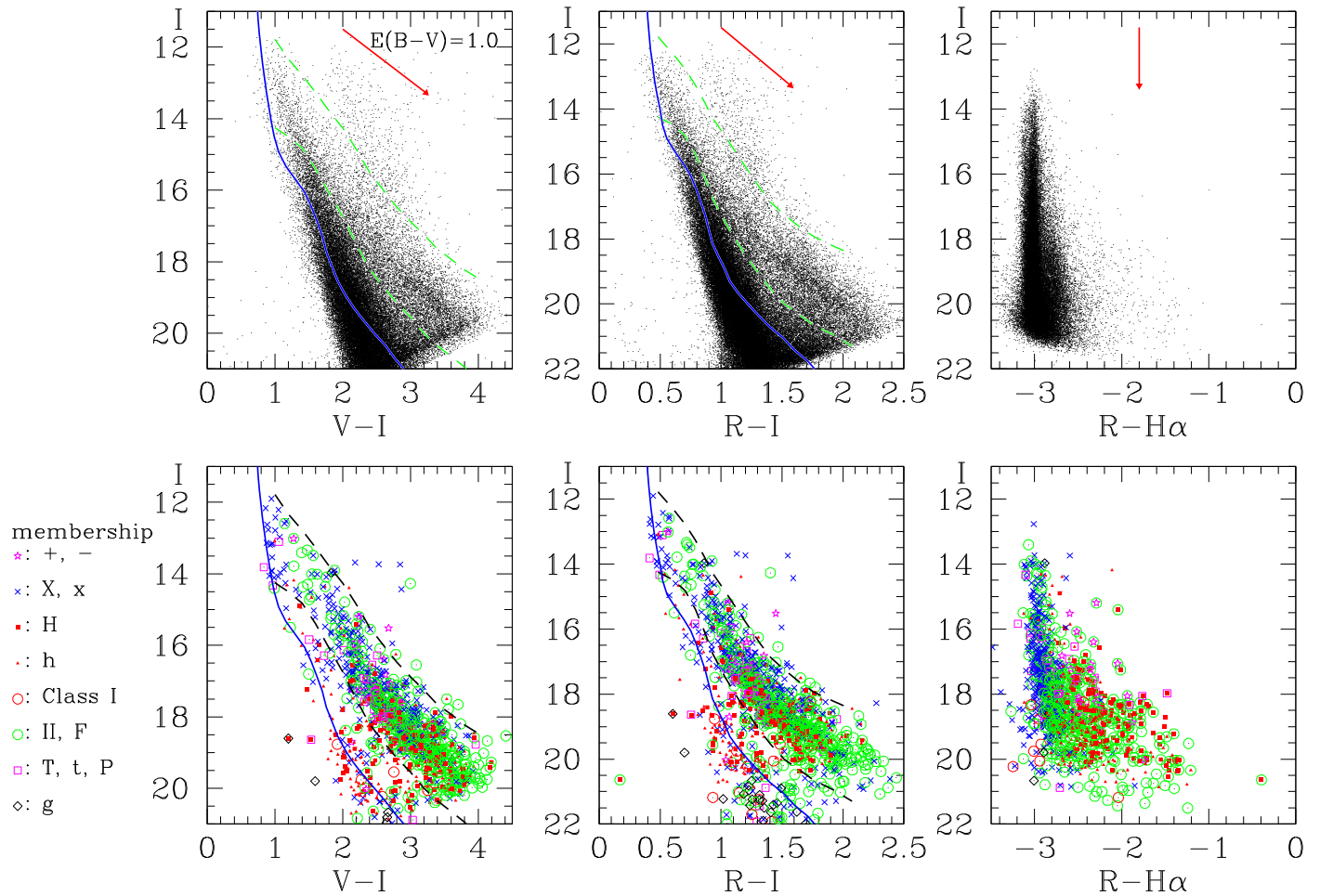


Figure 9. Color–magnitude diagrams of IC 1805 from CFH12K observations. Upper panels: the $(I, V - I)$ (left), $(I, R - I)$ (center), and $(I, R - H\alpha)$ (right) diagrams for all stars. Lower panel: the same diagrams for those stars assigned as members. The blue solid line represents the ZAMS relation (Sung et al. 2013a) at a distance of 2.4 kpc and $E(B - V) = 0.85$ mag, and the two dashed lines in the left two panels are the upper and lower boundaries of the PMS stars in IC 1805. The red arrow in the upper panels is the reddening vector for $E(B - V) = 1.0$ mag. The meaning of the symbols is presented in the lower left.

locus, and hence a background galaxy), while the latter is not in the CFH12K FOV.

There were 35 objects with a class g. Thirty objects are extended objects in the CFH12K images, and hence are galaxies. Two (S47970 = C31194, S57498 = C43188) are stars in the PMS locus. S73461 is the counterpart of two optical sources C63264 (an $H\alpha$ emission object below the PMS locus) and C63272 (a star? in the PMS locus). However, it is very difficult to judge whether S73461 is an elongated galaxy or a close optical double. The remaining two are not in the CFH12K FOV. The total number of optically confirmed galaxies is 122.

Among stars with a YSO classification from MIR photometric diagrams and SED slopes, YSO classes I, II, F, t, T, and stars of YSO class P and g are considered as probable low-mass PMS members of IC 1805. We present the spatial distribution of YSOs in the right panel of Figure 14. The highest density region of YSOs is midway between HD 15558 (O4.5III(f)) and HD 15629. The density of these objects decreases as the distance from the peak increases. The gradient of the surface density is high to the south and southwest, but low to the north. The lowest density of these objects is southwest of the cluster center. In addition, there is a weak signature of density enhancement of these objects in the far southern region. The marginal difference between the two distributions in the north may be caused by the difference in the photometric depth of the

$H\alpha$ observations as well as the incompleteness of YSO classification from MIR photometry.

The surface density distribution of Class III and IV objects is shown in Figure 15. These objects show a weak enhancement near the cluster center. There is no physical reason for Class III or IV objects above or below the PMS locus to show any radial variation of the surface density. However, the surface density of these objects in the PMS locus may show a radial variation, and hence we have drawn their surface density in the lower panels of Figure 15. This fact implies that the disk lifetime of some PMS stars may be very small or the strong ultraviolet (UV) radiation from hot massive stars in the cluster center may affect the disk lifetime (Sung et al. 2009).

3.3. X-Ray Emission Stars

Strong X-ray emission is one of the more prominent properties of PMS stars and therefore can be used as a membership criterion for the PMS stars in young open clusters. However, as X-ray emission from late-type stars persists for a long time (Sung et al. 2008a), and in addition, as the activity level of X-ray emission from PMS stars covers a wide range, i.e., $\log L_X/L_{\text{bol}} = -5 - -3$ (Feigelson et al. 2003), we should expect there to be some foreground or background interlopers with X-ray emission. With the above caveats, we

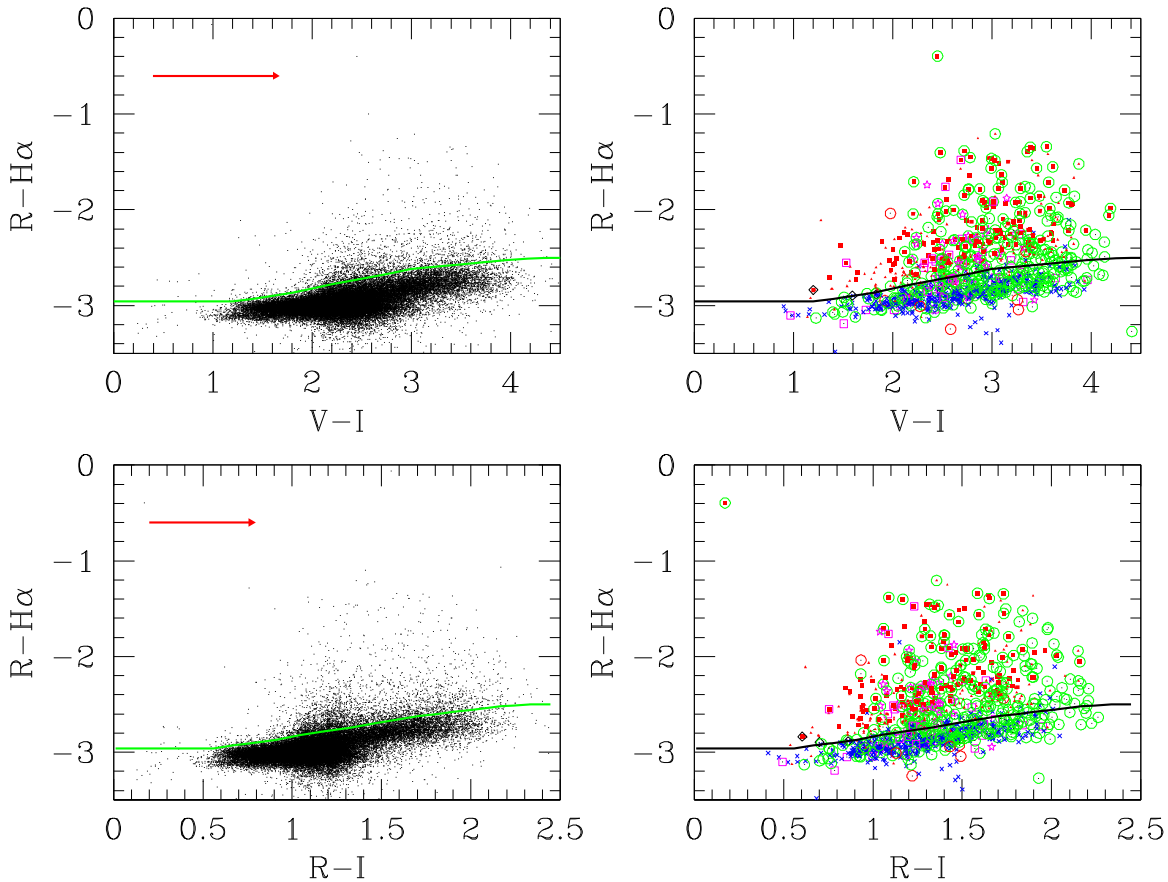


Figure 10. Selection criteria for $H\alpha$ emission stars. Left panels: the $(R - H\alpha)$ vs. $(V - I)$ diagram (upper) or the $(R - H\alpha)$ vs. $(R - I)$ diagram (lower) of all stars. Right panels: the same diagrams for stars with membership. The green (left panels) or black line (right panels) denote the mean line of stars with no appreciable $H\alpha$ emission. The red arrow in the left panels represent the reddening vector of $E(B - V) = 1.0$ mag. The other symbols in the right panels are the same as those in Figure 9.

tentatively identify the optical counterparts of the X-ray emission sources as cluster members, and then check their distribution in the optical CMDs. From the overall distribution of $H\alpha$ emission stars, MIR excess emission stars, and X-ray emission stars, the locus of PMS stars in the CMDs is finally derived as was done for the young open cluster NGC 2264 (Sung et al. 2004). The optical counterparts of X-ray sources in the PMS locus are considered to be members of IC 1805.

The lower panels of Figure 9 show the optical CMDs of the stars with PMS membership (stars with $H\alpha$ emission, X-ray emission, and/or PMS stars with YSO class I, F, II, t, T, P, and g). Most of these stars with PMS membership are located between the two dashed lines, and therefore the two dashed lines represent the PMS locus of IC 1805. However, some stars with PMS membership are on, or near, the reddened ZAMS line. Some of them were selected as PMS members both from $H\alpha$ photometry and MIR photometry. These stars are most likely PMS stars with nearly edge-on disks. Other stars selected from only one membership criterion ($H\alpha$ photometry or MIR photometry) may not be real PMS members, but spurious detections due to their intrinsic large photometric errors. Some X-ray emission stars near the reddened ZAMS line are either X-ray active stars among field stars in the Perseus spiral arm, or background galaxies. In addition, a few X-ray emission stars above the upper limit of the PMS locus, are foreground active late-type stars in the local arm. There is a YSO class F (C01044 = S022094) that is far brighter than the other PMS members in the PMS locus. This object is the optical

counterpart of IRAS 02260+6118, and could be one of the youngest objects near the border between W3 and W4 (see also Panwar et al. 2014).

3.4. Massive and Intermediate-mass Members

O- and early B-type ($Sp \lesssim B5$) stars are generally found in young stellar systems. Such massive members of young clusters or OB associations can be easily selected from the $(U - B, B - V)$ TCD. The number of O- and early B-type stars in the CFH12K FOV is 8 and 71, respectively. These stars are all considered to be massive members of IC 1805. However, optical photometry alone cannot discriminate members of IC 1805 from those of the Cas OB6 association.

Selection of late B- to F-type members of young open clusters is very difficult. The disks around these stars are relatively short-lived (Sung et al. 2009), therefore $H\alpha$ or MIR photometry is useless except for Herbig Ae/Be stars. In addition, late B- to F-type stars are quiet in X-rays because they have no surface convective zone, nor any strong stellar wind. Only a fraction of them are detected from X-ray observations, and in these rare cases, the X-ray emission is considered to originate from a low-mass companion that is in the T Tauri stage (Damiani et al. 2016). Spectral classification may be the only reliable membership criterion for these stars in young open clusters. Unfortunately, the spectral types of only a limited number of stars in IC 1805 are known. In view of such limitations, we had to select most of the intermediate-mass

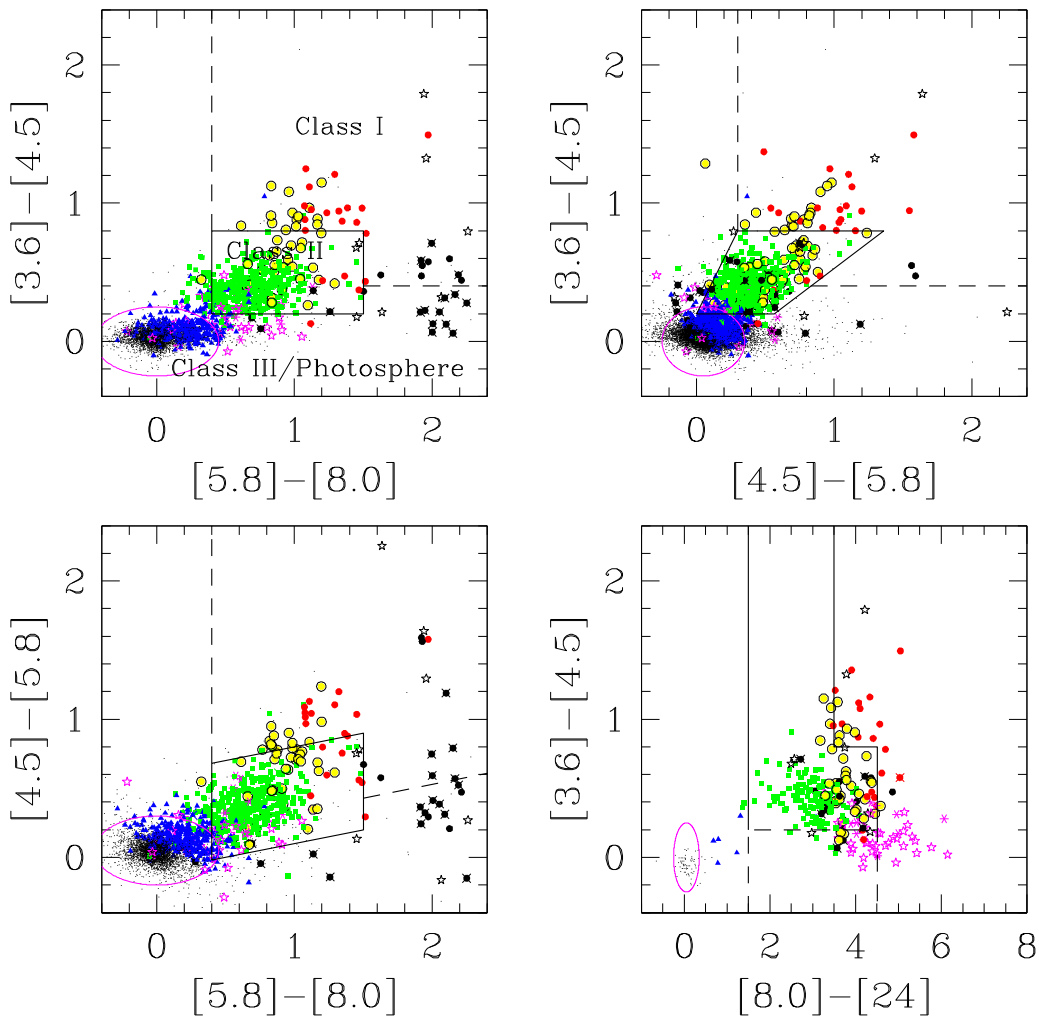


Figure 13. Two-color diagrams. Symbols are the same as those in Figure 12.

The spatial distribution of massive members and intermediate-mass members selected in this section is shown in Figure 17. Most massive members are concentrated at the center. Several members are between the bright central nebula and the faint north–south nebula along the western edge of W4. Furthermore, a few are at the edge of BRC 5. These stars are considered to be the second generation stars triggered by the strong radiation field from the massive O-type stars in the IC 1805 center (Ogura et al. 2002; Panwar et al. 2014). However, the distribution of intermediate-mass stars is more distributed and extended to the northeast connecting the central cluster and BRC 5. However, we could not find any enhancement of intermediate-mass stars in the southwest. The distribution is very similar to that of $H\alpha$ emission stars in Figure 14.

4. Reddening and Distance

4.1. Two-color Diagrams and Reddening

The TCDs of stars in the observed region are shown in Figure 18. Because the reddening vector in the $(R - I, V - I)$ TCD is very similar to the intrinsic color–color relation of MS stars, the field stars in the foreground or in the Perseus spiral arm and cluster stars show a similar distribution in the diagram, and so the diagram cannot be used for any membership criterion. The situation is slightly improved in the

$(B - V, V - I)$ TCD, but the loci of cluster PMS stars and that of field MS or giant stars largely overlap each other.

However, the $(U - B, B - V)$ diagram is the basic diagram for estimating the reddening of early-type stars without ambiguity, at least for the stars earlier than B5. The reddening $E(B - V)$ of 87 early-type stars in IC 1805 and 4 early-type stars outside the CFH12K FOV is determined from the $(U - B, B - V)$ diagram. The range of $E(B - V)$ is between 0.72 and 1.23 mag, and the mean value of $E(B - V)$ is 0.88 (± 0.10) mag (median value is 0.85 mag), which are very similar to that obtained by Guetter & Vrba (1989) and Massey et al. (1995). Although Sung & Lee (1995) applied a slightly different reddening law, they obtained a similar range and mean value. However, Joshi & Sagar (1983) and Hillwig et al. (2006) derived a somewhat smaller range and mean value. The latter authors derived the reddening from SED fitting to the O-type stars in the Cas OB6 association. Their $E(B - V)$ is mostly consistent with ours except for the O7Vz star BD +60 513 and the most evolved massive star HD 15570. While the $E(B - V)$ for the former is smaller than ours, that of the latter is larger.

The spatial variation of reddening, i.e., the reddening map, is derived from the 91 early-type stars in and around the observed FOV, and is shown in Figure 19(a), which is superimposed on the color-composite MIR image. The reddening is in general

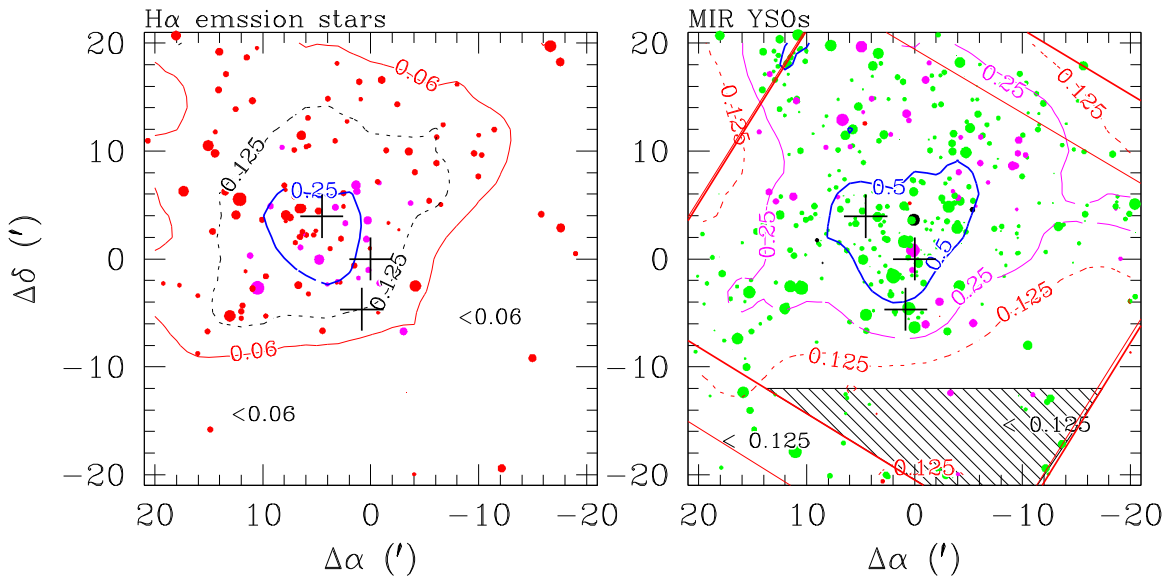


Figure 14. Spatial distribution of H α emission stars (left) and YSOs with YSO class I, F, II, t, T, g (right). The positions of HD 15558 ($\Delta\alpha = 0'0$, $\Delta\delta = 0'0$), HD 15570 ($\Delta\alpha = 0'82$, $\Delta\delta = -4'66$), and HD 15629 ($\Delta\alpha = 4'54$, $\Delta\delta = 3'94$) are marked as “+.” The contour with numbers represents the surface density of H α emission stars and YSOs in units of (star arcmin $^{-2}$). Thick and thin large squares in the right panel represent the FOV of IRAC 3.6 μ m and 4.5 μ m, respectively. The shaded area in the right panel represents the control field selected for the correction of field star contribution to the initial mass function (see Section 5.2). Dots represent either H α emission stars (left) or YSOs (right) for which size is proportional to the brightness of the objects. The color of the dots indicates the type of membership—(left) red: H α emission stars, magenta: H α emission stars with X-ray emission; (right) red: Class I, green: Class II or flat spectrum (F) objects, magenta: objects with (pre-)transition disks (t or T) or with PAH emission (P), and black: galaxy candidates (g).

larger in the west (close to the active SFR W3), which implies that the PAH emission nebula in the west is in front of IC 1805. However, there seems to be no close correlation between the variation in the reddening and the emission nebula at the center. This fact implies that the bright emission nebula is illuminated by the strong UV radiation from hot massive stars at the cluster center, but is probably at the immediate background of the main cluster. The reddening in the southeast of IC 1805 is slightly larger, implying that the nebula is partly associated with the cluster stars in this region. The smallest reddening occurs at ($\Delta\alpha \approx 6'$, $\Delta\delta \approx 10'$), where the PAH and CO emission (Carpenter et al. 2000) is relatively absent. Figure 19(b) shows the surface density of field MS stars below the PMS locus with $I = 17$ –20.5 mag. The surface density map also supports the radial structure of this region—the field stars are densely populated in the region where PAH emission is absent. The density is lowest in the western region. These facts also support the clouds associated with W3 being in front of IC 1805. The PAH emitting nebula just behind the central cluster effectively blocks the light from the background, therefore the surface density of field stars is relatively low along the nebula that extends from northwest to southeast. If the surface density of field stars along the line of sight is homogeneous in the observed FOV, about two-thirds of them are in front of the Perseus arm, about 15% are between the PAH nebula in the west (probably at the same distance as W3) and IC 1805, and about 25% are in the background of IC 1805. The reddening map will be used to estimate the reddening of the low-mass PMS stars in IC 1805.

Although the ($U - B$) values of the faint stars were not very good because of the smaller aperture of the telescope used, there are non-negligible numbers of UV-bright stars in the ($U - B$, $B - V$) diagram. This implies that many low-mass PMS stars in IC 1805 are still actively accreting. A similar situation can be found in other young open clusters in the Perseus spiral arm (Lim et al. 2014a, 2014b).

4.2. Reddening Law

The interstellar reddening law is one of the fundamental parameters involved in determining the distance to astronomical objects, and is known to be different from one line of sight to another in the Galaxy (Fitzpatrick & Massa 2009; Sung & Bessell 2014). In addition, Fitzpatrick & Massa (2009) acknowledged that there is no universal NIR extinction law. Forte (1978) and Guetter & Vrba (1989) presented a method to determine the total-to-selective extinction ratio R_V using color-excess ratios of optical and NIR colors, and Sung et al. (2013b) extended this relation to the MIR *Spitzer* colors. These relations have been successfully used to determine the R_V of several young open clusters. The color-excess ratios of several young open clusters have been well fitted to a single line with a normal R_V (Kook et al. 2010; Lim et al. 2011; Sung et al. 2013b; Lim et al. 2014a, 2014b, 2015a, 2015b). However, the color-excess ratios of some extremely young open clusters are best fitted by a combination of two lines with different slopes, which means that two different media with different extinction properties exist in the line of sight, i.e., an abnormal reddening law for the intracluster medium with a normal R_V for the foreground medium (e.g., NGC 1931 (Lim et al. 2015a), Westerlund 2 (Hur et al. 2015), or Tr 14 and Tr 16 (Hur et al. 2012)).

Figure 20 shows the color-excess diagrams for IC 1805 that we used to determine the total-to-selective extinction ratio R_V . We excluded the H α emission star VSA 113 (O9.5Ve or Be) from the fits because its colors were affected by emission from its circumstellar disk. The color-excess ratios are all well fitted to a single line, which implies that (1) the dust size distribution of the foreground medium and intracluster medium are very similar and (2) a fairly normal R_V in the direction of IC 1805 is obtained from the 64 O and early B-type stars ($Sp \leq B4V$), $R_V = 3.052 \pm 0.058$. From optical and NIR photometry and polarimetry, Guetter & Vrba (1989)

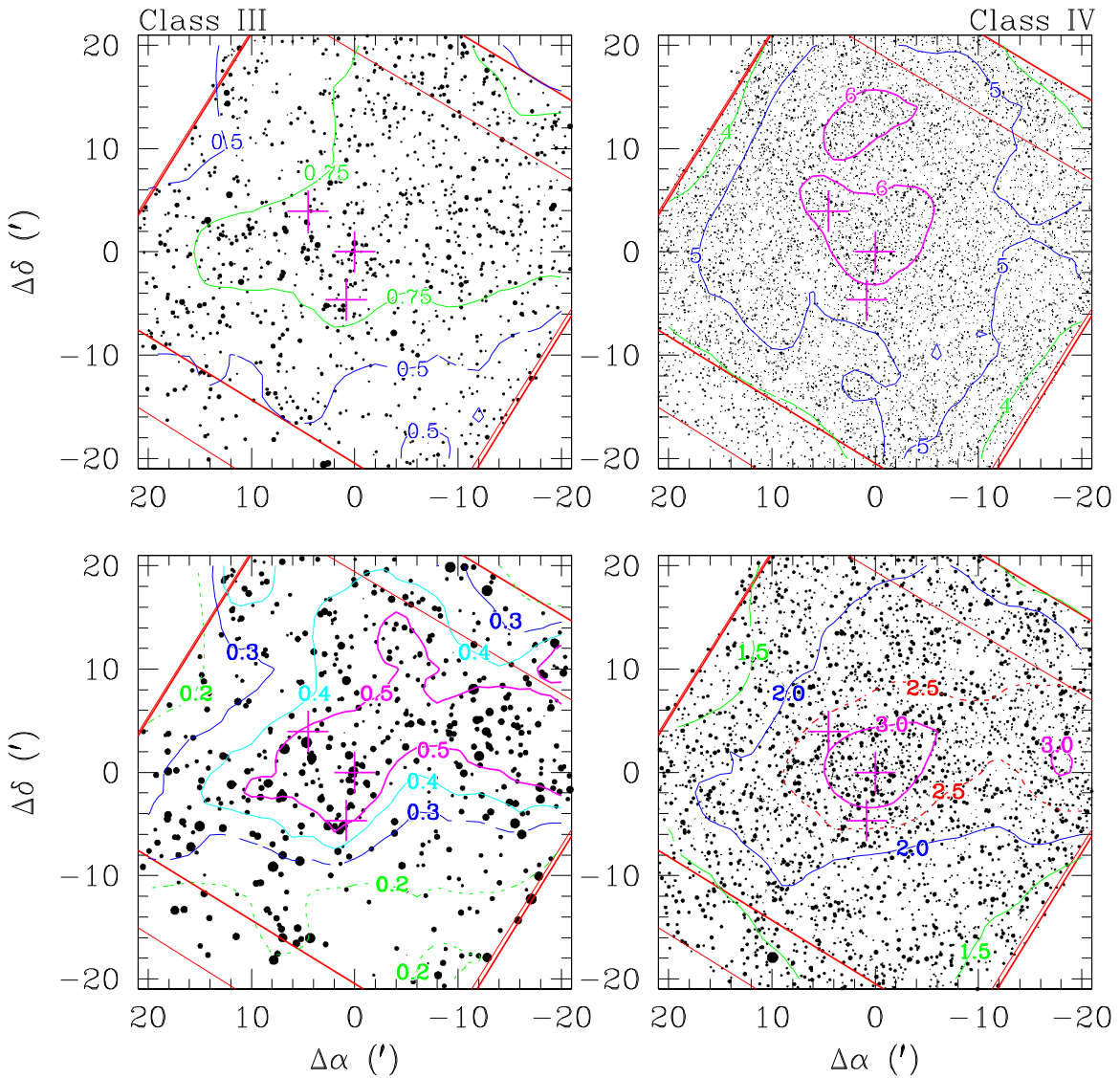


Figure 15. Spatial distribution of stars with YSO Class III and IV. (Upper) all stars with YSO class III (left) and IV (right). (Lower) the stars with the given YSO class in the PMS locus. The numbers on the contour denote the surface density in units of (star arcmin^{-2}).

arrived at the same conclusion for the properties of the dust in IC 1805 and in the foreground ($R_V = 3.1 \pm 0.1$). Recently, Medhi et al. (2007) deduced at the same dust properties from CCD polarimetry of IC 1805. Hanson & Clayton (1993) also had arrived at the same conclusion from extinction curve fitting from NIR to UV wavelengths, but obtained a slightly smaller R_V of about 2.9.

Previous R_V determinations for the cluster fall into two groups. One group obtained a nearly normal R_V as in the current work. Hillwig et al. (2006) obtained $R_V = 2.94\text{--}3.13$ from SED fitting; Kwon & Lee (1983) obtained $R_V = 3.06 \pm 0.06$ for the central region; Sung & Lee (1995), $R_V = 2.9$ from the spectral type versus M_V (Sp- M_V) relation. While another group of authors obtained somewhat larger values. Johnson (1968), $R_V = 5.7$ for the Cas OB6 region from the Sp- M_V relation; Kwon & Lee (1983), $R_V = 3.82 \pm 0.5$ for the peripheral region; Ishida (1969), $R_V = 3.8 \pm 0.5$ using radio and H α emission measures; Pandey et al. (2003), $R_V = 3.56 \pm 0.29$ from various color-excess diagrams, TCDs, and CMDs.

4.3. The Distance of IC 1805 and CMDs

Because O stars in IC 1805 are used for the calibration of the Sp- M_V relation (Conti & Aschuler 1971), the distance to the cluster is very important. However, because the distance to an astronomical object is strongly dependent on the adopted R_V and the adopted or derived R_V in the direction of IC 1805 varied from 2.9 to 5.7, the derived distance to IC 1805 ranged from 0.76 kpc (Johnson 1968) to 2.4 kpc (Kwon & Lee 1983; Sung & Lee 1995). The distance of IC 1805 from most photometric studies has been based on ZAMS fitting or the Sp- M_V relation, and converges around 2.3–2.4 kpc (Joshi & Sagar 1983; Kwon & Lee 1983; Massey et al. 1995; Sung & Lee 1995). In support, Garmany & Stencel (1992) derived the distance of the surrounding Cas OB6 association to be 2.4 kpc. In the absence of more recent determinations, investigators have therefore assumed or adopted the distance determined by Massey et al. (1995). However, a recent challenge to the distance of IC 1805 has emerged from radio astrometry of H $_2$ O or methanol masers in massive SFRs. Very Long Baseline Interferometry (VLBI) astrometry of a methanol maser

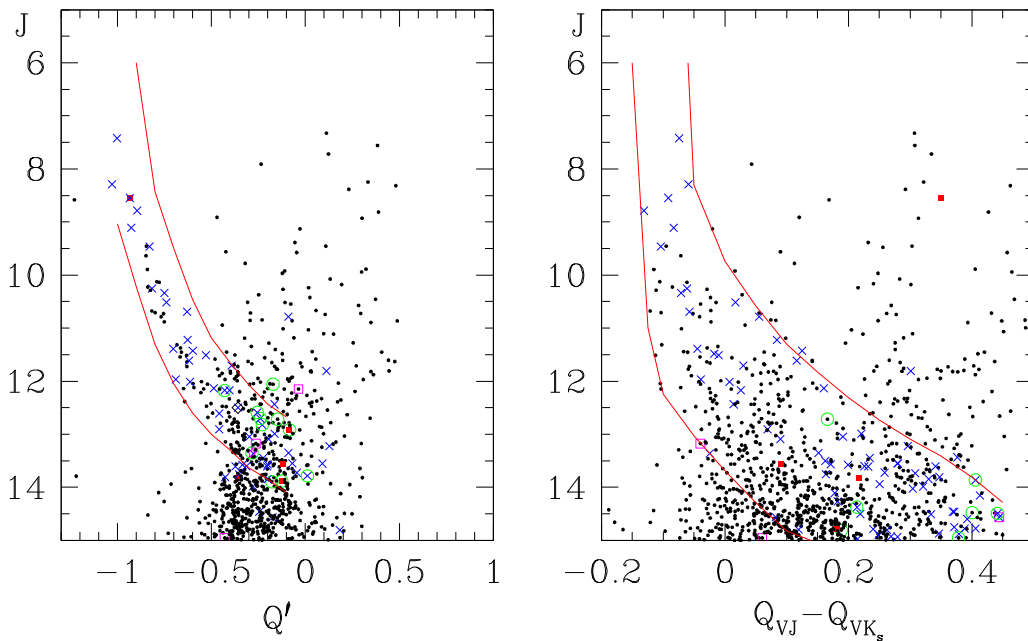


Figure 16. (J , Q') diagram (left) and (J , $Q_{VJ} - Q_{VK_s}$) diagram (right) of stars in the Maidanak 2k data. The modified Johnson's Q [$Q' \equiv (U - B) - 0.72(B - V) - 0.025E(B - V)^2$] and the reddening-free indices $Q_{V\lambda}$ are defined in Sung et al. (2013a). The solid lines represent the upper and lower limits of massive members and candidate intermediate-mass members of IC 1805. The other symbols are the same as those in Figure 9.

(Xu et al. 2006) or H_2O maser (Hachisuka et al. 2006) in the nearby H II region W3 has given a consistent distance of 2.0 ± 0.05 kpc for W3(OH). These astrometric results will be discussed further in Section 6.1.

We have independently derived the distance to IC 1805 using a modified ZAMS fitting technique. The CMDs of the reddening-free index $Q_{V\lambda}$ and a modified Johnson Q (Q') were used as shown in Figure 21. The definition of these indices is presented in Sung et al. (2013a; repeated in Lim et al. 2015a). When we fit to the ZAMS, we should take the lower ridge line of the MS band to avoid the effects of evolution during the MS stage, contamination by systems of multiple stars or chemically peculiar stars, and/or scatter due to photometric errors. Our derived distance modulus of IC 1805 is $11.9 (\pm 0.2)$ mag (equivalently $d = 2.4 (\pm 0.2)$ kpc), which is consistent with previous determinations, but about 400 pc more distant than the nearby SFR W3(OH). The error quoted here is an assumed error.¹³ In addition, ZAMS fitting is affected by the photometric errors. However, as can be seen in Figure 21 the ZAMS describes the lower part of the cluster stars in all four reddening-free CMDs.

The CMDs of IC 1805 are presented in Figures 9 and 22. The ZAMS with the median reddening and the adopted distance of IC 1805 is over-plotted. From the CMDs in Figure 9, we can barely detect the existence of cluster stars, but in Figure 22 we can easily recognize the well-developed sequence of early-type members to the left of each CMD. The reddened ZAMS follows the early-type MS stars in each CMD. The locus of low-mass PMS stars in IC 1805 is marked in two CMDs whose color is less affected by the UV excess due to mass accretion activities. In the (V , $U - B$) CMD, early-type

members are clearly separated from field stars, which are distributed vertically at $(U - B) \approx 0.3\text{--}0.6$ mag. However, the separation between cluster stars and field stars is not conspicuous in most CMDs in Figure 22. As mentioned in Section 3.4, late B- and A-type stars in IC 1805 (masses of PMS stars between $3 M_{\odot}$ and $5 M_{\odot}$ stars in Figure 22) overlap with field stars in the CMD, and cannot be reliably separated from field stars with any combination of optical and/or IR colors. The (I , $H\alpha$) CMD, which could be used as an age indicator of young open clusters as claimed by Damiani et al. (2016), is also presented. Due to the small number of X-ray emitting B- and A-type stars, the hooked feature at $H\alpha \approx 0.2$ is less pronounced. However, the length of the hooked feature is shorter than that of NGC 6231 and the feature is well separated from the vertical distribution of low-mass PMS stars at $H\alpha \approx 0.0$. These features indicate that IC 1805 is younger than NGC 6231 (age = 4.0–7.0 Myr for massive stars). All eight O-type stars in IC 1805 are X-ray emitters, but the fraction of X-ray emitters is about half for early B-type stars ($Sp \leq B4$).

4.4. Radius of IC 1805

The radius of a cluster is one of the important parameters in the study of cluster systems. However, IC 1805 is a very sparse cluster with no strong central concentration, and so it is not easy to define the radius of the cluster. Although, as shown in Figures 14, 15, and 17, massive stars are concentrated at the center, the spatial distributions of $H\alpha$ emission, MIR excess stars, and intermediate-mass stars are extended toward the northeast direction and show an abrupt decrease to the southwest. Therefore, the radius or spatial extent of IC 1805 is not well represented by the radial distribution of one type of star. Despite such a limitation, we tried to determine the radius of IC 1805 from the radial distribution of member stars. Before calculating the radial density profile of one type of object, we should find the center of the cluster. The apparent center of IC

¹³ We have selected proper motion and parallactic members of 34 nearby open clusters using the *Gaia* DR1 Tycho-*Gaia* astrometric solution (TGAS) data to check the reliability of the ZAMS relation, and found that the error in distance modulus is 0.21 ± 0.10 mag due to the scatter of individual parallaxes among members.

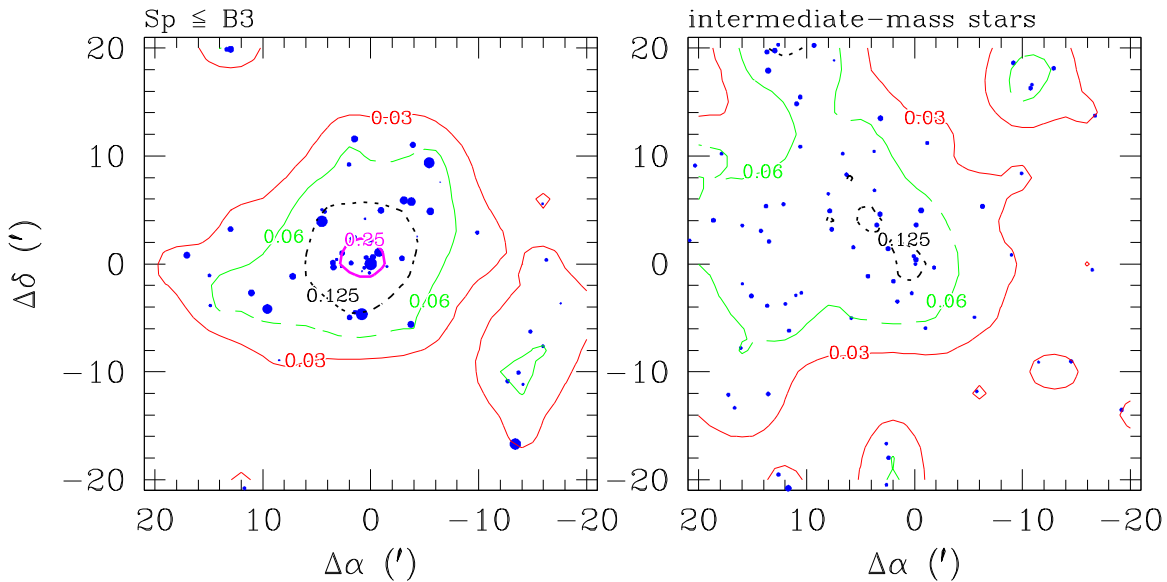


Figure 17. Spatial distribution of massive members (left) and intermediate-mass members (right). Blue dots represent the selected members of IC 1805. The size of dots is proportional to the brightness of the star, and the number on the contour denotes the surface density in units of (star arcmin²).

1805 derived from the surface density distribution of massive stars in Figure 17 is around the brightest star HD 15558 (O4.5IIIe), however, the spatial distribution of H α emission stars or MIR YSOs in Figure 14 indicates the center of these objects is to the immediate north of HD 15558 or somewhere between HD 15558 and HD 15629 (O4.5V). As we did for the young open cluster NGC 6231 (Sung et al. 2013b), we calculated the mass-weighted mean value of $(\Delta\alpha, \Delta\delta)$ of stars with $m \geq 5M_{\odot}$. The resultant center is $(-0.057, +0.867)$ north of HD 15558 ($\alpha_{J2000} = 2^{\text{h}} 32^{\text{m}} 42^{\text{s}}.06$, $\delta_{J2000} = +61^{\circ} 28' 2''.8$).

To determine the radius of IC 1805, we calculated the surface density profiles of the massive stars ($m \geq 5M_{\odot}$), Class IV, Class III, and MIR excess PMS stars, and these profiles are shown in Figure 23. The profile for massive stars was calculated for the whole CFH12K FOV, but profiles for the others were calculated for the SST/CM FOV because of the completeness of membership selection. In order to estimate the radial extension of IC 1805, we fitted the profile to the EFF model ($\mu(r) = \mu_0[1 + (r/a)^2]^{-\gamma/2} + \mu_{\text{bg}}$, Elson et al. 1987), and have given the fitting results in each panel of Figure 23 and Table 9. The fitting was performed with the IDL routine MPFIT. The fitting results relatively well represent the observed radial profile of massive stars and Class IV stars, however, those for Class III stars or MIR YSOs have a large error due to an abrupt increase at the very center of IC 1805 ($r \lesssim 1'$). We also tried to fit the profiles with the King model ($\rho(r) = \rho_0/[1 + (r/r_c)^2] + \rho_{\text{bg}}$, King 1962), and presented the results in Table 9. In contrast to the EFF model, the King model does not well describe the profile, especially near the center. The surface density of MIR YSOs and the ratio between MIR YSOs and Class IV stars decrease abruptly at $r \approx 15'$. The surface density profiles as well as the fitting results to the EFF model show that the radius of IC 1805 is about $15'$ ($=10.5$ pc at $d = 2.4$ kpc). This value is about 1.7 times larger than the radius obtained by Panwar et al. (2017) who estimated the radius from the radial density profile of their selected YSO members.

The surface density of massive stars is high enough to derive some information on their radial distribution. The core radius

r_c , which is defined as the radius where the surface density reaches half of the central value, is about $1.07'$ (equivalently 0.75 pc). This value is very similar to that of the massive stars in NGC 6231 ($r_c = 0.88 \pm 0.02$ pc). However, the full radius of IC 1805 is about 1.75 times larger than that of NGC 6231 ($r \approx 6.0$ pc).

5. Age and the Initial Mass Function of IC 1805

The mass and age of a star can be derived from the HRD with the help of stellar evolution models and PMS evolution tracks. To construct the HRD of a stellar system, we have to employ various calibrations in order to properly locate the stars in the HRD. The various calibrations required are summarized in Sung et al. (2013a). For massive O-type stars, the adopted spectral type is very important for estimating the effective temperature and bolometric magnitude (Sung et al. 2013a). Although minor differences in spectral type were mentioned in Rauw & Nazé (2016), we adopt the spectral types from Sota et al. (2011). Currently, two stellar evolution models of massive stars with stellar rotation are used in the mass and age estimate of massive stars, and these are compared in Sung et al. (2013b). For consistency with the mass and age scale of massive stars with previous studies of our group (Hur et al. 2012; Sung et al. 2013b; Lim et al. 2014a, 2014b, 2015a; Hur et al. 2015), the age and mass of massive stars are determined using the stellar evolution models of Ekström et al. (2012).

For a long time, the PMS evolution tracks of Siess et al. (2000; hereafter SDF00) were used in the age and mass estimate of low-mass PMS stars. Recently, Baraffe et al. (2015; hereafter BHAC15) published new PMS evolution tracks for masses less than $1.4 M_{\odot}$. We compare the masses and ages of low-mass PMS stars from these two PMS evolution tracks.

5.1. The HRD and Age of IC 1805

We constructed the HRD of IC 1805 using the calibrations described above. The HRD is shown in Figure 24 with several isochrones interpolated from stellar and PMS star evolution

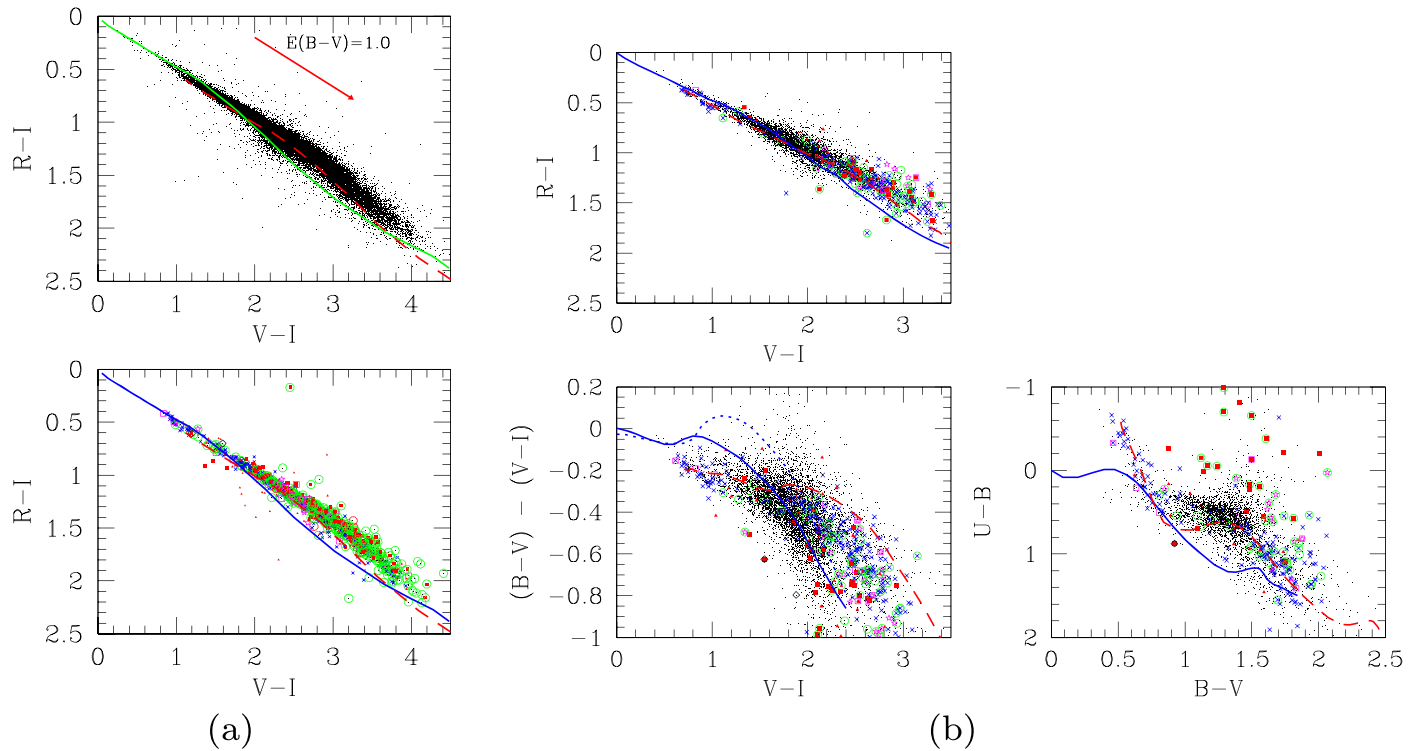


Figure 18. Two-color diagrams. (a) the $(R - I, V - I)$ TCDs from CFH12K observations. The upper and lower panels show the TCD of all stars and that of stars with PMS membership. (b) Three TCDs from Maidaanak 2k and 4k observations. The blue solid and red dashed lines represent, respectively, the intrinsic and reddened color-color relations of MS stars. The median reddening of the early-type members of IC 1805 $E(B - V) = 0.85$ mag is applied in the diagrams. The dotted line in the lower center is the intrinsic color-color relation of giant stars. The other symbols are the same as in Figure 9.

tracks. The brightest stars in the cluster are evolving away from the MS. The most evolved star HD 15570 (O4.5If+) is considered to be at the transition stage between a normal Of star and a WN star (Rauw & Nazé 2016). The optically brightest star HD 15558 (O4.5III(f)) is an SB2 system with a primary that has possibly a very large minimum mass (De Becker et al. 2006; see Rauw & Nazé 2016 for a more recent result). The age of stars at the MS turn-on in the lower part of the HRD seems to be much younger than that of the massive O-type stars, but, as mentioned in the previous sections, their membership is very uncertain. More discussion on the age distribution of low-mass PMS stars will be dealt with in detail below.

One of main issues in studying IC 1805 is the star-formation history and its relation to the star-formation activity in the active SFR W3. Guetter & Vrba (1989) noticed a large scatter of early B-type stars in the reddening-corrected CMD, and interpreted it as an old population of IC 1805 (age: about a few 10 Myr) prior to the formation of most massive stars in the cluster. However, from the size of the H II region, Dennison et al. (1997) estimated the age of the superbubble to be between 6.4 and 9.6 Myr.

From Figure 24, most O-type stars in IC 1805 are well fitted to the isochrone of age 3.5 Myr. There are two evolved early-type stars in the observed FOV—BD +60 493 (B0.5Ia—Ishida 1970; Shi & Hu 1999) and BD +60 498 (O9.7II-III—Sota et al. 2011).¹⁴ These two stars can be thought of as members of

¹⁴ Recently Rauw & Nazé (2016) claimed that the luminosity class of the star is V rather than II–III from the absorption of He II $\lambda 4686$ and the ratio of Si IV $\lambda 4088$ to He I $\lambda 4143$. If the luminosity class of the star is MS, BD +60 498 is probably a member of IC 1805 rather than a member of the Cas OB6 association.

the Cas OB6 association scattered around the W3–W4–W5 region. If we fit these two stars, the age of the best-fit isochrone is 7.3 Myr, which is well matched to the expansion age of the superbubble (Dennison et al. 1997). Although we can see a large scatter of early B-type stars in the HRD as noticed by Guetter & Vrba (1989), and if we assume the scatter to be the result of stellar evolution, we could find at least one or two evolved stars with a luminosity class of Iab. However, we cannot find any evolved counterpart of these early B-type stars in or around the observed FOV.¹⁵ If their scatter is a result of the star-formation history in IC 1805, their spatial distribution or kinematic properties may preserve some information of that. However, we could not find any differences between the two groups (see Section 6.2 for details).

Low-mass PMS stars in young open clusters give valuable information on the star-formation history of the clusters because the mass and age of PMS stars can be determined from the PMS evolution tracks. The HRD of low-mass PMS members is shown in Figure 25. In the figure, we compared two PMS evolution models—SDF00 in the upper left panel and BHAC15 in the other panels. Most PMS stars in IC 1805 are well enclosed between the two isochrones with ages 1 Myr and 5 Myr for SDF00. However, many of them are brighter than the 1 Myr-isochrone of BHAC15, but their distribution well follows the isochrone of age 1 Myr. In addition, BHAC15 published the absolute magnitudes in $VRIJHKLM$, and we showed the distribution of PMS stars in the CMDs in the lower panels. The distribution of PMS stars in the $(M_I, V - I)$

¹⁵ The G7Ib star VSA 199 (= M2k3581 = M4k4207) could be a possible member of this age group, but the absolute magnitude of the star ($M_V = -2.6$) is somewhat fainter than that of luminosity class Ib. The star is too faint and therefore too old to be an evolved counterpart of these bright B-type stars.

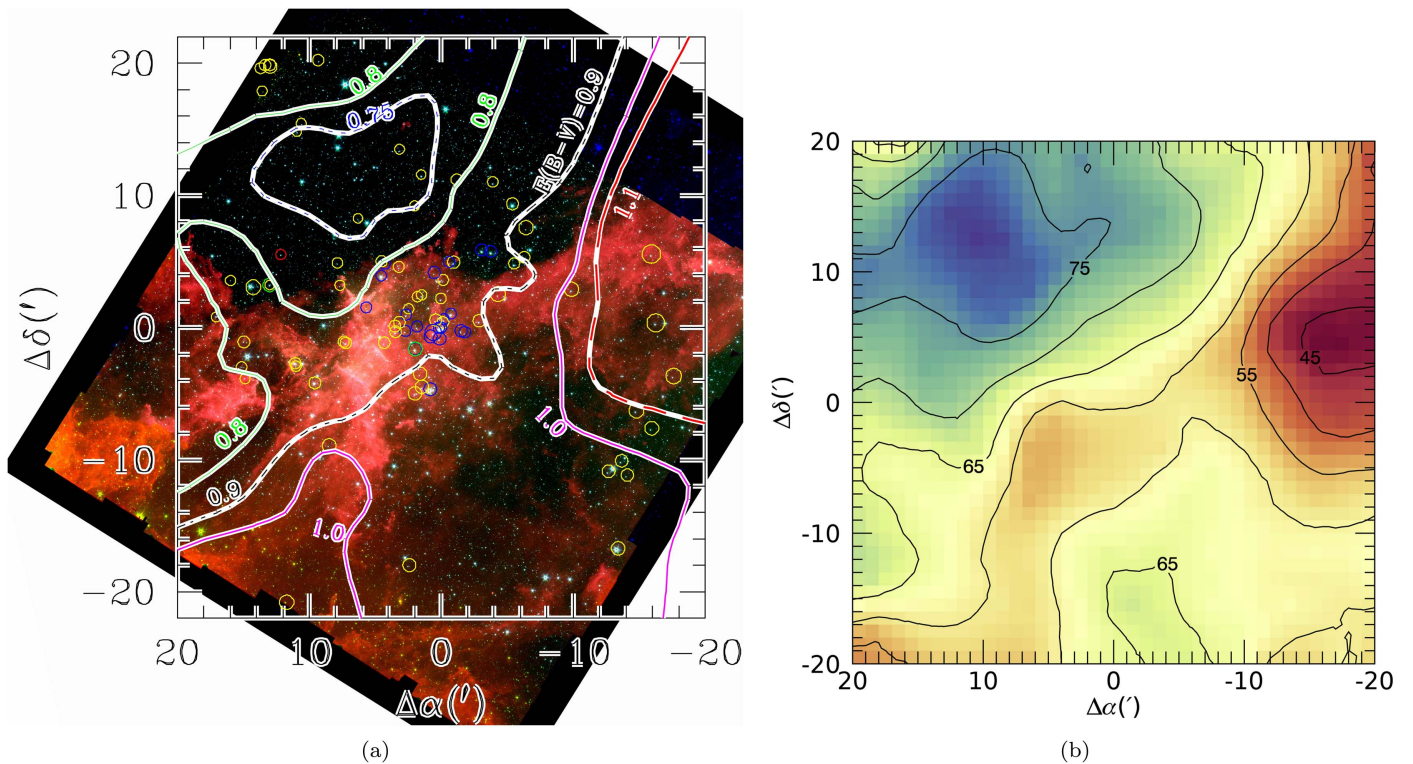


Figure 19. (a) The reddening map of IC 1805 superimposed on the color-composite MIR image (color encoding—red: $8.0 \mu\text{m}$, green: $4.5 \mu\text{m}$, blue: $3.6 \mu\text{m}$). The lines represent the iso-reddening contours smoothed with the scale length of $1/5$. The line type and thickness represent different amounts of reddening $E(B - V)$ as shown in the figure. The circles indicate the early-type stars used in the reddening determination. The size of the circles is proportional to the brightness of the stars. The color of the dots is related to the membership of the star—red: $\text{H}\alpha$ emission star, blue: X-ray emission star, and yellow: normal early-type star. (b) Surface density of field stars ($I = 17\text{--}20.5$ mag and below the PMS locus). The numbers on the contour denote the surface density in units of (star arcmin^{-2}).

diagram follows relatively well the isochrone of age 1 Myr, but that in the $(M_I, R - I)$ diagram does not well match the isochrone. This fact implies that M_R magnitude of **BHAC15** is not well matched to the M_R magnitude of real PMS stars.

We estimated the mass and age of individual PMS stars by interpolating the PMS evolution tracks, and compared the age and mass estimated from each diagram in Figure 25. Figure 26 shows the difference in mass and age from each diagram. Because many PMS evolution models show a mass–age relation (see Sung et al. 1997, 2004 for details), we compared the mass and age of 485 stars with $m = 0.3\text{--}1.0 M_\odot$ from **SDF00**. The masses from the two PMS evolution models are consistent with each other for $\log T_{\text{eff}} \lesssim 3.6$. The difference increases for hotter stars, but this may be due to the mass limit of **BHAC15** ($m \leq 1.4 M_\odot$). As expected from Figure 25, the age of low-mass PMS stars from **BHAC15** is systematically younger than that from Siess et al. (2000) by about 0.87 Myr. Because the **SDF00** isochrones of younger age ($\lesssim 5$ Myr) do not follow the distribution of low-mass PMS stars in the HRD well, the difference increases for low-mass stars. The middle and lower panels of Figure 26 compare the mass and age from the HRD and two CMDs based on the PMS evolution models of **BHAC15**, which show the internal consistency of mass and age from various diagrams. Although there is some scatter, the mass and age from the HRD and the $(M_I, V - I)$ CMD are in general consistent with each other. The small difference in mass implies that the temperature scale of **BHAC15** and that of Sung et al. (2013a) are consistent with each other. We checked the relation between temperature and $(V - I)$ using the same stars as **BHAC15**, and found that the relation is consistent within the observational errors. However, the differences are

very large between the physical parameters from the HRD and the $(M_I, R - I)$ CMD. The difference in mass is rather systematic, but the difference in age is very large and not systematic. Therefore, although reliable masses and ages of PMS stars can be obtained from the HRD or the $(M_I, V - I)$ CMD, it is advisable to not use the $(M_I, R - I)$ CMD.

Figure 27 shows the distribution of age from each diagram. The median age from **SDF00** is 2.48 Myr with 10 and 90 percentiles of 1.11 Myr and 5.75 Myr, respectively. The median age is about 1 Myr younger than the age of the most massive stars in IC 1805. The age spread from the age distribution of PMS stars is about 4.6 Myr according to the definition by Sung & Bessell (2010). This value is consistent with the age spread of NGC 2264 obtained by Sung & Bessell (2010), and Lim et al. (2016). The median age from the HRD and the PMS evolution model by **BHAC15** is 1.61 Myr with an age spread of about 3.9 Myr. The median age and age spread from the $(M_I, V - I)$ CMD is very similar to those from the HRD. However, those from the $(M_I, R - I)$ CMD are far different from the others—the median age and age spread are about 3.0 Myr and 7.5 Myr, respectively.

Sung et al. (2013b) obtained an age spread of about 3 Myr for massive stars and 6 Myr spread for low-mass PMS stars in the massive young open cluster NGC 6231. However, we could find no noticeable age spread among the massive stars in IC 1805 ($\lesssim 1.5$ Myr).

5.2. The Initial Mass Function

The mass of an individual star can be estimated from the HRD. It is implicitly assumed that all stars are single stars even

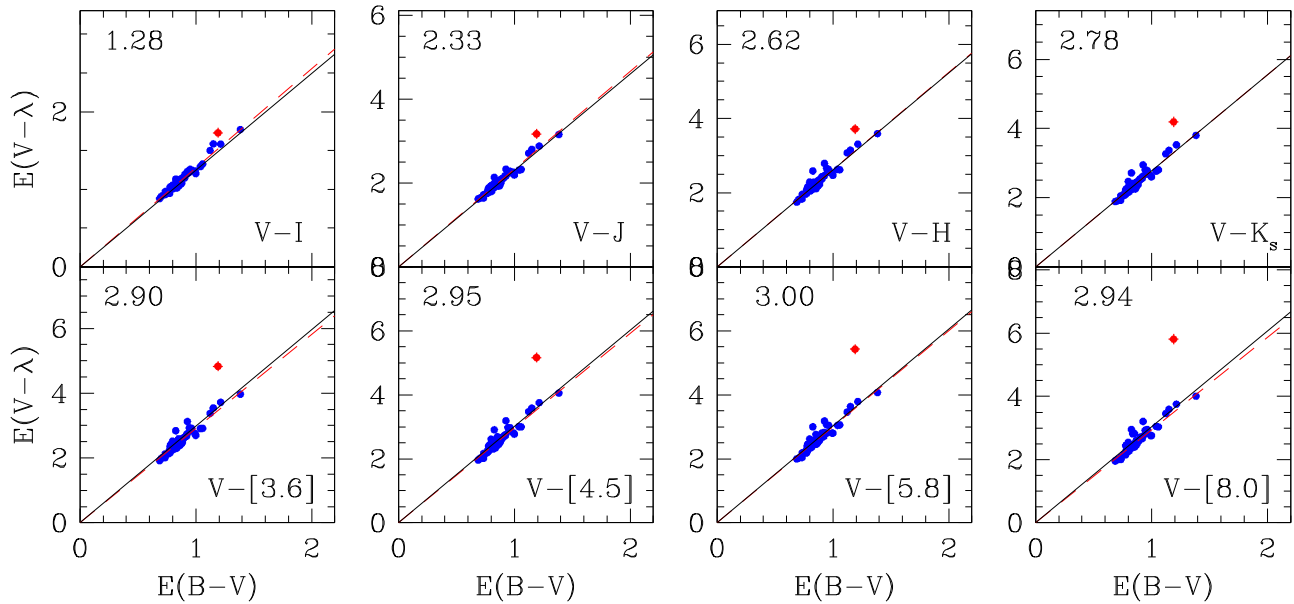


Figure 20. Reddening law of IC 1805. The solid line is the $E(V - \lambda)/E(B - V)$ ratio for $R_V = 3.05$, while the red dashed line represents the mean color-excess ratio from normal early-type stars in the CFH12K FOV. The number in each panel denotes the mean value of the color-excess ratio for the given color. The $H\alpha$ emission star VSA 113 (O9.5Ve or Be—red diamond) shows an abnormal value due to the excess emission from a circumstellar disk.

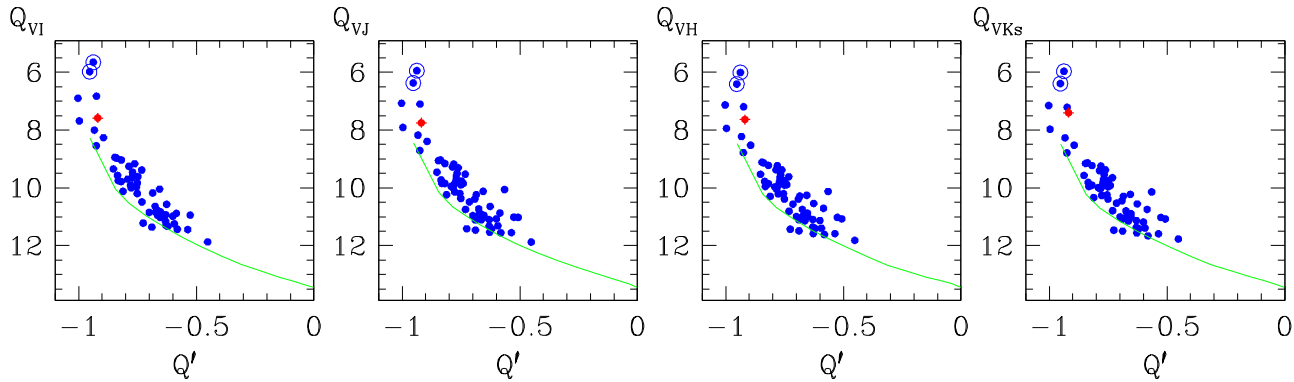


Figure 21. Reddening-independent index $Q_{V\lambda}$ vs. a modified Johnson $Q(Q')$ diagram of IC 1805. Dots represent early-type stars used in Figure 20. Dots with an open circle denote two evolved stars, HDS 15558 and HD 15570. The thick solid lines in each panel represent the ZAMS line at a distance modulus of 11.9 mag.

though the multiplicity of a few massive stars are known (Rauw & De Becker 2004; De Becker et al. 2006; Hillwig et al. 2006; Rauw & Nazé 2016). The effect of binarity on the shape of the IMF has been discussed in Sung & Bessell (2010). The mass estimate of massive stars from the HRD is not easy because a small difference in age gives a very different position in the HRD, and it is therefore impossible to use a single isochrone or mass–luminosity relation. In addition, the complex evolutionary tracks of massive stars make this matter even more difficult. We used the same method of estimating the mass of massive stars ($m \geq 20M_{\odot}$) as described in Sung et al. (2013b) based on the stellar evolution tracks of Ekström et al. (2012). The mass of intermediate-mass MS stars was estimated using the mass–luminosity relation of the isochrone of age 3.5 Myr. The mass and age of PMS stars were estimated by interpolating the PMS evolution tracks. For consistency with the mass scale of our previous works, and due to the lack of PMS evolution tracks for $m > 1.4M_{\odot}$ in BHAC15, we estimated the mass of PMS stars using the PMS evolution models of SDF00. Then the number of stars in a logarithmic mass interval of $\Delta \log m = 0.2$ was calculated.

However, we should consider two factors when we derive the IMF of IC 1805. The first is to select the region where the membership selection is homogeneous. Although X-ray observation gives the highest membership selection probability (Sung et al. 2004), *Chandra* or *XMM-Newton* observations are restricted to the cluster center. In addition, $H\alpha$ photometry is shallow in the extreme southern and northern regions. Despite its lower selection probability, the selection of MIR YSOs is homogeneous at least in the SST/CM FOV. Although we observed a much larger area, the IMF will be determined only for the SST/CM FOV. The next issue is to subtract the contribution of Cas OB6 association and field interlopers. To estimate the number of field interlopers in the PMS locus of IC 1805, we checked the CMD of the nearby old open cluster Tompaugh 4 (Subramaniam et al. 2010). The cluster region is slightly more reddened ($E(B - V) \approx 1.1$), and predicts more high-mass PMS stars ($m \approx 3 \sim 5M_{\odot}$) than the number of stars in the PMS locus. In addition, the depth of their photometry was too shallow to estimate the contribution of faint red foreground stars. Finally, we decided to search for a control field within the observed region. We checked the surface

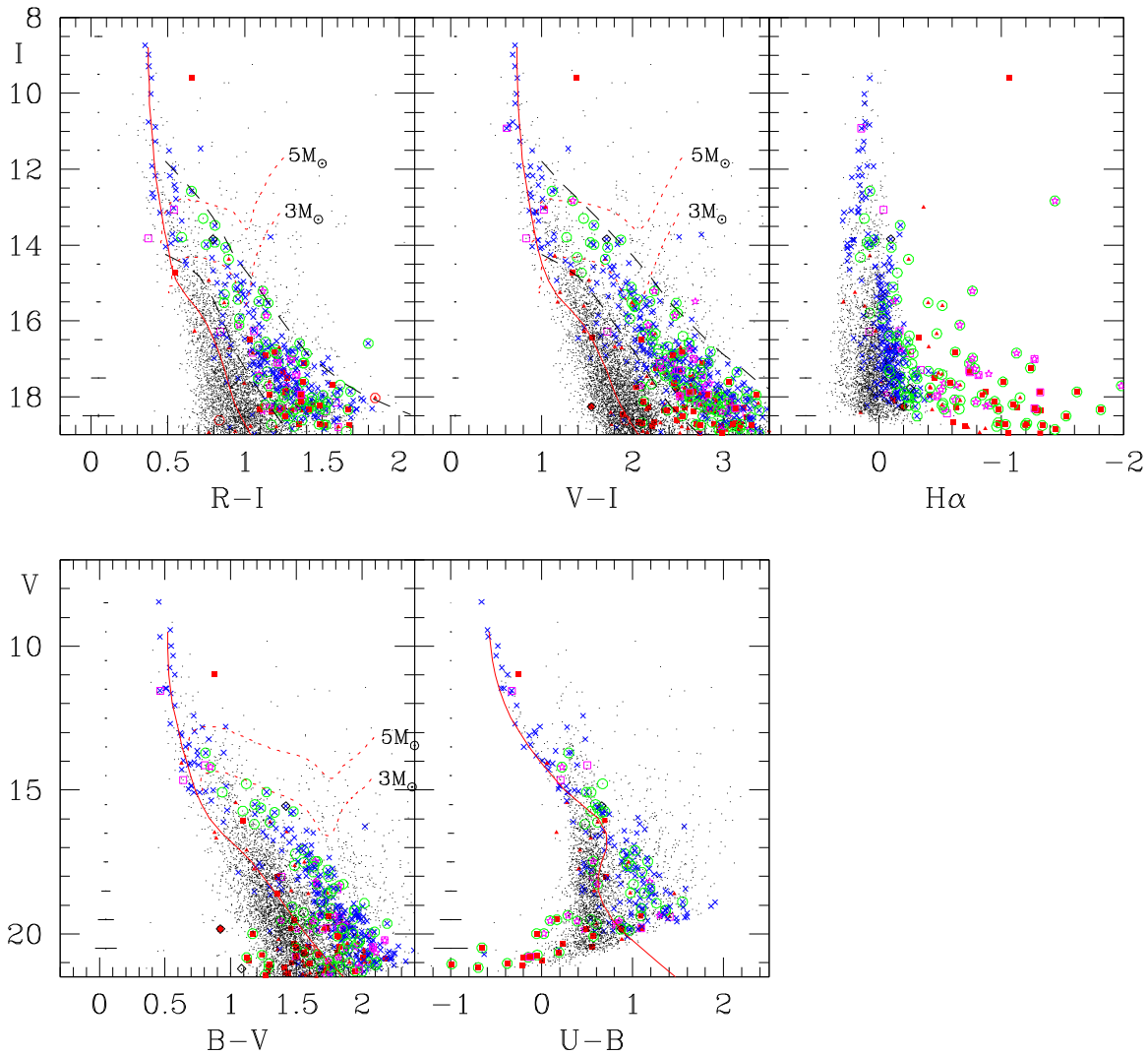


Figure 22. Color–magnitude diagram of IC 1805 based on the data obtained with the AZT-22 1.5 m telescope at Maidanak Astronomical Observatory. The solid line in each panel represents the reddened ZAMS with $E(B - V) = 0.85$ and $V_0 - M_V = 11.9$ mag, while the two dashed lines denote the upper and lower boundaries of the PMS locus of IC 1805. Mean photometric errors are shown in the left of each panel. The other symbols are the same as in Figure 9. The two dotted lines in the CMDs are the PMS evolutionary tracks of $3 M_\odot$ and $5 M_\odot$ stars, respectively, from Siess et al. (2000).

density variation of massive stars, Class III, IV stars, and MIR YOSs, and found that it reached a saturation level between¹⁶ $r \simeq 12' - 15'$. After various trials, the southern region of *SST/CM* FOV ($\Delta\delta \leq 12'$) was selected as the control field (the hatched area in Figure 14). The presumed Cas OB6 association member BD+61 493 is in the selected field region, and presumably the contribution of the Cas OB6 association can be subtracted. Although the density of H α emission stars or MIR excess stars is very low, some number of cluster members could still occur within the control field. In that case, over-subtraction of the field contribution is inevitable.

The first step is to check the mass spectrum of each component—members (early-type members, H α emission stars, and MIR YSOs), Class III stars, Class IV stars, stars with X-ray emission or no membership criterion, and all stars in the PMS locus. The mass spectrum of each component in the cluster region and field region is shown in the upper panels of Figure 28. In the figure, we can easily see that each component has a different contribution to the total mass spectrum (dotted

line)—cluster members dominate in the massive part, while Class IV objects and stars with no membership criterion or X-ray emission occupy the greater part at intermediate-mass and at the low-mass regime, respectively. The surface density of member stars is very low, but non-negligible in the field region. BD +61 493 is the only star with $m \geq 10M_\odot$ in the field region. In the middle panels of Figure 28, we compared the surface density of three regions for three components. The surface density is, in general, highest in the *Chandra* FOV and lowest in the field region. However, the difference in surface density is a strong function of mass as shown in the lower panels. The surface density of stars in the PMS locus with no membership criterion or X-ray emission is higher than that of the cluster region and even that of *Chandra* FOV in the mass range of $\log m = 0.1 - 0.6$, which is due to higher contribution of background MS stars as can be seen in the right panel of Figure 19 (the surface density of field MS stars is lowest in the center). The shaded region in the lower right panel represents the mass range of over-subtraction.

The IMF of IC 1805 is derived by subtracting the contribution of the Cas OB6 association and field stars (*SST/*

¹⁶ Recently, Panwar et al. (2017) derived about $9'$ for the radius of IC 1805.

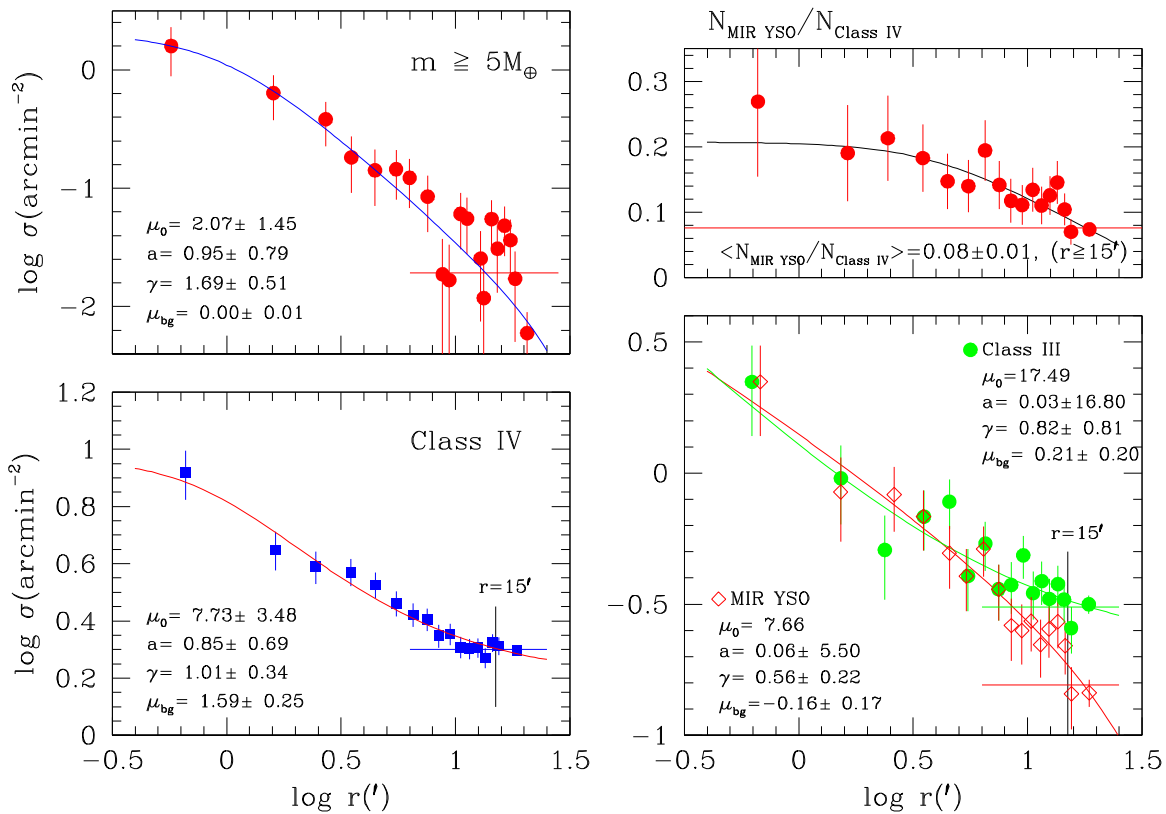


Figure 23. Surface density profile of massive stars ($m \geq 5M_{\odot}$ —upper left panel), Class IV (lower left panel), radial variation of the ratio between MIR YSOs and Class IV objects (upper right) and of MIR excess PMS members and Class III objects (lower right panel). The solid line represents the best fit to the EFF model (Elson et al. 1987), and the fitting parameters are shown in each panel. The horizontal line in each panel represents the average surface density of each object ($r \geq 12'$ for massive stars, and $r \geq 15'$ for the others). The error bars are derived by assuming Poisson statistics.

CM—Field) from the mass spectrum of the cluster region (SST/CM—Cluster). The net number of cluster stars for each component (members, Class III, Class IV, stars in the PMS locus with no membership or X-ray emission) is calculated for the given mass range, and then we calculate the IMF of IC 1805. The calculation is performed for the interval of $\Delta \log m = 0.1$ for $\log m < 1.5$ if the net number of cluster stars is larger than 0. The final IMF of IC 1805 is presented in Figure 29. The IMFs of NGC 1893, NGC 2264, and NGC 6231 are also shown for comparison. The IMF of IC 1805 shows a large fluctuation for massive stars ($\log m \gtrsim 1.0$), a peak at $\log m \approx 0.6$ – 0.7 , and then declines rapidly due to the incompleteness of the photometry. The over-subtraction of the field contribution is evident in the mass range of $\log m = 0.1$ – 0.5 . The slope of the IMF of IC 1805 is $\Gamma = -1.3 \pm 0.2$ for $\log m \geq 0.6$, which is very similar to that of NGC 1893 ($\Gamma = -1.3 \pm 0.1$, Lim et al. 2014b) in the Perseus arm, but slightly steeper than that of NGC 6231 ($\Gamma = -1.1 \pm 0.1$, Sung et al. 2013b), or shallower than the nearby young open cluster NGC 2264 ($\Gamma = -1.7 \pm 0.1$, Sung & Bessell 2010).

Massive stars in young open clusters are concentrated to the center. The origin of such mass segregation is still uncertain. Sung et al. (2013b) prefer a primordial origin (see also Kirk et al. 2016; Lane et al. 2016); however, many theoreticians favor the dynamical origin under the subvirial condition (e.g., McMillan et al. 2007). As mentioned in the Introduction, the surface density of stars in IC 1805 is very low, and so it is sometimes called a “stellar aggregate” or “association.” To address whether mass segregation is prevailing in IC 1805 or

not, we checked the radial variation of the IMF of the massive stars as shown in Figure 30. The slopes of the IMF for $r \lesssim 12'$ (equivalently about 8.4 pc at $d = 2.4$ kpc) are nearly the same ($\Gamma \approx -1.0 \pm 0.1$). No O-type star can be found outside this radius. The only O-type equivalent massive star outside the radius is BD +60 493 (B0.5Ia) which is considered a member of the Cas OB6 association. This fact also implies that the radius of IC 1805 is not much larger than $12'$. Furthermore, mass segregation of massive stars is not evident, at least for $r < 12'$ in IC 1805.

5.3. Total Mass of IC 1805

The total mass of a cluster is an important parameter. Weidner et al. (2010) estimated the total mass of IC 1805 as $10885_{-5528}^{+11137} M_{\odot}$. The mass was originally estimated to be $14400 M_{\odot}$ by Wolff et al. (2007) by assuming that the stars in the mass range of 6– $12 M_{\odot}$ constitute 5.5% of total mass and the number of early B-type stars in IC 1805 is 99. However, the total mass of member stars selected in Section 5 is about $1800 M_{\odot}$.

The mass of IC 1805 can be estimated by the direct integration of the IMF. Before integrating the IMF, we should slightly modify the IMF in Figure 29: we replaced the IMF in the mass range of $\log m = 0.1$ – 0.5 by the dashed line and corrected the IMF for $\log m \leq -0.7$ using the IMF of NGC 2264 by assuming that the difference in the IMF between a given mass and $\log m = -0.7$ is the same amount. This calculation gives $2110 M_{\odot}$, which is definitely a lower limit because we cannot take into account the contribution of

Table 9
Fitting Parameters for the Surface Density Profile

Object	μ_0 (arcmin $^{-2}$)	a ($^{\circ}$)	γ	μ_{bg} (arcmin $^{-2}$)	ρ_0 (arcmin $^{-2}$)	r_c ($^{\circ}$)	ρ_{bg} (arcmin $^{-2}$)
	EFF model			King Model			
massive star	2.069 ± 1.453	0.950 ± 0.787	1.688 ± 0.510	-0.004 ± 0.010	1.686 ± 0.844	1.377 ± 0.434	0.001 ± 0.004
MIR YSO	(7.658 ± 396.7)	(0.059 ± 5.497)	0.561 ± 0.220	-0.158 ± 0.172	0.930 ± 0.189	4.510 ± 0.943	0.101 ± 0.021
Class III	(17.485 ± 7028)	(0.034 ± 16.80)	0.825 ± 0.814	0.212 ± 0.198	0.618 ± 0.236	4.098 ± 1.726	0.282 ± 0.031
Class IV	7.733 ± 3.484	0.847 ± 0.689	1.011 ± 0.340	1.589 ± 0.246	4.014 ± 0.670	3.095 ± 0.508	1.838 ± 0.052
$N_{\text{MIR YSO}}/N_{\text{Class IV}}$	1.342 ± 47.83	4.056 ± 10.98	0.068 ± 2.629	-1.134 ± 47.81	0.172 ± 0.034	13.39 ± 5.235	0.016 ± 0.043

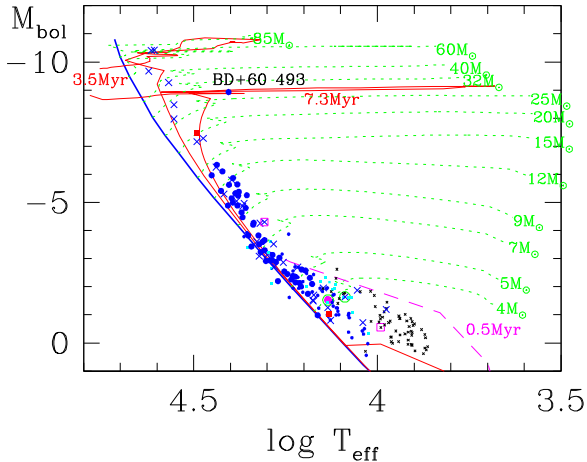


Figure 24. Hertzsprung–Russell diagram of bright stars in IC 1805. Large crosses, red squares, large magenta dots, large blue dots, small blue dots, small cyan squares, and black crosses represent, respectively, X-ray emission stars or candidates, H α emission stars or candidates, H α emission stars with X-ray emission, early-type stars, early-type candidates, stars with uncertain membership, and stars with no membership information. Stars with YSO class I, F, II, t, T, P, and g are superposed with an additional symbol as in Figure 9. The thick solid line is the ZAMS of Ekström et al. (2012), while thin solid lines are the isochrones for ages 3.5 Myr and 7.3 Myr interpolated from the stellar evolutionary tracks of Ekström et al. (2012) and the PMS evolution tracks of SDF00. The thin dashed line in the lower right is the isochrone of age 0.5 Myr interpolated from the PMS evolution tracks of SDF00. The dotted lines with mass to the right are the stellar evolution tracks of Ekström et al. (2012).

multiple systems among member stars. We also calculated the total mass of stars with masses larger than $5 M_{\odot}$ and $7 M_{\odot}$, and obtained $515.3 M_{\odot}$ and $595.3 M_{\odot}$, respectively.

To derive the total mass of IC 1805, we simulated a model cluster with the given IMF mentioned above and binarity. To be a more realistic model cluster, multiplicity should be taken into account. However, it is virtually impossible to do so because we do not have enough information on the frequency distribution of multiples and the mass ratio distribution and can only take the binary fraction distribution and its mass ratio distribution summarized in Duchêne & Kraus (2013). From several simulations, we calculated the ratios between the total cluster mass and the total primary mass (M_{total}/M_p), the mass of the primaries larger than $5 M_{\odot}$ [$M_{\text{total}}/M_p(\geq 5M_{\odot})$], and that larger than $7 M_{\odot}$ [$M_{\text{total}}/M_p(\geq 7M_{\odot})$]. The ratios are 1.344, 4.310, and 5.128, respectively. The mass of IC 1805 (the cluster region selected in Section 5.2) is estimated to be $2690 \pm 190 M_{\odot}$. The upper limit of the cluster mass can also be derived using the total mass of all member stars in the cluster region with masses larger than $5 M_{\odot}$ and $7 M_{\odot}$ and the ratios above, and obtained $3710 \pm 30 M_{\odot}$. Furthermore, the number of O-type stars ($m \geq 15M_{\odot}$) is also estimated to be

6.9 ± 1.0 , which is in agreement with the number of observed O stars (see the Introduction).

This total mass of IC 1805 is far lower than the cluster mass estimated by Wolff et al. (2007) and Weidner et al. (2010). Were the cluster mass of IC 1805 similar to that estimated by Weidner et al. (2010), we would expect to find about 29 O-type primaries ($m \geq 15M_{\odot}$) (+16 O-type secondaries) rather than the actual content of 8 or 9. Their large estimated cluster mass is probably caused by the inclusion of early B-type stars belonging to the Cas OB6 association.

6. Discussion

6.1. Distance of W3 and W4

Most investigators implicitly assumed that the three active SFRs W3, W4, and W5 in the Cas OB6 association are at the same distance (e.g., Megeath et al. 2008). The reason for this assumption is that star formation in W3 is considered to have been triggered by the massive young open cluster IC 1805 because this region of the Galaxy has for a long time been thought of as the site of triggered sequential star formation. However, there is no direct evidence of triggered star formation in W3 by W4. The young open cluster in W3, IC 1795, is nearly the same age as IC 1805 (Oey et al. 2005), and the three young SFRs in W3 (W3 Main, W3(OH), and W3 North) show far different populations (Feigelson & Townsley 2008), indicating that different star-formation mechanisms operated in the different SFRs. The distance of IC 1805, derived from the ZAMS fitting, gives $2.4 (\pm 0.2)$ kpc, which is consistent with the distance obtained by previous optical investigators as mentioned in Section 4.3. For a long time, the distance from ZAMS fitting to clusters provided the most accurate distances and was the most important step in the distance ladder out to the distance of external galaxies in the local group. However, this assumption has been challenged by the emergence of μ arcsecond (μ as) accuracy astrometry from radio VLBI observations (Reid & Honma 2014). Xu et al. (2006) and Hachisuka et al. (2006) measured the parallax of a methanol maser and H $_2$ O maser in W3(OH), respectively, and obtained a consistent distance of 2.0 kpc. More recently, Matsumoto et al. (2011) obtained an even smaller distance of $1.67^{+0.21}_{-0.17}$ kpc based on methanol maser emission from an ultracompact H II region in W3(OH) from a shorter baseline observation. Although the internal error of radio VLBI astrometry is very small (less than 1μ as), there could be several sources of systematic external errors—variability of maser sources (very few maser spots persist for more than a year), spatial motion of maser spots, variation of the centroid position of astrometric references due to variability or jet ejection from AGNs, up to a few μ as error due to the zenith delay correction, and some systematic sensitivity variation due to the angular offset of the astrometric

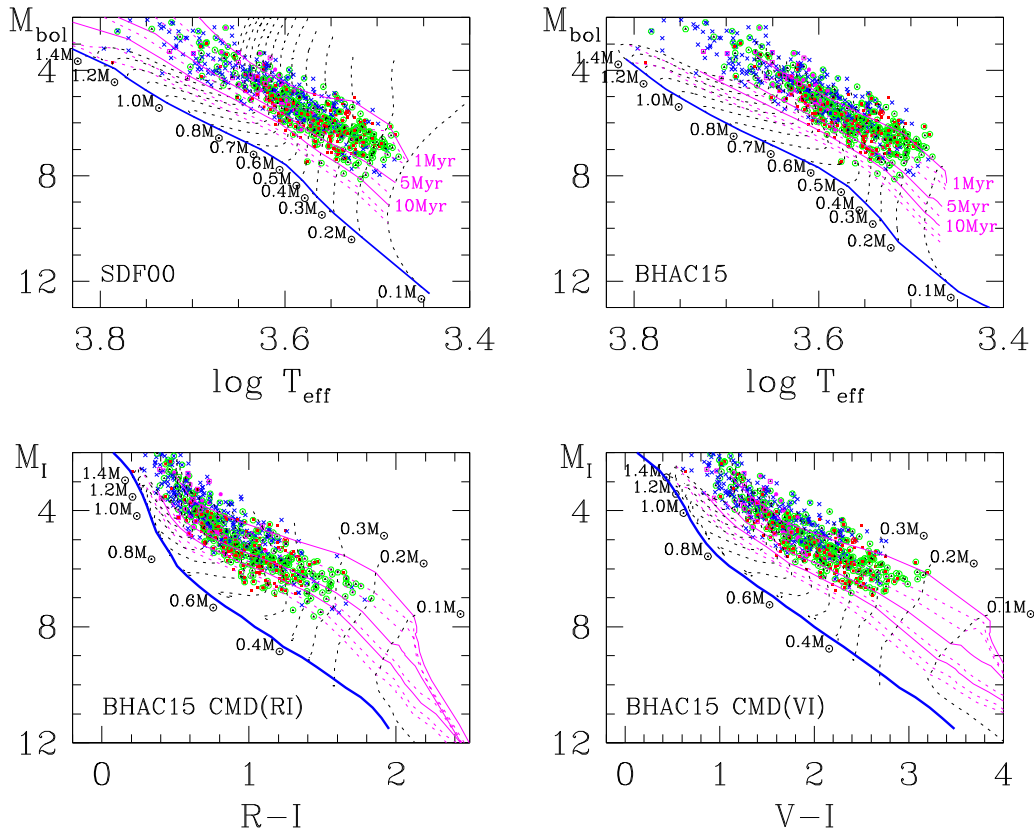


Figure 25. Hertzspung–Russell diagrams (upper panels) and the $(M_I, R - I)$ or $(M_I, V - I)$ color–magnitude diagrams (lower panels) of PMS stars in IC 1805. The thick blue solid line in each diagram is the ZAMS relation. The magenta solid lines represent the isochrones of age 1, 5, and 10 Myr interpolated from the PMS evolution tracks, while the magenta dashed lines are the isochrones of ages 2, 3, 7 (upper) or 8 (lower), 15, and 20 Myr. The dotted lines with mass to the left or right are the PMS evolution tracks for the mass. The other symbols are the same as in Figure 9. The upper left panel is based on the PMS evolution models by SDF00, and the other panels are based on the recent PMS evolution models by BHAC15.

reference. Therefore, unknown external errors could be much larger than the published internal errors. Most recently, the astrometric satellite *Gaia* released the first result from the data collected during the first 14 months. Lindegren et al. (2016) compared the *Gaia* astrometric data with those from radio VLBI astrometry for a representative sample, and showed large differences for some objects (see their Table C.1). To check the reliability of the ZAMS relation, we have selected proper motion and parallactic members of 34 nearby open clusters ($d \lesssim 1$ kpc) using the *Gaia* DR1 TGAS data, and found that their parallactic distance is consistent with the ZAMS-fitting distance within the scatter of parallaxes (about 0.2 mag) among the selected members.

Although the reddening-free indices used in this paper are relatively immune to variations in abundance, it is better to check the effect of abundance differences on the ZAMS relation. According to Genovali et al. (2014) the abundance gradient from δ Cepheid variables, which represent the young population in the Galactic disk, is $[\text{Fe}/\text{H}] = 0.49 (\pm 0.03) - 0.051 (\pm 0.003) R_{\text{GC}}$ (kpc). The abundance at IC 1805 ($R_{\text{GC}} \approx 10.3$ kpc) is estimated to be about -0.035 dex. Furthermore, the gradient between $R_{\text{GC}} \approx 7$ – 10 kpc is much shallower than the average slope (see the lower panel of Figure 4 of Genovali et al. 2014), therefore the abundance near IC 1805 is probably close to the solar value, and thus there should be no difference in abundance, hence no impact on distance determination. However, the abundance of the stars in IC 1805 may be lower than the value estimated above (e.g., $[\text{Fe}/\text{H}] \approx -0.13$ if we adopt the abundance gradient from red giant stars

($d[\text{Fe}/\text{H}]/dR_{\text{GC}} = -0.07$ for $\tau < 1$ Gyr, Anders et al. 2016)), the bolometric magnitude difference of the ZAMS relation of massive stars between $[\text{Fe}/\text{H}] = 0.00$ and -0.13 is estimated to be about $0.14 (\pm 0.02)$ mag at a given temperature from the stellar evolution models of Georgy et al. (2013). The abundance difference from the solar metallicity, if true, may slightly reduce the difference between the distance of IC 1805 from the ZAMS fitting and that of W3(OH) from radio astrometry.

Recently, Bakis et al. (2016) determined a distance of 1.7 ± 0.2 kpc to the early-type eclipsing binary DN Cas in the Cas OB6 association and classified DN Cas as a B0V+B1V system. However, Hiltner (1956) classified the star as a O8Vvar, which would make a difference to the deduced distance. The spectra in Figure 2 of Bakis et al. (2016), as well as our unpublished high-resolution echelle spectra obtained with the Bohyun-san Observatory Echelle Spectrograph (BOES—Kim et al. 2002), show many helium lines, such as He II $\lambda\lambda$ 4200, 4541, 4686, He I $\lambda\lambda$ 4026, 4144, 4387, 4471, and C III $\lambda\lambda$ 4647/4650/4651. The strength of He II λ 4541 is slightly stronger than He I λ 4388, and He II λ 4200 is stronger than He I λ 4144. The strength of C III $\lambda\lambda$ 4647/4650/4651 of the secondary (see Figure 2 of Bakis et al. (2016) at phase 0.996) is slightly stronger than that of He II λ 4686, while that of the primary with longer wavelength is opposite. These features indicate that DN Cas is a binary system but with a O8V primary and O9.5V secondary. The absolute magnitude difference between O8V and B0V is about 0.85 mag (Sung et al. 2013a), and therefore the distance to DN Cas may be

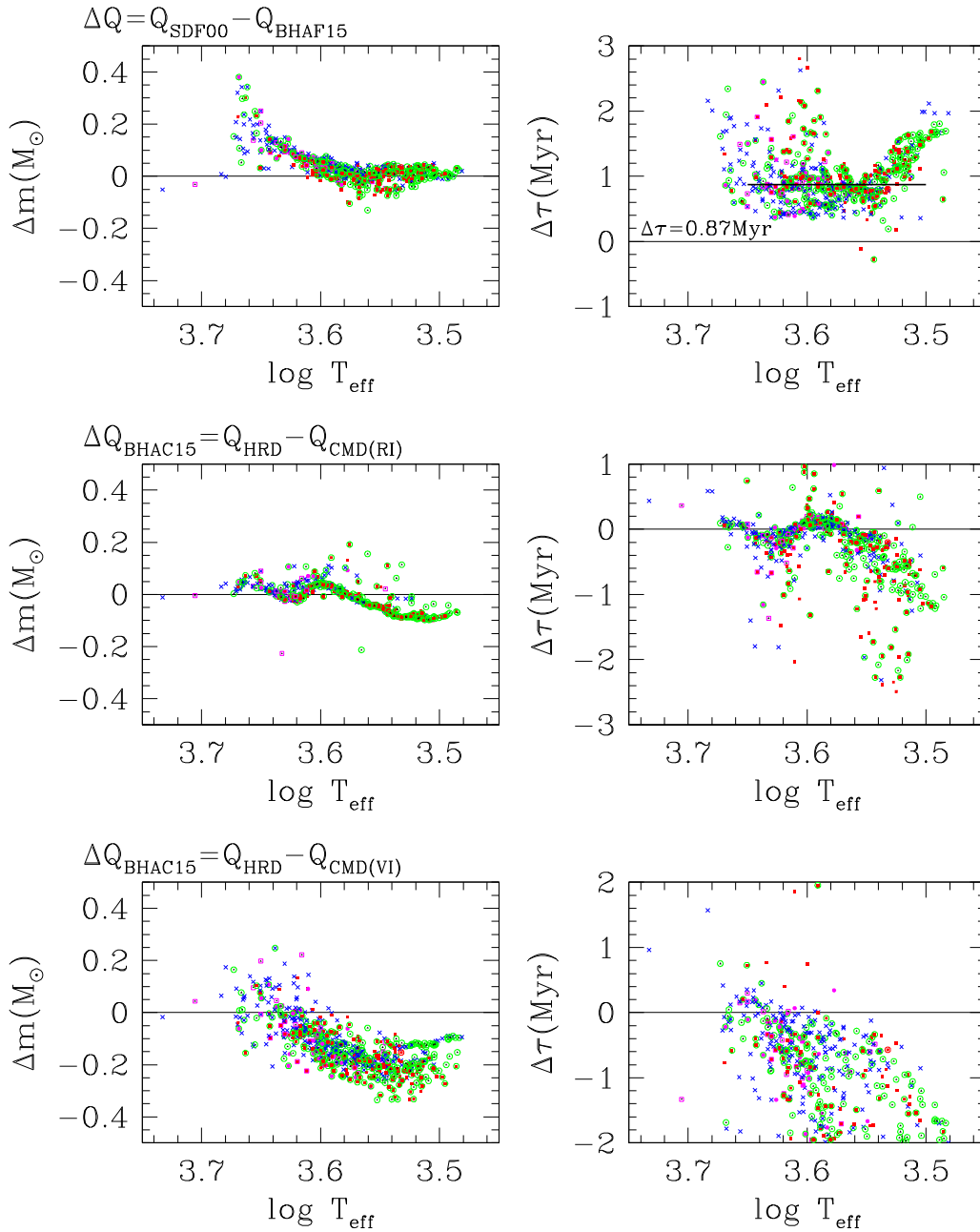


Figure 26. Comparison of mass and age from each diagram in Figure 25. The meaning of Δ is explained in the top of the left panels. The upper panels compare the mass (left) or age (right) from the HRDs in the upper panels of Figure 25. The middle and lower panels show the difference of mass or age from the HRD (upper right panel of Figure 25) and that from the CMDs (lower panels of Figure 25) of BHAC15.

about 2.5 kpc ($V_0 - M_V \approx 12.0$). Hence the smaller distance obtained by Bakis et al. (2016) is probably caused by the misclassification of the spectral type.

Now we should reconsider whether the active SFRs W3–W4–W5 are at the same distance or not. Normally, the width of a spiral arm is considered to be about 500 pc. Currently, the number of SFRs measured with accurate radio VLBI astrometry is over 100 (Reid & Honma 2014). The distances to many SFRs in the Perseus arm were recently published by Choi et al. (2014). Using the data in their Table 5, we calculated the width of the Perseus spiral arm - $\Delta d = 0.9$ kpc at $l \approx 95^\circ$, $\Delta d \gtrsim 1.2$ kpc at $l \approx 108^\circ$, and $\Delta d = 0.7$ kpc at $l \approx 111^\circ$. Because we did not take into account the orientation of the Perseus spiral arm to the line of sight, the difference Δd

above is larger than the actual width of the Perseus arm; however, the actual width may be similar to or larger than 0.5 kpc. The radio VLBI astrometry of three SFRs in the superbubble around the young open cluster NGC 281 ($l \approx 123^\circ$) shows a large difference in distance—IRAS 00420+5530: 2.2 ± 0.05 kpc and NGC 281 W: $2.8^{+0.26}_{-0.22}$ kpc (Sakai et al. 2013). The size of the W4 superbubble is much larger than that of NGC 281, and so we can expect a much larger size for the W4 region. Reynolds et al. (2001) could not find any sign of $H\alpha$ line splitting, and concluded that the large $H\alpha$ emission structure has a loop shape, rather than a shell structure. They considered that the loop could be of cylindrical shape and its radial extent similar to its extent on the sky. In addition, the size of H I holes (H I superbubbles) from the H I

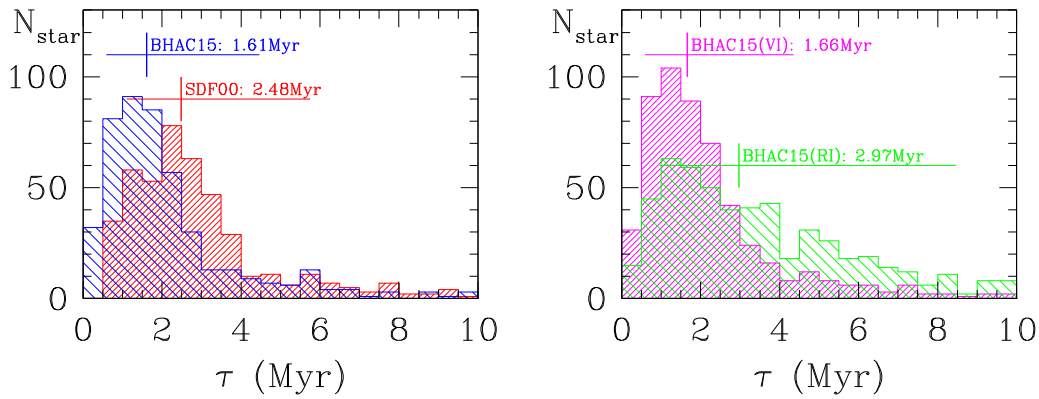


Figure 27. Age distribution from PMS models. The vertical bar represents the median age of stars with masses between 0.3 and $1.0 M_{\odot}$, and the horizontal bar shows the range of 10% and 90% of the distribution.

nearby galaxy survey (Bagetakos et al. 2011) range from about 100 pc (limited by the resolution of radio observation) to about 2 kpc. From the information gathered above, we can state that there are no reasonable physical grounds for assuming that the giant H II regions W3 and W4 are at the same distance.

We searched for stars within 30 arcmin of IC 1805 in the TGAS catalog (Lindgren et al. 2016), and retrieved data for 103 stars. Among them, 33 stars are O- or early B-type stars, and one of them (ALS 7225 = KM Cas, O9.5V((f))) is close to the western edge of W4. The latter star is not considered to be a member of IC 1805, and is excluded in the statistics. Figure 31 shows the distribution of the TGAS parallaxes. The parallaxes for eight bright O-type stars were more concentrated around $\pi = 0.56$ (mean value) (± 0.16) mas, while those for 24 B-type stars scattered more widely with a median value of 0.32 (± 0.33) mas. The median value for all 32 early-type stars is 0.40 (± 0.32) mas (equivalently $d = 2.5$ (1.4–13) kpc), which is very similar to the distance obtained from the ZAMS fitting in Section 4.3. However, the error of the parallax measurements, even for the TGAS catalog, is still very high (about 0.27 mas for 8 O-type stars), so we will have to wait for a few more years to get a better distance to IC 1805 from *Gaia* stellar parallaxes.

As mentioned in Section 4.1, the clouds associated with W3 are in front of IC 1805. Assuming that the radial distribution of faint MS field stars below the PMS locus is homogeneous, the surface density difference in Figure 19 between IC 1805 and the PAH emission nebula in the west of the observed FOV (probably at the same distance as W3) that is about 15%, can be converted into 0.36 kpc. This value is very similar to the difference in distance between W3(OH) and IC 1805. From the morphology and distance of the region, we can sketch a picture of the region. The young open cluster IC 1805, or more exactly, most of the massive stars, may be at the far side of the bubble. However, we cannot rule out the possibility of a large radial scatter of member stars inside the bubble that can be speculated from the broad MS band of early B-type stars in the CMDs (see Section 5.1). The active SFR W3 is at the western edge of the bubble, and therefore we can expect a large spread in distance among the stars/SFRs in W3. The reddening-free CMDs of IC 1795 using the data in Oey et al. (2005) indicate that the distance modulus of the cluster is more appropriate for 11.9 mag rather than 11.5 mag ($d = 2$ kpc).

6.2. Do the O and B Stars in IC 1805 Have Different Origins?

As mentioned in Section 5.1, there are many early B-type stars that are apparently brighter than normal stars, and Guetter & Vrba (1989) considered them to be an older group with an age of about a few 10 Myr. We looked for differences in the spatial or kinematic properties among the B-type stars, but could find no difference in the spatial distribution between the brighter and fainter groups. In addition, we homogenized all available proper motion data (Tycho—Hoeg et al. (2000), PPM—Röser & Bastian (1988), USNOB—Monet et al. (2003), USNO ACT—Urban et al. (1997), and Vasilevskis et al. (1965); all data were linearly transformed to the Tycho system, and then merged with an appropriate weight), but we could not find any discrete group among them.

This issue could be disentangled when high quality proper motion and parallax data from *Gaia* become available. However, the quality of the currently available TGAS catalog is not high enough, and we can find no subgroupings among the B-type stars. Figure 32 shows the TGAS proper motions of O- and early B-type stars in IC 1805. Bright B-type stars are colored in green, while normal (fainter) B-type stars are in blue. Normal B-type stars show a slightly larger scatter, but the extreme points are due to a larger error. Therefore, we can conclude that there is practically no difference in proper motion between the bright and normal B-type stars.

The proper motions of the B-type stars show a large scatter as well as an elongated distribution in the proper motion plane. The principal axis of the distribution is rotated by approximately 13° about an east–west direction, which is nearly parallel to the Galactic plane as shown in Figure 32 (right) and the PAH emitting nebula just behind IC 1805. Interestingly, the standard deviation along the principal axis is four times larger than that along the minor axis. The proper motion of eight O-type stars, however, is well localized in a small area in the proper motion plane and the distribution of the O-type stars in the proper motion plane is nearly circular with an axial ratio of about 1.1. Although the proper motion of B-type stars has a large error, the difference in the distribution is remarkable.

If this is a real feature, does it reflect the difference in the formation processes between O- and B-type stars? A possible explanation for this feature, if real, may be the differences in the formation environments. The O-type stars may have formed in the dense central part of a molecular cloud, and therefore they show a small dispersion in proper motion. Whereas, the B-type stars may have two different formation scenarios—one

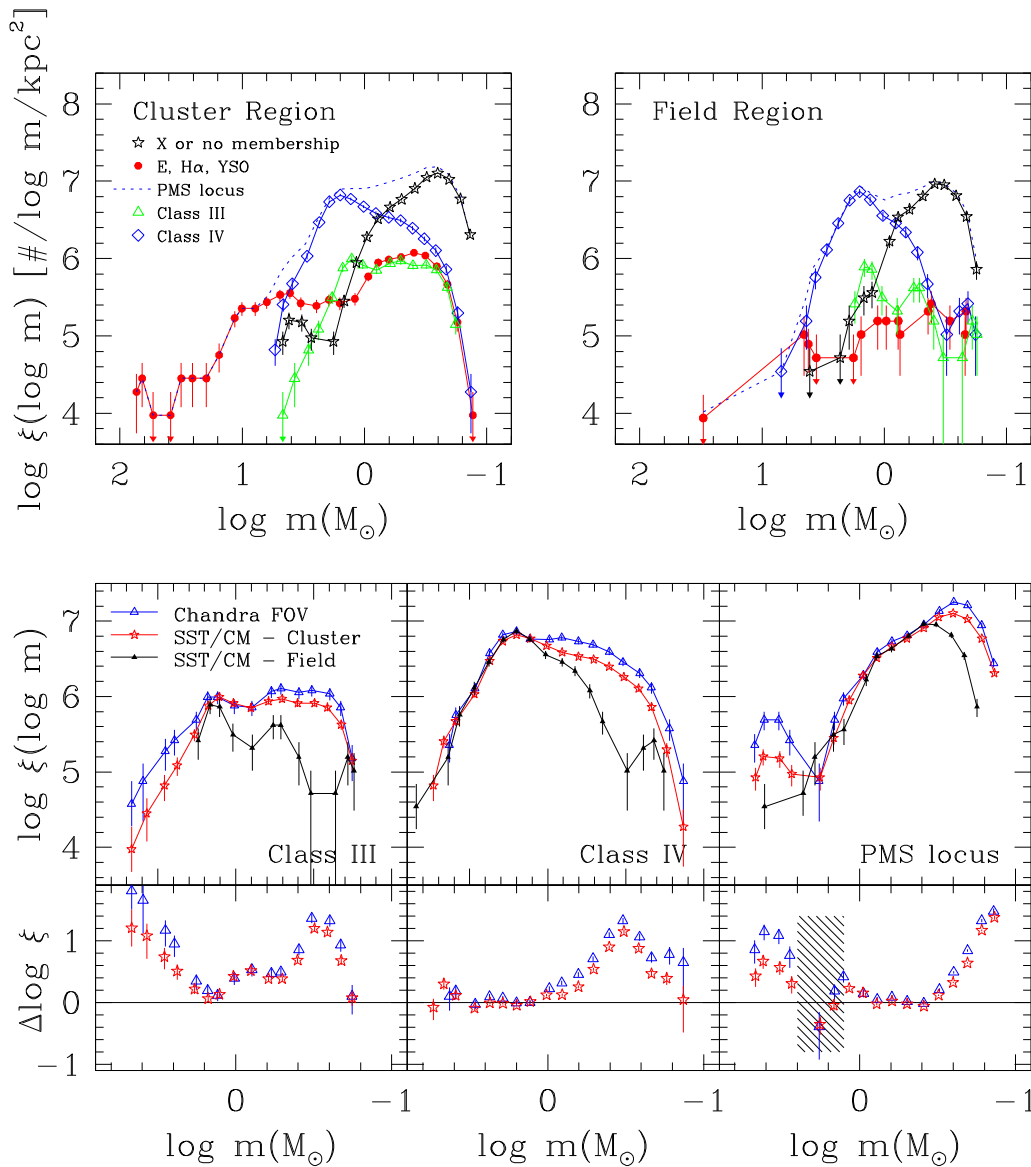


Figure 28. (Upper panel) The mass spectrum of each component of the cluster region (left) and that of the field region (right). Different components show different contributions to the total mass spectrum (dashed line). (Middle panel) Mass spectrum of three regions—*Chandra* FOV, *SST/CM* cluster region, and *SST/CM* field region—for Class III (left), for Class IV (center), and for stars in the PMS locus (X-ray emission stars or stars with no membership criterion; right). (Lower panel) The difference in the mass spectrum relative to that of the field region. The shaded region in the right panel represents the over-subtracted range.

group of B-type stars could have formed from the same molecular cloud as the O-type stars, while the other group of B-type stars could have formed in small clouds dispersed from the center along the Galactic plane. This systematic motion implies that the formation of these B-type stars were affected by an internal trigger. The latter case is similar to the star-formation activity in the small clouds scattered in W4 found by Carpenter et al. (2000), but the expanding direction is along the Galactic plane.

6.3. LS I+61 303 and Star Formation in IC 1805

IC 1805 (or the Cas OB6 association) is considered to be the birth place of the high-mass X-ray binary LS I+61 303 (Mirabel et al. 2004). LS I+61 303 is classified as a Be/X-ray binary system, but the nature of the compact object is still controversial, whether it is a neutron star (pulsar) or a black hole (micro-quasar). The variable radio counterpart of LS I+61

303 has been resolved as a rapidly precessing relativistic jet (Massi et al. 2001). More recently, Dhawan et al. (2006) could not find any relativistic motion, and supports a pulsar wind nebula model. The mass of the system is estimated as $14 \pm 2 M_{\odot}$ for the B0Ve primary star and $2 \pm 1 M_{\odot}$ for the compact object, and the mass loss due to the supernova (SN) explosion is estimated to be less than $2 \pm 1 M_{\odot}$ (Mirabel et al. 2004).

The distance estimate to the object was attempted using radio as well as optical wavelengths. Frail & Hjellming (1991) detected an HI 21 cm absorption feature at $v_r \approx -45 \text{ km s}^{-1}$, and interpreted the velocity component as the spiral arm shock at the nearside edge of the Perseus arm. Because they could not find any velocity component associated with the cold interstellar gas in the Perseus arm, they suggested that LS I + 61 303 is in the Perseus arm just behind the spiral arm shock, but in front of the main Perseus arm. They estimated the distance to LS I + 61 303 as $2.0 \pm 0.2 \text{ kpc}$. Later, Steele et al. (1998) obtained the same distance to the object based on

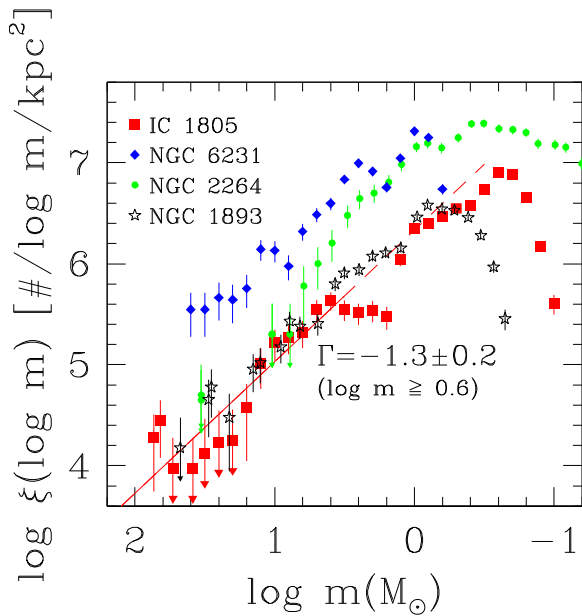


Figure 29. Initial mass function of IC 1805 corrected for the contribution of Cas OB6 association and field stars. The over-subtraction of field contribution is evident for $\log m = 0.1$ – 0.6 as shown in Figure 28. The IMFs of NGC 6231 (diamond), NGC 2264 (dot), and NGC 1893 (star mark) are also shown for comparison.

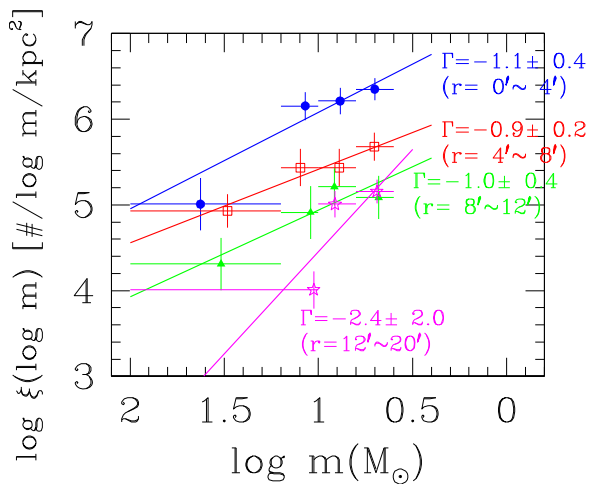


Figure 30. Radial variation of the IMF of massive stars. The slopes of the IMF of the inner three annuli have nearly the same value, but it increases abruptly at $r > 12'$.

spectral classification, reddening estimation, and the $Sp-M_V$ relation. However, as the distance estimated by Frail & Hjellming (1991) is based on the spiral arm model of the Galaxy and that by Steele et al. (1998) is hampered by the peculiar nature of the object, the distance to LS I +61 303 remains uncertain.

To assess the theories on the origin of LS I+61 303, it is necessary to check (1) the star-formation history in IC 1805 and the surrounding Cas OB6 association, and (2) the astrometric properties of LS I+61 303. The probable members of the Cas OB6 association are listed in Garmany & Stencel (1992) and Humphreys (1978). We selected only Cas OB6 members distributed around IC 1805, and placed them in the HRD. The ages of the evolved association members were between 6.0 and 13 Myr, which is consistent with the age of the shell structure

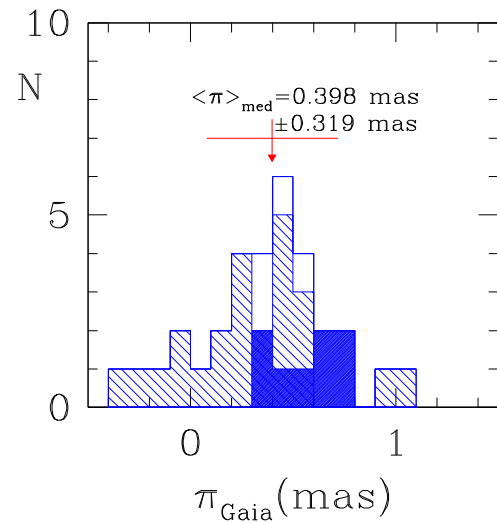


Figure 31. Distribution of the TGAS parallaxes of 32 O- and B-type stars in IC 1805. The dark, shaded, and open histograms represent the parallax distribution of O, B, and all 32 stars, respectively.

of the superbubble (Dennison et al. 1997), while that of the unevolved members is very similar to that of IC 1805 and IC 1795 (Oey et al. 2005). If we focus on the stars in the W3–W4 region, the age of the evolved stars is less than about 10 Myr (their age relies strongly on the membership and spectral type). However, the most reliable age can be obtained from the highly evolved stars in the region (BD +60 493 (B0.5Ia) and OI 109 (O9.7Ia) in IC 1795–Oey et al. 2005), and that is about 7.5 Myr. The age of IC 1805 and IC 1795 is about 3.5 Myr, so the age difference between the two young clusters and these evolved stars is about 4 Myr, which is the lifetime of a very massive star. The most massive stars among the former generation of stars (the members of the Cas OB6 association) may have exploded as SNe about 4 Myr ago and the formation of IC 1805 and IC 1795 in W3 may have been triggered by the SN explosions. The micro-quasar candidate LS I+61 303 could be a remnant of the previous SN explosions.

The above cluster formation scenario may be feasible if we could find other independent information supporting the scenario. The angular distance between LS I+61 303 and the center of IC 1805 is $58'22$ ($\Delta\alpha = 56'24$, $\Delta\delta = -14'23$), and therefore the expected proper motion of LS I+61 303 should be ($\mu_\alpha \approx +0.84$ mas yr $^{-1}$, $\mu_\delta \approx -0.21$ mas yr $^{-1}$). If the SN explosions have been exploded somewhere between IC 1805 and IC 1795, then the expected μ_α should be larger than the value. Mirabel et al. (2004) tried to find the birth place of LS I +61 303 using the proper motion data by Lestrade et al. (1999). Later, Dhawan et al. (2006) provided a more accurate proper motion of LS I + 61 303 [$(\mu_\alpha, \mu_\delta) = (-0.302 \pm 0.07, -0.257 \pm 0.05)$ mas yr $^{-1}$], which is very similar to the proper motion from the TGAS catalog [$(\mu_\alpha, \mu_\delta) = (-0.354 \pm 0.267, -0.077 \pm 0.211)$ mas yr $^{-1}$]. Furthermore, the proper motion vector of LS I+61 303 is very similar to that of IC 1805 traced by the O- and early B-type stars. From the current astrometric data, there seems to be no causal relationship between the star formation in IC 1805 and the formation of LS I+61 303.

7. Summary and Conclusions

In this paper, we presented deep optical and MIR photometry for about 100,000 stars in a $41' \times 44'$ area of the young open

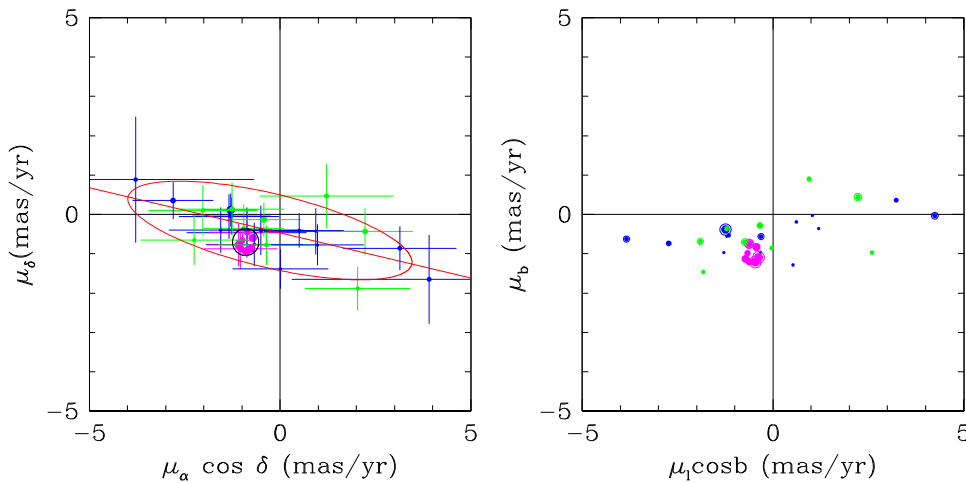


Figure 32. TGAS proper motions of O- and B-type stars in IC 1805 in the equatorial coordinate system (left) and in the Galactic coordinate system (right). Magenta, blue, and green dots represent O-type stars, normal B-type stars, and bright B-type stars in IC 1805, respectively. The ellipses in the left panel show the distribution of the proper motion of B-type stars (red) and that of O-type stars (black), respectively. The red straight line indicates the major axis of the ellipse.

cluster IC 1805 in the Perseus spiral arm. We selected cluster members from optical TCDs and CMDs, $H\alpha$ photometry, X-ray emission, and MIR excess stars from MIR TCDs and SED slope. The low-mass PMS stars selected from $H\alpha$ emission and/or MIR excess emission spread over the whole observed region with no strong concentration.

The total to selective extinction ratio of IC 1805 was determined from the color-excess ratios of optical to MIR colors, and found to be fairly normal ($R_V = 3.05 \pm 0.06$). The distance modulus of IC 1805 was determined from the reddening-free CMDs, and is 11.9 ± 0.2 mag ($d = 2.4 \pm 0.2$ kpc), which is about 0.4 kpc farther than the nearby SFR W3(OH). The massive stars in IC 1805 are well matched to the isochrone of age 3.5 Myr, while the low-mass PMS stars have a median age of 2.4 Myr or 1.6 Myr depending on the adopted PMS evolution models. Although there are many massive stars in IC 1805, the shape of the IMF is still bumpy. The slope of the IMF of IC 1805 is nearly Salpeter value ($\Gamma = -1.3 \pm 0.2$). The shape of the IMF extrapolated down to the brown dwarf regime and a Monte Carlo simulation of a model cluster accounting for the binary frequency and mass ratio distribution of binary system were used to estimate a total mass for IC 1805 of about $2700 \pm 200 M_\odot$, which is far smaller than the mass of IC 1805 proposed by Weidner et al. (2010), but in agreement with the number of massive O stars in the cluster.

Using the recently released astrometric data from the *Gaia* mission, we found the median value of the parallaxes of 32 O- and early B-type members of IC 1805 to be 0.40 (± 0.32) mas [$d = 2.5$ (1.4–13) kpc], which is similar to the parallax from the photometric distance. In addition, the proper motions of early B-type stars show an elongated distribution along the Galactic plane, while those of the O-type stars are well localized. This feature implies that some B-type stars were likely formed from small clouds dispersed by previous episodes of massive star formation (Carpenter et al. 2000) or previous supernova explosions.

The authors thank the anonymous referee who gave many helpful comments and suggestions. H.S. would like to express his thanks to Dr. Inwoo Han, the President of the Korea Astronomy and Space Science Institute for hosting him as a Visiting Researcher. H.S. acknowledges the support of the

National Research Foundation of Korea (Grant No. NRF-2015R1D1A1A01058444).

Facilities: *Spitzer* (IRAC and MIPS), CFHT, Maidanak:1.5 m, *XMM-Newton*, *Gaia*.

Software: IRAF, IDL, SM.

References

- Anders, F., Chiappini, C., Minchev, I., et al. 2016, *A&A*, in press (arXiv:1608.04951)
- Bagetakos, I., Brinks, E., Walter, F., et al. 2011, *AJ*, 141, 23
- Bakis, V., Bakis, H., Bilir, S., & Eker, Z. 2016, *PASA*, 33, 46
- Baraffe, I., Homeier, D., Allard, F., & Chabrier, G. 2015, *A&A*, 577, 42 (BHAC15)
- Bessell, M. S. 1979, *PASP*, 91, 589
- Bessell, M. S. 1990, *PASP*, 102, 1181
- Cardelli, J. A., Clayton, G. C., & Mathis, J. S. 1989, *ApJ*, 345, 245
- Carpenter, J. M., Heyer, M. H., & Snell, R. L. 2000, *ApJS*, 130, 381
- Choi, Y. K., Hachisuka, K., Reid, M. J., et al. 2014, *ApJ*, 790, 99
- Conti, P., & Aschuler, W. R. 1971, *ApJ*, 170, 325
- Damiani, F., Micela, G., & Sciortino, S. 2016, *A&A*, 596, 82
- De Becker, M., Rauw, G., Manfroid, J., & Eenes, P. 2006, *A&A*, 456, 1121
- Dean, J. F., Warren, P. R., & Cousins, A. W. J. 1978, *MNRAS*, 183, 569
- Dennison, B., Topasna, G. A., & Simonetti, J. H. 1997, *ApJL*, 474, L31
- Dhawan, V., Mioduszewski, A., & Rupen, M. 2006, in Proc. VI Microquasar Workshop: Microquasars and Beyond, ed. T. Belloni (Trieste: PoS), 52
- Duchêne, G., & Kraus, A. 2013, *ARA&A*, 51, 269
- Ekström, S., Georgy, C., Eggenberger, P., et al. 2012, *A&A*, 537, 146
- Elmegreen, D. M. 1980, *ApJ*, 240, 846
- Elson, R. A. W., Fall, S. M., & Freeman, K. C. 1987, *ApJ*, 323, 54
- Fazio, G. G., Hora, J. L., Allen, L. E., et al. 2004, *ApJS*, 154, 1
- Feigelson, E., Gaffney, J. A., III, Gamire, G., Hillenbrand, L., & Townsley, L. 2003, *ApJ*, 584, 911
- Feigelson, E., Townsley, L., Broos, P., et al. 2013, *ApJS*, 209, 26
- Feigelson, E. D., & Townsley, L. K. 2008, *ApJ*, 673, 354
- Fitzpatrick, E. L., & Massa, D. 2009, *ApJ*, 699, 1209
- Flaccomio, E., Micela, G., Sciortino, S., et al. 1999, *A&A*, 345, 521
- Forte, J. C. 1978, *AJ*, 83, 1199
- Frail, D. A., & Hjellming, R. M. 1991, *AJ*, 101, 2126
- Fukuda, N., Miao, J., Sugitani, K., et al. 2013, *ApJ*, 773, 132
- Garmany, K., & Stencel, R. E. 1992, *A&AS*, 94, 211
- Genovali, K., Lemasle, B., Bono, G., et al. 2014, *A&A*, 566, 37
- Georgy, C., Ekström, S., Granada, A., et al. 2013, *A&A*, 553, 24
- Guetter, H. H., & Vrba, F. J. 1989, *AJ*, 98, 611
- Gutermuth, R. A., Myers, P. C., Megeath, S. T., et al. 2008, *ApJ*, 674, 336
- Hachisuka, K., Brunthaler, A., Menten, K. M., et al. 2006, *ApJ*, 645, 337
- Hanson, M. M., & Clayton, G. C. 1993, *AJ*, 106, 1947
- Hillwig, T. C., Gies, D. R., Bagnuolo, W. G., Jr., et al. 2006, *ApJ*, 603, 1069
- Hiltner, W. A. 1956, *ApJS*, 2, 389
- Hiltner, W. A., & Johnson, H. L. 1956, *ApJ*, 124, 367

- Hoag, A. A., Johnson, H. L., Iriarte, B., et al. 1961, 17 (Pub. US Naval Obs.), 408
- Hoeg, E., Fabricius, C., Makarov, C. C., et al. 2000, *A&A*, 355, L27
- Humphreys, R. 1978, *ApJS*, 38, 309
- Hur, H., Park, B.-G., Sung, H., et al. 2015, *MNRAS*, 446, 3797
- Hur, H., Sung, H., & Bessell, M. S. 2012, *AJ*, 143, 41
- Im, M., Ko, J., Cho, Y., et al. 2010, *JKAS*, 43, 75
- Ishida, K. 1969, *MNRAS*, 144, 55
- Ishida, K. 1970, *PASJ*, 22, 277
- Johnson, H. L. 1968, in *Nebulae and Interstellar Matter*, ed. B. M. Middlehurst & L. H. Aller (Chicago, IL: Univ. Chicago Press), 167
- Johnson, H. L., & Hiltner, W. A. 1956, *ApJ*, 123, 267
- Johnson, H. L., & Morgan, W. W. 1955, *ApJ*, 122, 142
- Joshi, U. C., & Sagar, R. 1983, *JRASC*, 77, 40
- Kilkenny, D., van Wyk, F., Roberts, G., Marang, F., & Cooper, D. 1998, *MNRAS*, 294, 93
- Kim, K.-M., Jang, B.-H., Han, I., et al. 2002, *JKAS*, 35, 221
- King, I. 1962, *AJ*, 67, 471
- Kirk, H., Johnstone, D., Di Francesco, J., et al. 2016, *ApJ*, 821, 98
- Koenig, X. P., Allen, L. E., Guthermuth, R. A., et al. 2008, *ApJ*, 688, 1142
- Koenig, X. P., Leisawitz, D. T., Benford, D. J., et al. 2012, *ApJ*, 744, 130
- Kook, S. H., Sung, H., & Bessell, M. S. 2010, *JKAS*, 43, 141
- Kwon, S. M., & Lee, S.-W. 1983, *JKAS*, 16, 7
- Lane, J., Kirk, H., Johnstone, D., et al. 2016, *ApJ*, 833, 44
- Lestrade, J.-F., Preston, R. A., Jones, D. L., et al. 1999, *A&A*, 344, 1014
- Lim, B., Sung, H., Bessell, M. S., et al. 2015a, *AJ*, 149, 127
- Lim, B., Sung, H., Bessell, M. S., Karimov, R., & Ibrahimov, M. 2009, *JKAS*, 42, 161
- Lim, B., Sung, H., Hur, H., et al. 2015b, *JKAS*, 48, 343
- Lim, B., Sung, H., Karimov, R., & Ibrahimov, M. 2008, *PKAS*, 23, 1
- Lim, B., Sung, H., Karimov, R., & Ibrahimov, M. 2011, *JKAS*, 44, 39
- Lim, B., Sung, H., Kim, J. S., et al. 2016, *ApJ*, 831, 116
- Lim, B., Sung, H., Kim, J. S., Bessell, M. S., & Karimov, R. 2014a, *MNRAS*, 438, 1451
- Lim, B., Sung, H., Kim, J. S., Bessell, M. S., & Park, B.-G. 2014b, *MNRAS*, 443, 454
- Lindgren, L., Lammers, U., Bastian, U., et al. 2016, *A&A*, 595, 4
- Massey, P., Johnson, K. E., & DeGioia-Eastwood, K. 1995, *ApJ*, 454, 151
- Massi, M., Robó, M., Paredes, J. M., et al. 2001, *A&A*, 376, 217
- Matsumoto, N., Honma, M., Isono, Y., et al. 2011, *PASJ*, 63, 1345
- McMillan, S. L. W., Vesperini, E., & Portegies Zwart, S. F. 2007, *ApJL*, 655, 45
- Medhi, B. J., Maheswar, M., Brijesh, K., et al. 2007, *MNRAS*, 378, 881
- Megeath, S. T., Townsley, L. K., Oey, M. S., & Tieftrunk, A. R. 2008, in *Handbook of Star Forming Regions*, Vol. 1. Northern Sky, ed. B. Reipurth (San Francisco, CA: ASP), 264
- Menzies, J. W., Marang, F., Laing, J. D., Coulson, I. M., & Engelbrecht, C. A. 1991, *MNRAS*, 248, 642
- Mirabel, I. F., Rodrigues, I., & Liu, Q. Z. 2004, *A&A*, 422, L29
- Monet, D. G., et al. 2003, *AJ*, 125, 984
- Ninov, Z., Bretz, D. R., Easton, A. R., Jr., & Shure, M. 1995, *AJ*, 110, 2242
- Normandeau, M., Taylor, A. R., & Dewdney, P. E. 1996, *Natur*, 380, 687
- Normandeau, M., Taylor, A. R., & Dewdney, P. E. 1997, *ApJS*, 108, 279
- Oey, M. S., Watson, A. M., Kern, K., & Walth, G. L. 2005, *AJ*, 129, 393
- Ogura, K., Sugitani, K., & Pickles, A. 2002, *AJ*, 123, 2597
- Pandey, A. K., Upadhyay, K., Nakada, Y., & Ogura, K. 2003, *A&A*, 397, 191
- Panwar, N., Chen, W. P., Pandey, A. K., et al. 2014, *MNRAS*, 443, 1614
- Panwar, N., Samal, M. R., Pandey, A. K., et al. 2017, *MNRAS*, in press (arXiv:1703.03604)
- Rauw, G., & De Becker, M. 2004, *A&A*, 421, 693
- Rauw, G., & Nazé, Y. 2016, *A&A*, in press (arXiv:1608.04499)
- Reid, M. J., & Honma, M. 2014, *ARA&A*, 52, 339
- Reynolds, R. J., Sterling, N. C., & Haffner, L. M. 2001, *ApJL*, 558, L101
- Rieke, G. H., Young, E. T., Engelbracht, C. W., et al. 2004, *ApJS*, 154, 25
- Röser, S., & Bastian, U. 1988, *A&A*, 74, 449
- Sakai, N., Sato, M., Motogi, K., et al. 2013, *PASJ*, 66, 3
- Sana, H., de Mink, S. E., de Koter, A., et al. 2012, *Sci*, 337, 444
- Shi, H. M., & Hu, J. Y. 1999, *A&AS*, 136, 313
- Siess, L., Dufour, E., & Forestini, M. 2000, *A&A*, 358, 5931 (SDF00)
- Skrutskie, M. F., et al. 2006, *AJ*, 131, 1163
- Sota, A., Maiz Apellaniz, J., Walborn, N. R., et al. 2011, *ApJS*, 193, 24
- Steele, I. A., Negueruela, I., Coe, M. J., & Roche, P. 1998, *MNRAS*, 297, L5
- Subramaniam, A., Carraro, G., & Janes, K. A. 2010, *MNRAS*, 404, 1385
- Sung, H., & Bessell, M. S. 2004, *AJ*, 127, 1014
- Sung, H., & Bessell, M. S. 2010, *AJ*, 140, 2070
- Sung, H., & Bessell, M. S. 2014, *ASPC*, 482, 275
- Sung, H., Bessell, M. S., & Chun, M.-Y. 2004, *AJ*, 128, 1684
- Sung, H., Bessell, M. S., Chun, M.-Y., Karimov, R., & Ibrahimov, M. 2008, *AJ*, 135, 441
- Sung, H., Bessell, M. S., & Lee, S.-W. 1997, *AJ*, 114, 2644
- Sung, H., & Lee, S.-W. 1995, *JKAS*, 28, 119
- Sung, H., Lim, B., Bessell, M. S., et al. 2013a, *JKAS*, 46, 103
- Sung, H., Sana, H., & Bessell, M. S. 2008a, *JKAS*, 41, 1
- Sung, H., Sana, H., & Bessell, M. S. 2013b, *AJ*, 145, 37
- Sung, H., Stauffer, J. R., & Bessell, M. S. 2009, *AJ*, 138, 1116
- Townsley, L. K., Broos, P. S., Garmire, G. P., et al. 2014, *ApJS*, 213, 1
- Urban, S., Corbin, T., & Wycoff, G. 1997, *BAAS*, 29, 1306
- Vasilevskis, S., Sanders, W. L., & Van Altena, W. F. 1965, *AJ*, 70, 806
- Weidner, C., Kroupa, P., & Bonnell, I. A. D. 2010, *MNRAS*, 401, 275
- Wolff, S. C., Strom, S. E., & Dror, D. 2007, *AJ*, 133, 1092
- Wolff, S. C., Strom, S. E., & Rebull, L. M. 2011, *ApJ*, 726, 19
- Xu, Y., Reid, M. J., Zheng, X. W., & Menten, K. M. 2006, *Sci*, 311, 54